Department of Advanced Materials Science,
Graduate School of Frontier Sciences,
The University of Tokyo

Master thesis

Structural analysis of lamellar twisting in polymer spherulite by polarized optical microscopy and microbeam x-ray scattering

偏光顕微鏡およびマイクロビーム X 線散乱による
高分子球晶におけるラメラのねじれ構造の解析

Professor　Yoshiyuki Amemiya

076140　Yoshinari Hashimoto

Jan.2009

Acknowledgement

Throughout this work, every member in Amemiya laboratory encouraged me to carry it out.

First of all, I would like to express my deep respect to Prof. Yoshiyuki Amemiya from the bottom of my heart. He continuously encouraged me with helpful and profound advices. He also spared me a time for discussion form his busy scheduling.

I really thank Assistant Prof. Yuya shinohara for supporting my work. I was always surprised at his strikingly deep insights and logical way of speaking. He taught me skills of presentation and writings. Without his cooperation, I could not have accomplished the experiments at KEK and SPring-8 under restricted machine time.

I thank Dr. Yoshinobu Nozue for kind cooperation. He suggested me experimental plans and proper direction of my research. I could maintain high motivation throughout this work thanks to his advices.

I am deeply grateful to Mr. Tatsuya Kikuzuki for helping the simulation work. I could deepen the understanding of x-ray scattering through a long discussion with him.

I thank Prof. Toshio Takahashi for a helpful discussion about the data treatment. His advice was very essential, and kindly guided me to better analysis.

I appreciate Prof. Akihiko Toda and Dr Hiroshi Kajioka at Hiroshima University for sparing me a long time and encouraging me with a hot discussion.

I am thankful to members of Oya laboratory for lending me a microtome, and kindly teaching me the cutting work. I am grateful to members of Ito laboratory for allowing me to use their equipments.

Finally, I would like to express my appreciation to my family and friends. I could manage to complete the thesis thanks to their warm words of encouragement.

Contents

1 Introduction **6**

2 Lamellar twisting **8**
2.1 Hierarchical structure of Polymer crystal 8
2.1.1 First order structure of polymer crystal 8
2.1.2 Higher order structure of Polymer crystal 9
2.1.3 Hierarchical structure of polymer crystal and x-ray scattering . . . 11
2.2 Development of lamellar structure 12
2.2.1 Driving force of crystallization 12
2.2.2 Dependence of growth speed and lamellar thickness on supercooling 14
2.2.3 Regime transition in polymer crystallization 16
2.2.4 Lamellar branching 17
2.3 Twisting lamellae 18
2.3.1 Observation of twisting lamellae and the chain tilt 19
2.3.2 Lamellar twisting of achiral polymer 21
2.3.3 Lamellar twisting of chiral polymer 25
2.3.4 S-shaped lamellae and lamellar twisting 25
2.4 Samples of our research 26
2.4.1 PCL/PVB 26
2.4.2 PVDF/PEA 27

3 Purpose of research **28**
3.1 Summary of previous works 28
3.1.1 S-shaped lamellae 28
3.1.2 Stepwise lamellar twisting 29
3.2 Purpose of this work 29
3.2.1 Elucidation of the lamellar twisting mechanism 29
3.2.2 Elucidation of the mechanism of stepwise lamellar twisting 31

4 Fundamentals of x-ray scattering and polarized optical microscopy **32**
4.1 X-ray scattering 32
4.1.1 Kinematical diffraction theory 32

4.1.2 Fourier transform and Patterson function . . . 34
4.1.3 Form factor and structure factor . . . 35
4.1.4 Informations from SAXS . . . 36
4.1.5 Wide angle scattering from crystalline material . . . 39
4.1.6 Lorentz correction . . . 40
4.2 Polarized optical microscopy . . . 41
4.2.1 Ellipsoidal optical indicatrix . . . 42
4.2.2 Polarized optical microscopy . . . 43

5 Synchrotron radiation and related instrumentation 44
5.1 The principle of the generation of synchrotron radiation . . . 45
5.2 Insertion light source . . . 47
5.3 Characteristics of beamlines . . . 48
5.4 Microbeam x-ray scattering . . . 50
5.4.1 Application of microbeam x-ray scattering . . . 50
5.4.2 Optics for microbeam x-ray scattering . . . 51
5.5 X-ray detecting system . . . 52
5.5.1 Characteristics of x-ray detector . . . 52
5.5.2 Types of x-ray detectors . . . 53
5.5.3 Image intensifier + charge coupled device detector . . . 54

6 Experiment 56
6.1 Sample preparation . . . 56
6.2 Microbeam WAXS measurement . . . 56
6.3 Microbeam SAXS-WAXS simultaneous measurement . . . 59
6.4 Polarized optical microscopy observation . . . 60

7 Data analysis and simulation 61
7.1 Analysis of lamellar twist by microbeam x-ray scattering . . . 61
7.1.1 Plot of azimuthal intensity distribution against radial distance in spherulite (Image-plot) . . . 61
7.1.2 Summary of previous simulation . . . 62
7.1.3 The issues to be overcome in previous works . . . 64
7.1.4 Proposal of modified simulation . . . 65
7.1.5 Sample rotation . . . 66
7.1.6 Determination of stepwise twisting by analyzing other facets . . . 67
7.1.7 Microbeam SAXS . . . 69
7.2 Analysis of lamellar twist with POM . . . 70

8 Result and Discussion 72
8.1 Polarized optical microscopy . . . 72
8.1.1 Growth rate of PCL/PVB spherulite . . . 72
8.1.2 Analysis of stepwise twisting . . . 73
8.2 Microbeam SAXS and SAXS-WAXS simultaneous measurement . . . 75

8.2.1 Comparison of 2D sherulite and 3D spherulite 76
8.2.2 Azimuthal distribution of lamellar diffraction 76
8.2.3 Chain tilt in PCL/PVB spherulite 77
8.2.4 Chain tilt in PVDF/PEA spherulite 78
8.3 Microbeam WAXS 80
8.3.1 Determination of stepwise lamellar twisting from 110 reflection . 80
8.3.2 Determination of stepwise twisting by analyzing other facets . . . 84
8.3.3 Comparison of 2D spherulite and 3D spherulite 85
8.3.4 The ordering of chain packing 87
8.3.5 Azimuthal intensity distribution of hk0 reflection 88
8.3.6 Evaluation of the angular spread of reciprocal spots around the three axes 89
8.3.7 Lamellar orientation in unbanded area 91
8.3.8 Specific structure around spherulite center 92
8.4 Discussion 93
8.4.1 Determination of stepwise lamellar twisting 93
8.4.2 Rhythmic growth 94
8.4.3 The origin of stepwise lamellar twisting 96
8.4.4 The influence of PVB on PCL lamellar structure 97
8.4.5 Driving force of lamellar twist in PCL/PVB spherulite 99
8.4.6 Chiral factor in pure PCL spherulite 99

9 Conclusions and Future works **102**
9.1 Conclusions 102
9.2 Future works 102

Chapter 1

Introduction

Polymer material such as polyethylene is indispensable for daily life today, owing to its invaluable nature of lightweight, plasticity, and mechanical strength. There are several desired macroscopic property of plastic material in individual cases, such as mechanical strength, transparency, and electrical conductivity, which are backed up by microscopic structure of polymer crystal. In general, hierarchical structure exist in polymer crystal from melt, that is to say, crystal packing structure of sub-nano order, crystal and amorphous alternating layer structure (lamella) of 10 nm order, and spherulite of μm order composed of radiating lamellae.

Besides the practical aspect, spherulite has been of academic interest and there remain challenging problems unsolved. Some of spherulites exhibit banding structure under polarized optical microscope (POM). The banding structure indicates the cooperative rotation of radiating lamellae [20]. For example, in the case of Poly-(ε caprolaction)/Poly-(vinyl butyral) (PCL/PVB) blend system, pure PCL does not show clear banding. By contrast, blending PVB gives rise to extremely coherent banding structure as shown in Figure 1.1.

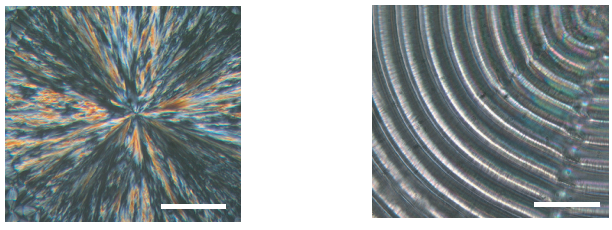

Figure 1.1: Left: Spherulite of pure PCL. Right: Spherulite of PCL/PVB. Under polarized optical microscopy, Scale bar: 50 μm.

The mechanism by which achiral structure at molecular level acquires chirality at higher order structure is intriguing. The purpose of our research is to investigate the nano-structure which triggers the formation of banding structure. The origin of lamellar twisting has been extensively researched for a half century; however, unified theory has not been established [20]. It is explained in one of the theories that foundation to pro-

voke the break of structural symmetry is that chains are obliquely folded against lamellar normal [20]. However, simultaneous observations of chain tilt and twist sense in intact spherulite, which gives decisive information to ensure the chain tilt has not been achieved.

Another issue regarding lamellar twisting has been reported in previous works [1], where the phase of lamellar twist proceeds non-uniformly. We also set our aim to clarify the mechanism of stepwise lamellar twisting by the structural analysis of lamellar twisting.

One of the powerful tools to investigate the nano-structure of material is x-ray scattering measurement. Lamellar structure and crystal packing structure can be analyzed by small angle x-ray scattering (SAXS) and wide angle x-ray scattering (WAXS), respectively. Polymer crystal sometimes has inhomogeneity of micrometer order, the information of which is averaged by conventional x-ray scattering measurement where the beam size is several hundred micrometers. By reducing the beam size to micrometer order, local information such as the lamellar orientation and the chain tilt to lamellar normal inside single banding can be obtained. Microbeam scattering measurement requires light sources of synchrotron facility with high brilliance. The structure of the anisotropic material, such as polymer crystal, can also be analyzed by POM.

In this work, two samples of PCL/PVB blend and Poly-(vinylidene fluoride)/Poly-(ethylene acrylate) (PVDF/PEA) blend are at play. Both PCL and PVDF are achiral polymer. The former blend system shows extremely cooperative banding structure as described above. Pure PVDF exhibit banding with considerable short period of μm order. In the case of PCL, cooperative lamellar twisting is achieved only when diluents such as PVB or PVC are blended [49].

Finally, outline of this thesis is summarized. In this thesis, the observation of the lamellar twisting will be presented, with the purpose to elucidate the mechanism of lamellar twisting and its non-uniformity. Chapter 2 describes the previous reports regarding the mechanisms of lamellar twisting and related topics. The purpose of research and linkage between previous works are summarized in Chapter 3. Then, the fundamentals of x-ray scattering and POM are reviewed in Chapter 4, which are the basis for analyzing lamellar twisting. Chapter 5 describes the synchrotron radiation and related instrumentation which are the essential tools in the experiment. The experimental method is presented in Chapter 6. Then, the analytical method of lamellar twisting, particularly focusing on the determination of the stepwise twisting is discussed in Chapter 7. The observation results, the interpretation, and the discussion of the mechanisms of lamellar twisting and its non-uniformity are presented in Chapter 8.

Chapter 2

Lamellar twisting

2.1 Hierarchical structure of Polymer crystal

In this section, crystalline structure of polymer is briefly summarized [2][3][4]. Hierarchical structure exists in polymer crystal; crystal packing structure of the angstrom order, lamellar structure where crystal layer and amorphous layer appears alternatively in 10 nm order, spherical crystal (spherulite) of the micrometer structure.

2.1.1 First order structure of polymer crystal

Development of the crystal largely depends on steric regularity and compactness of molecular structure of polymers. Among hydrocarbon polymers, only isotactic and syndiotactic polymer crystallize with a few exceptions. If side group is small like polyethylene (PE), polymer chain arranges in planar zigzag form. Bulky side groups causes polymer to take spiral shape (helix), minimizing the steric hindrance. When m monomer units exist during n times rotation, it is called m/n fold helix. Sense of the helices sometimes determines the chirality of the higher order structure [20]. In terms of chirality, we can also classify polymers by the existence of asymmetrical carbons. The grouping of polymers is summarized in Figure 2.1.

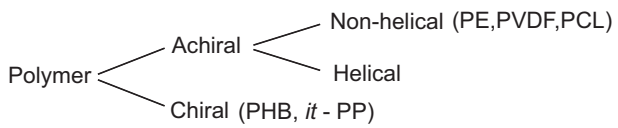

Figure 2.1: Classification of polymer by first order structure. PE: Poly-(ethylene). PVDF: Poly-(vinylidene fluoride). PCL: Poly-(ε caprolacton). *it*-PP: isotactic Poly-(propylene). PHB: Poly-(hydroxybutyrate)

2.1.2 Higher order structure of Polymer crystal

Crystallization process can take place at solution or at melt. Single crystal with full degree of crystallinity forms from dilute solution. By contrast, partially crystallized spherical crystal (spherulite) grows under melt crystallization. In a practical sense, spherulite characteristic is of significant concern, because almost all of plastic materials are made from melt polymer. For example, the size of spherulite affects on the mechanical strength and transparency of the material. Nucleation agents are used to increase the number of spherulite and reduce its size.

Single crystal

It was only in 1957 that Keller discovered polymer single crystal by slow precipitation from xylene solution. The crystal is lozenge-shaped, where chains were found to be normal to the substrate by electron diffraction. The growth front consists of (110) facet. After that, full investigation of the single crystal revealed that the crystal is not flat, as Keller initially suggested, but takes the from of pyramidal or chair like crystal as illustrated in Figure 2.2.

Single crystal has much in common with spherulite. For example, the embryo of spherulite is akin to the single crystal. Facets of spherulite growth front is said to be the same as that of single crystal.

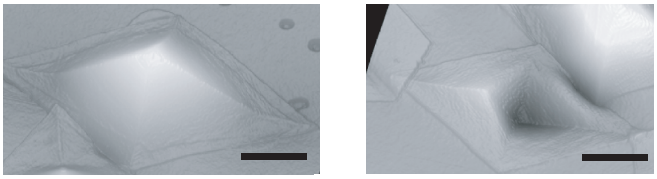

Figure 2.2: Left: Pyramidal single crystal. Right: Chair like single crystal. Scale bar: 1 μm. [33]

Spherulite

When the polymer is crystallized from condensed system, the crystal takes spherical morphology which is totally different from single crystal. Melt crystallization occurs under relatively large supercooling (ΔT) because of polymer entanglements. At the initial stage of crystallization, spherulite is akin to single crystal, and then the crystal begins to branch and fan out until it takes lath-like shape (axialite, hedrite, shown in Figure 2.3) which eventually develops into spherulite. The growth lasts until spherulites impinges on each other.

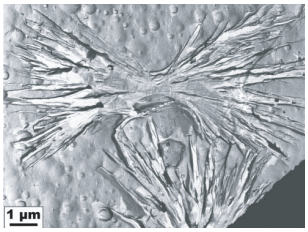

Figure 2.3: Axialite, an embryo of spherulite. [39]

From electron microscopy and x-ray scattering measurement, it was confirmed that spherulite is composed of flat crystals which are called lamellae. Lamellae arrange periodically, among which amorphous layer exist where non-crystallizable molecules are accumulated, such as loops of folded chain, atactic polymer, small molecular weight fragment, impurities. This crystal and amorphous alternating layer structure is also referred to as lamellar structure (Figure 2.4). Chain axis was found to be perpendicular to the radial direction of spherulites by the microbeam X-ray diffraction [6]. Compared with single crystal, lamellar crystal is less ordered.

The difference of monomer crystal and polymer crystal is that the polymer traverses many unit cells. Lamellae are tightly joined each other by the traversing molecules. This tight junction among lamellae affects the mechanical tolerance of the material.

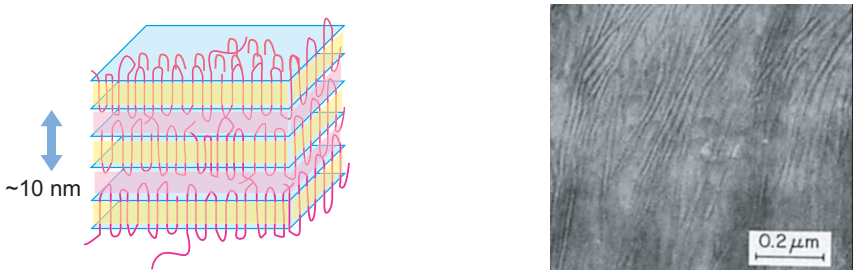

Figure 2.4: Left: Schematic view of lamellar structure. Yellow and pink correspond to crystal phase and amorphous phase. Right: TEM image of lamellae.

Cross-shaped extinction pattern (Maltese cross) is observed in spherulites under polarized optical microscope (Figure 2.5). Some of spherulites shows extinction rings, which indicates the cooperative rotation of lamellae in the radial direction.

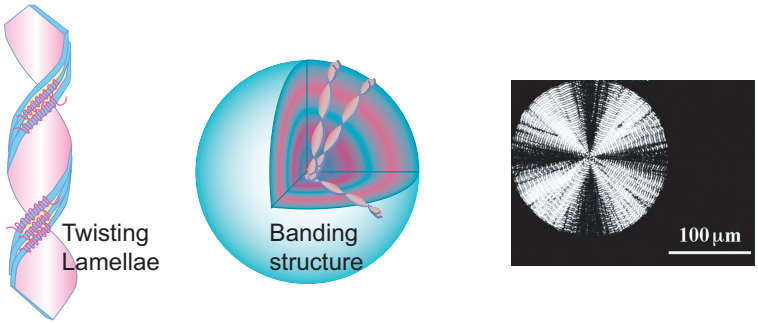

Figure 2.5: Left: Twisting lamella. Center: Banded spherulite composed of twisting lamellae. Right: Maltese cross pattern under polarized optical microscope.

2.1.3 Hierarchical structure of polymer crystal and x-ray scattering

X-ray scattering is one of the powerful tools to analyze the hierarchical structure of polymer crystal. As Bragg formula $\lambda = 2d \sin\theta$ indicates (where λ is wavelength, 2θ is scattering angle, and d is structure scale), the periodicity of lamellar structure of 10 nm order and that of crystal packing structure of 1 nm order can be analyzed by small angle x-ray scattering (SAXS) and wide angle x-ray scattering (WAXS), respectively (Figure 2.6).

While many polymeric materials have spatial inhomogeneity on a micrometer scale, conventional x-ray scattering has drawback in that we can only obtain the averaged structure of the area irradiated by x-ray beam of several hundreds of micrometer. This problem has been overcome with the advent of recent synchrotron radiation and focusing devices which enabled the microbeam x-ray scattering measurement [5]. In addition, imaging techniques such as TEM and AFM still bears difficulties in the in-situ observation of structural change of micrometer scale. X-ray scattering has an advantage that time-resolved x-ray scattering measurement can trace the time-lapse change of the structure during crystallization or deformation process.

By contrast, Fourier transformed image does not uniquely determine the structure in real space. Complementary information from real space observations are essential to abandon such ambiguity.

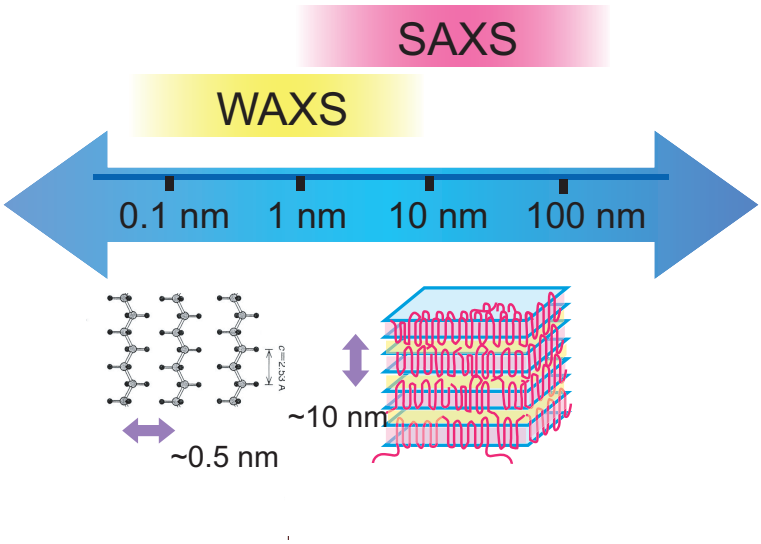

Figure 2.6: Hierarchical structure of polymer crystal and x-ray scattering.

2.2 Development of lamellar structure

Polymer crystallization is totally different from that of monomer. Monomer crystallization converges toward thermodynamically stable state, in contrast, polymer crystallization is governed by kinetics. In order to crystallize regularly, chain molecules have to wind off the entanglement and overcome the high entropy barrier. Therefore, polymer crystal does not reach the thermodynamically stable state, and it only partially crystallizes from the melt. In this section, kinematical theory of polymer crystallization is reviewed [2][7]. Lamellar branching, which is necessary for the three dimensional expansion of spherulite, is also briefly summarized.

2.2.1 Driving force of crystallization

Crystallization is a phase transition of a fist kind as illustrated in Figure 2.7. Under constant pressure, Gibbs free energy of crystal phase and liquid phase cross at the melting point.

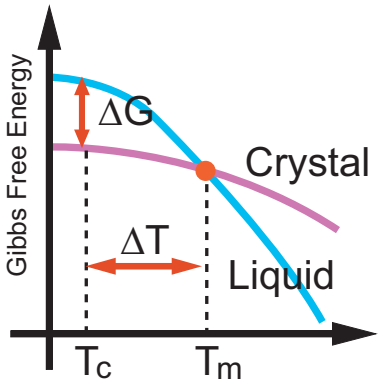

Figure 2.7: Linear approximation of phase transition

When the liquid phase is quenched below the melting point, metastable liquid phase changes into more stable crystal phase. The driving force of crystallization is the difference of Gibbs free energy ΔG, which depends on the degree of supercooling $\Delta T = T_m - T_c$.

$$G = H_c - T_m S_c = H_l - T_m S_l \tag{2.1}$$

$$\therefore \Delta H = T_m \Delta S \tag{2.2}$$

where H and S are enthalpy and entropy. Notation l and c mean liquid phase and crystal phase, respectively. The driving force of crystallization ΔG_c is proportional to the degree of supercooling in the first approximation as follows.

$$\Delta G_c = \Delta H - T_c \Delta S = \Delta H \frac{\Delta T}{T_m} \tag{2.3}$$

Besides the driving force of the crystallization, we have to take into account the interface energy, which inhibits the nucleation. Assuming the spherical nuclei, total shift of free energy can be written as

$$\Delta G = -\frac{4\pi}{3} r^3 \Delta G_c + 4\pi r^2 \sigma \tag{2.4}$$

First term is the decrease of free energy by the crystallization, and the second one is the interfacial energy. The maximum of the function corresponds to the critical size of nuclei.

$$r_c = \frac{2\sigma}{\Delta G_c} \propto \frac{1}{\Delta T} \tag{2.5}$$

Steady growth are allowed only in the nucleus whose size are over the critical size r_c. Under less degree of supercooling, therefore, nucleation frequency decreases. This process is called primary nucleation to distinguish from that which occurs on the crystal surface as explained in the following.

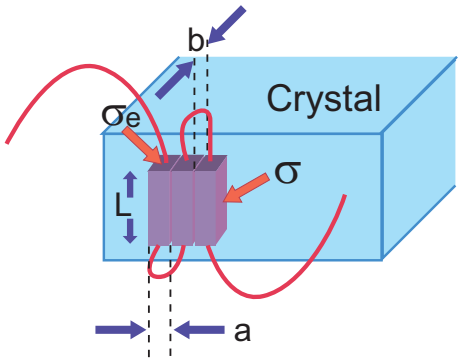

Figure 2.8: Secondary nucleation at the spherulite growth front.

When the molecules adsorbs onto the flat crystal face, they have to get through the free energy barrier deriving from the lateral surface free energy σ and upper surface energy σ_e. This process is called secondary nucleation (Figure 2.8). When the nuclei whose length is ℓ and the number of stems is n appears, the shift of total free energy $\Delta G(n, \ell)$ is written as the following, where Δg is the gibbs free energy decrease per unit volume, a and b are the width and height of the stems, respectively.

$$\Delta G(n, \ell) = -\ell nab\Delta g + nab2\sigma_e + 2\sigma\ell ab \tag{2.6}$$

The form of Equation 2.6 implies the existence of saddle point, which corresponds to the critical nucleation size. Using partial differentiations, following formula are derived.

$$n^* = \frac{2\sigma}{a\Delta g} \qquad \ell^* = \frac{2\sigma_e}{\Delta g} \tag{2.7}$$

2.2.2 Dependence of growth speed and lamellar thickness on supercooling

The dependence of radial growth speed V on temperature is written as the product of the term which reflects the mobility of the molecules β and the term of secondary nucleation. The friction of the molecules increases under low temperature near the glass transition temperature T_g, and the entropy effect is more pronounced under high temperature near melting point, both of which result in slow growth.

$$V \propto \beta \exp\left(-\frac{A}{T\Delta T}\right) \tag{2.8}$$

$$\beta \propto \exp\left(-\frac{B}{T - T_v}\right) \tag{2.9}$$

where T_v is Vogel temperature defined as $T_v = T_g - 51.6$ K, A and B are constant.

Lamellar thickness depends on the degree of supercooling as to which below formula is known.

$$d_c(T) = \delta l + \frac{A}{\Delta T} \tag{2.10}$$

Laurenzian-Hoffmann theory gives clear explanation of the above formulas. In this model, the stem length of the lamellae is assumed to be constant during the crystallization. The frequency of the secondary nucleation $S(\ell)$ with stem length ℓ is calculated about each ℓ. Total growth is the written as the integration of $S(\ell)$ about each ℓ, which is over the critical length ℓ^*. Mean lamellar thickness ℓ can be calculated by weighing the $S(\ell)$ onto each ℓ.

$$I = \int_{\ell^*}^{\infty} S(\ell) d\ell \tag{2.11}$$

$$\langle \ell \rangle = \frac{\int_{\ell^*}^{\infty} \ell S(\ell) d\ell}{\int_{\ell^*}^{\infty} S(\ell) d\ell} \tag{2.12}$$

If surface nuclei of the thickness ℓ grows, free energy changes as in the diagram illustrated in Figure 2.9. The free energy reaches the maximum when the first stem crystallizes.

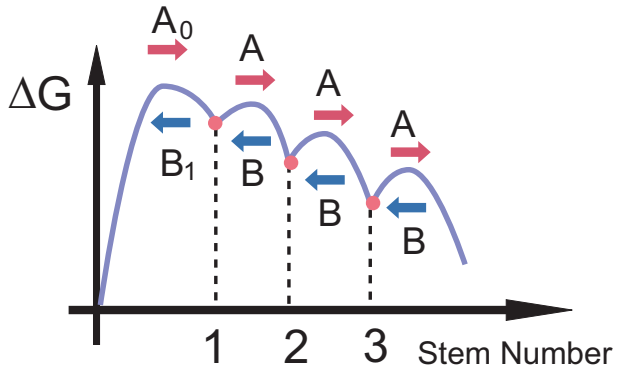

Figure 2.9: Transition of ΔG at initial stage of crystallization

The term A_0, B_1, A and B are the transition frequency. β is the chain mobility factor in the Equation 2.8. A_0 is given in the following because the interface term is the predominant factor.

$$A_0 = \beta \exp\left(\frac{-2b\sigma\ell}{kT}\right) \tag{2.13}$$

The step where stem number increase does not entail the increment of the lateral interfacial energy. The terms of top and bottom surface interfacial energy appears as follows

$$A = \beta \exp\left(\frac{-2ab l\sigma_e}{kT}\right) \tag{2.14}$$

B_1 and B can be written as following, considering the energy to separate from the crystal.

$$B_1 = \beta \exp\left(\frac{-abl\Delta g}{kT}\right) \tag{2.15}$$

$$B = \beta \exp\left(\frac{-abl\Delta g}{kT}\right) \tag{2.16}$$

The rate determining step of crystal growth is the one where chain attaches on the crystal and the makes new stem. Therefore, the frequency of the secondary nucleation with stem length ℓ is given as

$$S(\ell) = A_0 \frac{A - B}{A - B + B_1} = A_0\left(1 - \frac{B}{A}\right) \tag{2.17}$$

The integrations in Equation 2.11 and Equation 2.12 give the total crystal growth and mean lamellar thickness.

$$i \propto \beta \exp\left(-\frac{4b\sigma\sigma_e}{kT}\right) = \beta \exp\left(-\frac{K}{T\Delta T}\right) \tag{2.18}$$

$$\langle \ell \rangle = 2\frac{\sigma_e}{\Delta g} + const \tag{2.19}$$

these Eqation 2.18 and 2.19 are consistent with the Equation 2.8 and 2.10.

2.2.3 Regime transition in polymer crystallization

Several modes of spherulitic growth are known. The growth mode can be classified into the single nucleation growth and multi-nucleation growth depending on the balance between the frequency of secondary nucleation and lateral growth speed. Laurentizan introduced the nondimensional parameter $z = iL^2/4g$ to compare these two factors, where i is the nucleation frequency per unit time and unit length, L is the lamellar width, g is the lateral growth speed. Single nucleation mode and multi-nucleation correspond to the cases where $z << 1$ and $z >> 1$, respectively. The growth speed V is given as follows, combining with the equation 2.11.

$$V = biL \propto \beta \exp\left(-\frac{K}{T\Delta T}\right) \tag{2.20}$$

$$V = b\sqrt{2ig} \propto \beta \exp\left(-\frac{K}{2T\Delta T}\right) \tag{2.21}$$

The relationship between the modes of growth and morphology of spherulite is suggested in the case of Poly-(ethylene) [8] [9]. At higher crystallization temperature above 127 ℃

(Regime I), branching frequency decrease, and crystal forms axialite. Banded spherulites appears at lower crystallization temperature (Figure 2.10).

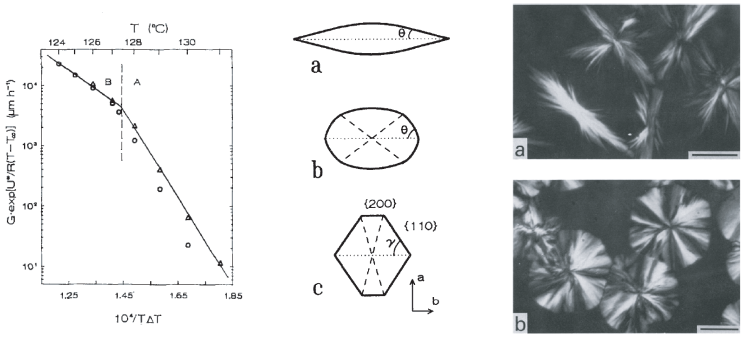

Figure 2.10: Regime transition of polyethylene. Left: Discontinuous change of growth speed depending on crystallization temperature. Center: Morphology of single crystal corresponding to growth regime. Right: Axilate at high Tc (top) and spherulite at low Tc (bottom) [8]

2.2.4 Lamellar branching

Lamellar branching is a requisite for the three dimensional development of spherulite as briefly mentioned in Section 2.1.2. It has been proposed by Keith and Padden that the lamellar branching derives from concentration field of impurities at the growth front [10][11]. Industrial polymers have molecular weight distribution, which entails uncrystallizable and diffusive molecules. According to this theory, the distribution of such impurities $C(x)$ at position x is assumed to exponentially decrease, depending on the diffuse coefficient D and growth rate G of the spherulite.

$$C(x) = \Delta C \exp(-Gx/D) + C_\infty \tag{2.22}$$

where C_∞ is the concentration at infinitely remote position, and $\Delta C = C(0) - C_\infty$. Near the growth front, equilibrium melting point $T_L(x)$ is depressed by the concentrated impurities. If the enthalpy stemming from the polymer attachment diffuses away in the crystal phase, the temperature profile around the growth front is like in Figure 2.11(a). Under such condition, supercooled region occasionally appear, where temperature $T(x)$ is below $T_L(x)$ as illustrated in Figure 2.11(b). Dimension of the supercooled region $\delta = D/G$ is a determinant of the critical size of lamellae. When the lamellae width reaches the critical size, the branching occurs.

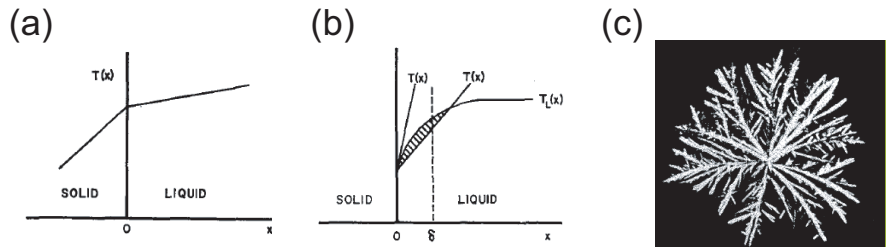

Figure 2.11: (a) Temperature profile at the growth front. (b) The equilibrium melting point $T_L(x)$ is occasionally below the temperature [10]. (c) Dendritic crystal of isotactic poly-propylene when the uncrystallizable component is superior [11].

Furthermore, they advocate that the parameter δ also affects the frequency of lamellar branching. Larger δ value leads to less frequency of lamellar branching. The extreme case is the dendritic crystal as shown in Figure 2.11(c). The orientation is randomized compared with the compact spherulite because of the free space among the fibrils.

The drawback of the above theory is that the effect of the interfacial tension, which stabilizes the planer growth front, is not taken into account. This point was overcome by Goldenfeld, who concluded that the critical width was proportional to $\sqrt{\delta}$. Further expansion was brought by Toda. According to the theory [12][13], the band width is determined by the critical size. In either case where the main contribution of lamellar twist may be unbalanced surface stress or screw dislocation as summarized in Section 2.3.2, the rigidness of lamellae, which leads to the difficulty of lamellar twisting, is proportional to lamellar width. Therefore, the bandwidth is proportional to the critical width of lamellae. However, it has been reported that this theory cannot be applied to polyester polymers, such as PCL/PVB and PLLA [12], in that the bandwidth is relatively constant regardless of the degree of supercooling [88].

2.3 Twisting lamellae

Twisting of lamella still remains a topic of research and controversy [20][21]. It may be difficult to establish unified theory to explain the origin of lamellar twisting, because the phenomena is widely observed in the material science not just for polymer crystal. Here, prevailed theories about the mechanism of lamellar twist are reviewed.

Polymers can be roughly classified by the existence of chirality as summarized in Section 2.1.1. In the case of chiral polymer, the chirality of the polymer chain may well propagate to the higher-order structure and determine the lamellar twist sense. However, the mechanism by which achiral polymer acquires chirality at higher order structure is quite complicated and intriguing.

In chiral polymer spherulite, the twist sense is uniform in the whole spherulite [32]. In the case of achiral polymer, coexisting of both handedness of lamellar twist is confirmed by microbeam x-ray scattering measurement by Nozue [23], and AFM observation by

Toda [34]. It is deduced by Toda that the achiral polymer spherulite is divided into two regions of left handed twist and right handed twist [34].

In this work, the twisting mechanism of achiral polymer crystal is of interest. This topics were thoroughly surveyed. Associated topics such as lamellar twisting of chiral polymer and S-shaped lamellae are also briefly referred.

2.3.1 Observation of twisting lamellae and the chain tilt

Twisting lamellar structure is sometimes observed in polymer crystal from melt. Etching techniques pioneered by Keller and Bassett et al, enabled investigation of internal structure of spherulite and observation of individual twisting lamellae (Figure 2.12).

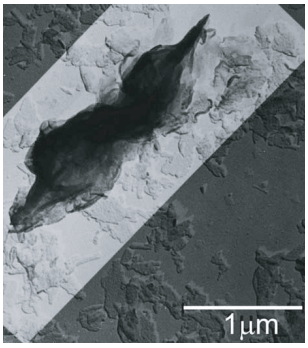

Figure 2.12: Rotating lamellae of Poly-ethylene [20]

When dealing with lamellar twist, both twist sense and twist periodicity is to be determined. The periodicity is easily determined by POM. There are several measures for the identification of the twist sense, which is critical information correlated with structural features such as chirality of polymer and chain tilt.

Result of universal stage is shown in Figure 2.13, where the spherulite is tilted around spherulite radius [89]. Rotating the sample corresponds to change the phase of twist, which leads to the shift of the bandings of the POM image. It was firstly confirmed by Fujiwara that *c* axis of crystal, which are parallel with the folded chain, rotates along radial direction by microbeam x-ray scattering [24].

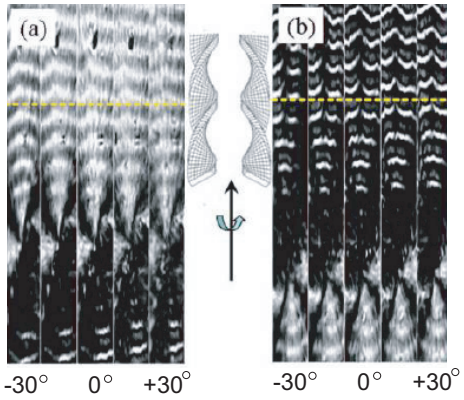

Figure 2.13: Determination of the sense of lamellar twist with POM [89]. The position of banding changes depending on the rotational angle of the sample. (a) Right handed screw. (b) Left handed screw.

Relating to lamellar twist, chain tilt to with respect to lamellar normal is generally determined by electron diffraction of single crystal from melt or solution, as illustrated in Figure 2.14. As explained in the following section, the chain tilt is said to be the key factor for achiral polymers to develop into the chiral structure [30]. Single crystals from melt or solution are rotated against the incident beam, and the orientation of folded chain is analyzed from the diffraction patterns. When we evaluate the chain tilt, single crystal from melt, not from solution need to be prepared [35]. The chain tilt is expected to be less under solution crystallization which entails low crystallization temperature and more free space around lamellar surface.

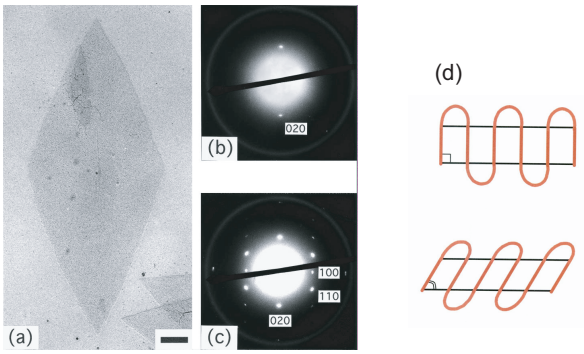

Figure 2.14: The electron diffraction pattern of PVDF single crystal. Scale bar of the optical microscope (a) is 0.5 μm. (b) When the specimen is normal to the incident beam, only 0k0 reflection are observed. (c) When it is tilted around *b* axis, hk0 diffraction appear. This indicates the tilted chain orientation to lamellar normal as illustrated in (d) [22].

2.3.2 Lamellar twisting of achiral polymer

There are four theoretical mainstreams about the origin of lamellar twist of achiral polymer

- Concentration field
- Screw dislocation model
- Unbalanced surface model
- Re-organization model

In this section, polyethylene frequently appears as an exemplar because it is the most simple polymer which exhibit banded spherulite, and often used as model sample in many research. Also, it has orthorhombic unit cell, which is the same as PCL and PVDF.

Concentration field

According to the theory, it is assumed that ahead of lamellar growth front is more susceptible to polymer depletion than above or bottom side of lamellae [31]. This causes lamellar twist to reach more concentrated area.

This theory is criticized in two points. Firstly, this model cannot account for the selectivity of twist sense and coherence of the twist. The second point is that this theory is too general in that it cannot give an explanation to the crystalline polymorphism such as PVDF and isotactic poly(1-butene). For example, PVDF can crystallize in α from and γ form under the same condition, but they exhibit different lamellar twist manner.

Screw dislocation model

Screw dislocation, which accompanies lamellar branching, is necessary for three dimensional expansion of spherulites. Bassett stresses that the major contribution of lamellar twist stems from the queues of screw dislocation, which entails the quantum increment of the twist phase [41][39] as illustrated in Figure 2.15. The surface pressure, which gives rise to the dislocations, was deduced to be caused by cilia protruding from lamellar surface. Another explanation of lamellar twist is the repulsion between parent lamellae and daughter lamellae [30]. The isochirality of the dislocation is the result of uniformly oriented chain tilt.

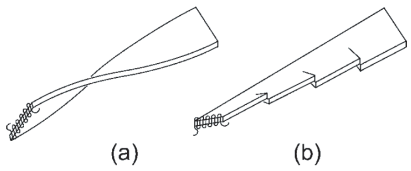

Figure 2.15: (a) Continuous lamellar twist. (b) Discontinuous lamellar twist by isochiral dislocation [12].

Toda suggests the correlation of screw dislocation and the chair like single crystal from melt [33][34][35]. Both pyramidal and chair like single crystal forms at the same ratio from solution, whereas single crystal from melt is invariably chair like [35]. Lamellae twist to relax the strain stress at the boundaries where the two half crystal are connected together as illustrated in Figure 2.16. The twist sense of the screw dislocation remains the same in the whole spherulite.

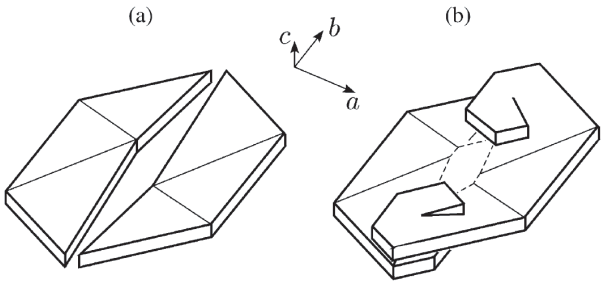

Figure 2.16: Chair like crystal and screw dislocation [35]. (a) Convex and concave lamellae are united. (b) Screw dislocation generates to relax the strain energy.

Keith *et al* put on emphasis that the screw dislocation cannot be the major factor of lamellar twist, admitting its essential role of space filling [20][27]. They point out that the screw dislocations develop not at growth front as Toda indicates, but at the boundaries of lamellae where the strain energy reaches maximum. He insists that it is impossible to account for tight twist of pure PVDF whose period is 1 μm considering the dimension of Burgers' vector. More critical and apparent counterexample is the single lamellar twist as shown in Figure 2.17 [21]. If the discontinuous model is correct, the lamellar twist appears only in multilamellar entity, which is inconsistent with the observation results.

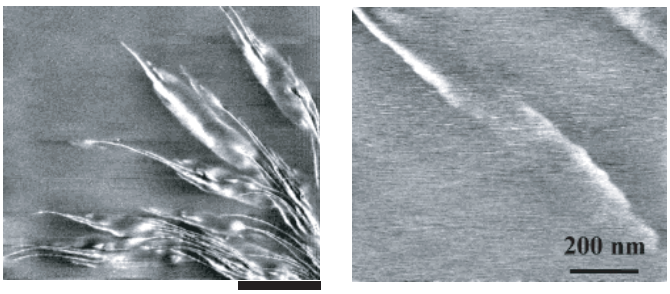

Figure 2.17: AFM image of twisting lamellae of Poly (3-hydroxybutyrate-co-hydroxyhexanoate) [29]. Note that it is chiral polymer.

Unbalanced surface stress by chain tilt

In this theory, polymer chain is assumed to be folded in the direction inclined to lamellar normal at the growth front [26][30]. When lamellae grow laterally, longer polymer chain

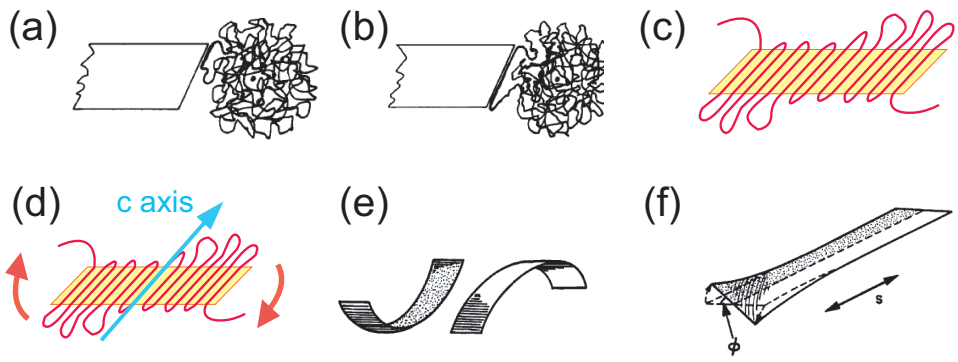

Figure 2.18: Lamellar twisting mechanism based on unbalanced surface stress [26]. (a)(b)Isolation of polymer from entanglement. (c) chain tilt with respect to lamellar normal. (d) The chain tilt and its correlation with the twist sense. (e) Half-split lamellae. (f) Lamellar twist to relax the surface stress.

has to be isolated from entanglement at obtuse angle compared with at acute angle as described in Figure 2.18(a)(b). Therefore, relatively loose loops form at acute angle, where pressure is pronounced (Figure 2.18(c)). The unbalanced fold surface causes the lamellar twist (Figure 2.18(d)). As a consequence of the pressure difference at the opposing side of lamellae, if the lamellar is spared in the growing direction, the split lamella will induce lamellar curvature in opposite direction (Figure 2.18(e)). In bulk crystallization, however, the half lamellae are connected together, hence lamellae twist to relax the surface stress (Figure 2.18(f)). The mechanism of the cooperativity of lamellar twisting is explained as lamellar interlocking [26].

In this context, the tilting angle increases under higher crystallization temperature, because augmented chain mobility leads to longer loops with higher degree of freedom and the increase of tilting angle. Low crystallization temperature and fast growth causes more asymmetric structure because the chain at obtuse angle cannot have enough time to loosen the entanglement. Therefore, although the chain tilt is the requisite for the twist, more tilting angle does not mean more twist. In addition, larger molecular weight increases the unbalanced surface stress, which leads to shorter band spacing.

There are several reports supporting Keith model showing the winding half-split lamellae as shown in Figure 2.19 [28]. When PE is crystallized in thin film under high crystallization temperature, lath like crystals with hooks on its surface appears [28]. Chain tilt by 45 degree was confirmed by electron diffraction. The flat lamellae split during the growth and the split lamella rotates 90 degree and forms the hook shaped lamellae whose curvature radius is about 5 μm (Figure 2.19(a)(b)). This result may support the theory of the unbalanced surface stress.

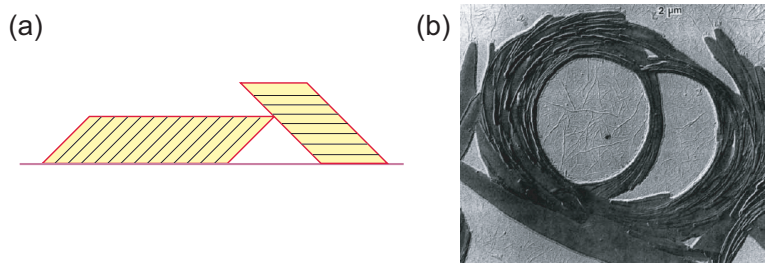

Figure 2.19: Supportive observations of Keith model. (a) Schematic view of the split and rotated lamellae. (b) Hook shaped lamellae composed of half-split lamellae.

Re-organization of fold surface

The theory of unbalanced surface stress is not accord with Bassett interpretation, where the screw dislocation is the major contribution of lamellar twist. The unbalanced surface theory does not hold true for the regime I and II transition of poly-(ethylene) (Refer Section 2.2.3). PE shows banding only when crystallized under below 127 °C, and does not show banding when grown at low supercooling condition. However, in both cases, chain tilts to lamellar normal. This contradiction is resolved by Bassett as follows [36][37][38].

At the growth front, lamellar plane coincides with (001), in other words, chain does not tilt. After chain attachment to the lamellae, chain tilts and structural re-organization occurs until it reaches entropically stable state with chain tilt. At high crystallization temperature, chains have enough time to tilt and the re-organization is over before the attachment of next molecule. At low crystallization temperature, the chain deposit on growth front before the re-organization completes, which involves re-organization behind the growth front (Figure 2.20). The chain tilt causes the screw dislocation and lamellar twist.

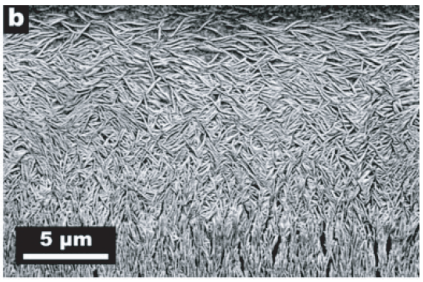

Figure 2.20: SEM image of spherulite growth front of PE. The spherulite grows down in the image. Lamellae takes S-shaped morphology as time passes, which indicates the re-organization behind the growth front [36].

2.3.3 Lamellar twisting of chiral polymer

Lamellar twisting mechanism of achrial polymers was reviewed in the above. Here, the lamellar chirality stemming from the molecular level chirality is reviewed. Regardless of the chain tilt, lamellae of chiral polymer may well twist, because most of chiral polymer exhibit helix crystal structure.

Keller concluded that the molecular chirality propagates to higher order structure, and that it determines the lamellar twist sense [32]. Li et al propose another chirality cascade; the molecular level chirality is strongly correlated with the chirality of helix hand of the crystal, and it is correlated with lamellar chirality [20].

However, these empirical rules have some exemptions. Chains are normal to the lamellar sureface in crystal of nonracemic chiral polyester poly (ethylene trephtalate9). If the enantiomer is changed from all R to S, lamellae twist in opposite direction. However, the twist sense can also be changed by the length of residue. Samples PET(R*-9) and PET(R*-11) produce crystal with right handed twist, whereas PET(R*-10) produces crystals with right hand twist. Another counterexample is the case of PHB and PHV, the difference of which are the size of the residue attached to chiral carbon. Both PHV and PHB have the helix of the same hand, whereas the lamellar twist sense is opposite [20].

2.3.4 S-shaped lamellae and lamellar twisting

S-shaped lamella was found by Bassett in PE. It has been reported that the S-shape tends to appear with higher molecular weight and lower crystallization temperature [43]. Here, the mechanisms of the formation of S-shaped lamella by Keith and by Toda are reviewed.

Bassett reported the unique correlation of the twist sense and the S-morphology; lamellae rotates along the radial growth direction while scooping up the melt [40] (Figure 2.21). This phenomenon is explained by the unbalanced surface pressure theory by Keith and Padden, which bends the lamellar. Toda indicates that S-shaped lamellae originate from the screw dislocation from chair type crystal whose cross section takes S-shaped morphology [9].

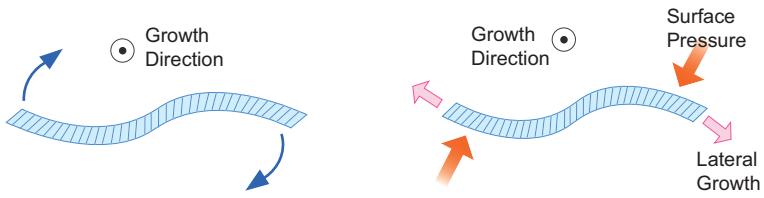

Figure 2.21: Left: The correlation between the sense of lamellar twist and that of S-shape. Right: Formation mechanism of S-shape by Keith and Padden

Above two models agrees in the correlation of chain tilt and twist sense. It contradicts, however, with respect to the correlation between S-shape and twist sense as illustrated in Figure 2.22 [22] (Refer Section 3.1.1).

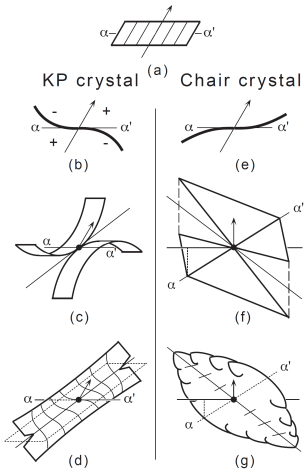

Figure 2.22: Opposing models regarding the formation of S-shape lamellae and its correlation with the chain tilt and twist handedness [22]

2.4 Samples of our research

2.4.1 PCL/PVB

Poly ε-caprolacton (PCL) is a biodegradable polyester which has the chemical stuture of $[-O-(CH_2)_5-CO-]_n$. It is miscible with various kinds of polymer because of its hydrophobic methylene group and hydrophilic ester group [50]. The melting point and glass transition temperature are about 333 K and 213 K, respectively. There have been numerous reports about PCL blends, such as PCL/PVC [49], PCL/SAN [15], and PCL/PHB. The crystal structure is orthorhombic as shown in Figure 2.4.1, where chains are in zigzag conformation like PE. Slight deviation of carbonyl group from the zigzag plane has been reported by Chatani et al [51].

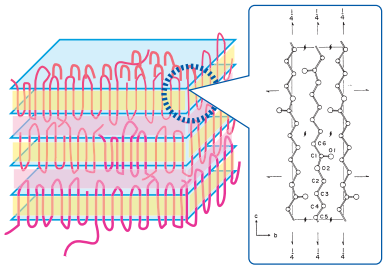

Figure 2.23: Crystal structure of PCL. *c* axis is longer than other axis by more than two times

Although pure PCL shows little banding structure, several studies indicate that PCL exhibits coarse banding structure at relatively high crystallization temperature [49][53].

The correlation between the morphological transition from no banded spherulite to banding spherulite and the Regime transition from II to III has been suggested [52].

In this work, we deal with PCL/PVB blend system introduced by Keith et al, which exhibits extremely cooperative banding structure [49]. In general, banding structure does not change until blend material is added in the order of 10 percent, however, PVB turns random twisting of PCL into clearly cooperative twisting only by adding 0.5 percent. The mechanism of cooperativity is suggested to be that the interlocking lamellar structure of PCL is tightly fixed by the bridging PVB molecules between PCL lamellae. Band periodicity is considerably affected by the PVB concentration. Also, it decreases a little under higher crystallization temperature [55]. In addition, two kinds of lamellar structure have been reported [49]. More than one kind of lamellar structure is rare in polymer crystal. Polymer blends can be classified into crystal/crystal, crystal/amorphous, and amorphous/amorphous. Although some of the crystal/crystal blend shows several kinds of lamellar structure [47][48], PCL/PVB is the exclusive system of crystal/amorphous blend in this respect.

2.4.2 PVDF/PEA

Chemical structure of Poly Vinylidene Fluoride is $[-CH_2 - CF_2-]$. High melting point about 200 ℃ derives from its highly polar and not bulky structure. Several kinds of crystal structure are known in PVDF, and banding spherulites are comprised from orthorhombic α crystal [46][54]. Banded spherulite of pure PVDF has extremely short periodicity about 1 μm, which is attributed to be dipolar interaction [30][45]. In contrast, PVDF/PEA blend system shows banding in the order of 10 μm [44], which allows the structure analysis of lamellar twisting by microbeam x-ray scattering (Figure 2.24). From the electron diffraction of single crystal from the melt, it has been reported that the chain tilt against the lamellar normal is about 26 degree, regardless of the blend composition [22].

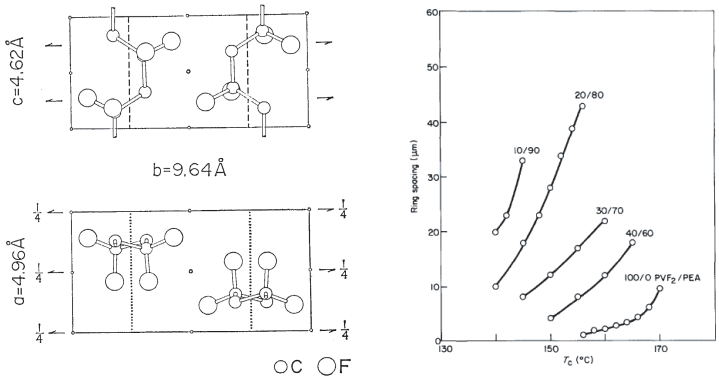

Figure 2.24: Left: Crystalline structure of PVDF [46]. Right: Bandwith of PVDF/PEA under various blend composition [44].

Chapter 3

Purpose of research

In this section, previous works [1] and remaining problems about the PCL/PVB lamellar structure are summarized. After that, outline and purposes of our research are described.

3.1 Summary of previous works

3.1.1 S-shaped lamellae

It has been reported that there are two kinds of lamellar structure of different periodicity in PCL/PVB blend system under high crystallization temperature [49]. Further investigation by microbeam-SAXS revealed that they are not parallel and that the shorter periodic lamellae fulfill Bragg condition after the longer one by 15 degree of twist phase (Figure 3.1 (Left)). Besides this result, the existence of S-shaped lamellae was indicated by 3D TEM observation [61].

From above observations, structural model can be speculated, where the two kinds of lamellae correspond to the outer region or the inner region of S-shaped lamella. As illustrated in Figure 3.1, we cannot determine the sense of the S-shape of lamellae only from the information of reciprocal space obtained by microbeam SAXS supposing that S-shaped lamellae model is true. Crystallization process was observed by microbeam SAXS to determine which of the two lamellae crystallize first, because the firstly crystallizing lamellae correspond to inner region of S-shape. However, the previous work could not be able to determine the order of their crystallization completely.

Because of the ambiguity of reciprocal space, we could not conclude which of the two contradictory models regarding the S-shaped lamella was right, if the S-shaped lamellar model was true (Refer Section 2.3.4 [22]). In this work, we assessed that further research concerning this point was difficult.

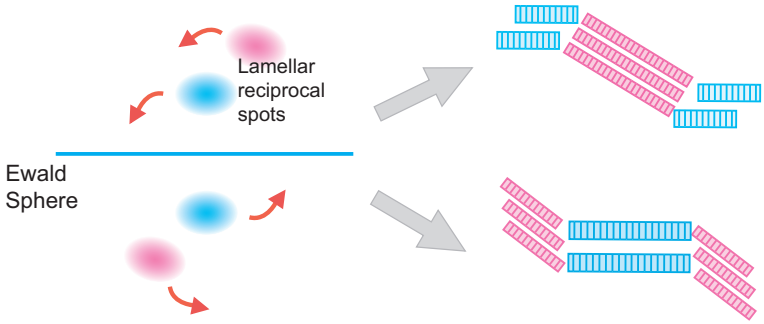

Figure 3.1: Left: Two kinds of lamellae in reciprocal space. Red arrows indicate the twisting direction of reciprocal spots of lamellae. Right: Ambiguity in real space remains even though the structure in reciprocal space is uniquely determined.

3.1.2 Stepwise lamellar twisting

In addition to the S-shaped lamella, it was found by microbeam WAXS and microbeam SAXS measurement which involves sample rotation around spherulite radius (Refer Section 7.1.5) that lamellae in PCL/PVB = 95/5 sample do not rotate uniformly along the radial direction of spherulite, when the crystallization temperature is over about 40 ℃. It was also concluded that the phase of lamellar twist proceeds slowly when they take edge-on orientation, which are perpendicular to the substrate (Figure 3.2).

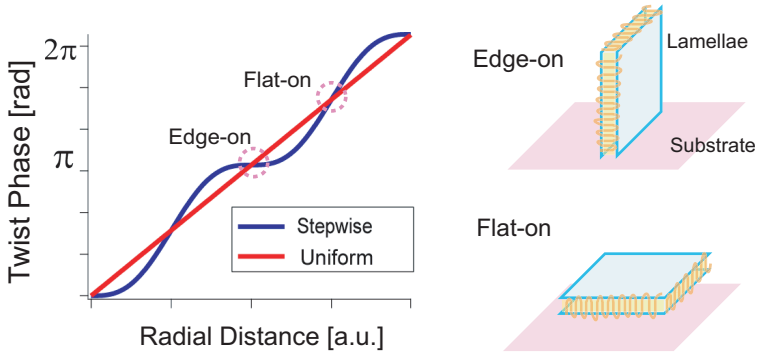

Figure 3.2: Stepwise lamellar twisting. Edge-on lamellae are perpendicular to the substrate. Flat-on lamellae are parallel to the substrate.

3.2 Purpose of this work

3.2.1 Elucidation of the lamellar twisting mechanism

In this work, the mechanism how achiral polymer PCL acquires chirality in higher order structure is one of the main concern. We try to elucidate the lamellar twisting mechanism particularly focusing on the two points as follows.

- The influence of PVB on PCL lamellar structure

Because PCL shows little banding structure without PVB, PVB molecules give critical influence on lamellar twisting. We may be able to get a clue to this question by analyzing the samples of different crystallization temperature and different concentration of PVB by microbeam WAXS and microbeam SAXS.

- The chain tilt to lamellar normal

As explained in Section 2.3.2, Keith remarks lamellar twisting cannot exist without chain tilt in achiral and non-helical polymers [30]. However, the observation method of chain tilt to the lamellar normal in intact spherulite without etching techinique [43] remains the electron diffraction of the single crystal from melt or the terrace like crystal ahead the growth front [42]. For example, chain tilt by 25 degree has been reported in PVDF/PEA blend system [22].

It seems possible to confirm the chain tilt without microbeam by comparing the lamellar thickness and stem length as reported in the case of powder diffraction [62] (Figure 3.3). Lamellar thickness can be calculated by the analysis of SAXS (Refer Section 4.1.4). The stem length can be obtained by measuring FWHM of WAXS diffraction in scattering angle direction (Refer Section 4.1.5). However, the SAXS analysis is not applicable to the sample with about 50 percent degree of crystallinity [2], and stacking number of unit cells along the *c* axis in polymer crystal is usually very small. These may result in erroneous estimation of the chain tilt. Moreover, the macrobeam scattering lose the information of the sense of lamellar twist, which is crucial to figure out the mechanism of lamellar twisting.

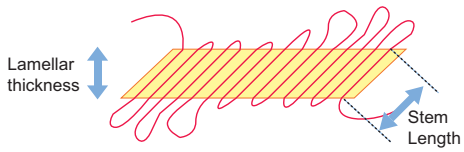

Figure 3.3: Lamellar thickness and stem length

These problems can be resolved by microbeam SAXS-WAXS simultaneous measurement. We can obtain information of the orientation of lamellae and that of folded chain comprising lamellae by SAXS and WAXS, respectively. Therefore, if the chain tilt exists, we observe the phase shift between SAXS and WAXS. For example, the maximum of the intensity profile of lamellar reflection is expected to be behind the valley of that of hk0 refletion as illustrated in Figure 3.4 when the beam scans the sample along the radial direction of the spherulite.

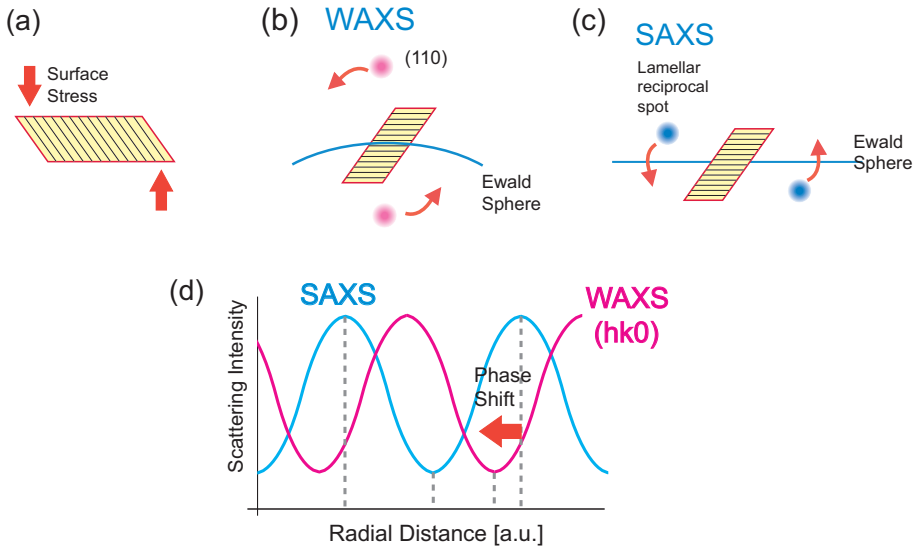

Figure 3.4: Qualitative simulation of the simulataneous SAXS-WAXS measurement. Lamellae grow perpendicular to the paper upward. If the lamellae rotate like (a), the reciprocal spots of (110) at wide angle region rotate like (b), and reciprocal spots of lamellae at small angle region rotate like (c). Therefore, the phase shift between them is expected to be observed as shown in (d).

3.2.2 Elucidation of the mechanism of stepwise lamellar twisting

Several reasons of stepwise twisting can be speculated, such as polymer-substrate interaction and/or the growth in the restricted space, for lamellae always rotate slowly when they are edge-on. To examine whether or not such possibilities are reasonable, we compare the spherulites grown from three dimensional space and that from two-dimensionally confined space (Figure 3.5). We also investigate how the PVB concentration and crystallization temperature affect the degree of non-uniformity. The correlation between the stepwise lamellar twisting and rhythmic growth was investigated by POM.

How to determine whether or not stepwise lamellar twisting exist in spherulite is detailed in chapter 7.

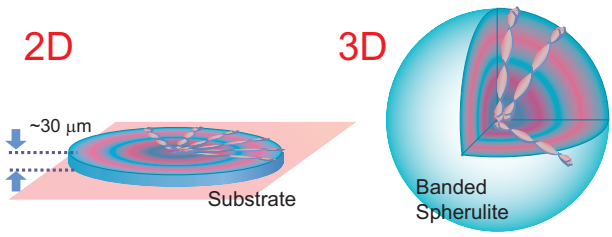

Figure 3.5: Left: Spherulite grown in two dimensional space. Right: Spherulite grown in three dimensional space.

Chapter 4

Fundamentals of x-ray scattering and polarized optical microscopy

4.1 X-ray scattering

X-ray scattering is a powerful tool to analyze the structural periodicity of matter. The characteristics of x-ray scattering are as follows;

- X-ray scattering does not need specific sample preparation for the observation.
- It is applicable to the analysis of inner structure of opaque samples with high transmittance.
- We can obtain informations from multi-scale structure at once.
- Recent advent of synchrotron radiation enabled the time-resolved and space-resolved measurement.

When certain structural periodicity d_{space} exists in a matter, strong diffraction appears in the direction such that Bragg condition

$$\lambda = 2d_{space} \sin\theta \tag{4.1}$$

is satisfied, where λ is the wavelength and 2θ is the scattering angle. The formula indicates that smaller scattering angle corresponds to bigger periodicity. In this section, the principles of x-ray scattering and the information which can be deduced from the analysis of the scattering pattern are described [64][65][67].

4.1.1 Kinematical diffraction theory

Unless we deal with highly crystallized materials, the x-ray scattering can be written in the framework of kinematical diffraction theory [71], where incident x-ray is not assumed

to be scattered more than once in the matter. We also assume that the distance between sample and detector is long enough for Fraunhofer approximation.

When incident x-ray is irradiated, electrons are forced to vibrate by the electric field of x-ray, and emit electromagnetic wave. The diffraction from sample is the superposition of the scattering from each electron. Here we define the wavevector of incident wave and that of scattered wave as $\boldsymbol{k_i}$ and $\boldsymbol{k_s}$, respectively, and the scattering vector as the difference between the two $\boldsymbol{q} = \boldsymbol{k_s} - \boldsymbol{k_i}$. The electron density at $\boldsymbol{r}$ is $\rho(\boldsymbol{r})$. Total scattering from the matter is the integral of the product of electron number $\rho(\boldsymbol{r})d\boldsymbol{r}$ in the differential volume $d\boldsymbol{r}$ and the factor of phase shift. The phase shift at $\boldsymbol{r}$ is $e^{-i\boldsymbol{q}\cdot\boldsymbol{r}}$, because the difference in the phase at $\boldsymbol{r}$ and at origin is $\boldsymbol{k_s}\cdot\boldsymbol{r} - \boldsymbol{k_i}\cdot\boldsymbol{r} = \boldsymbol{q}\cdot\boldsymbol{r}$, as illustrated in Figure 4.1.

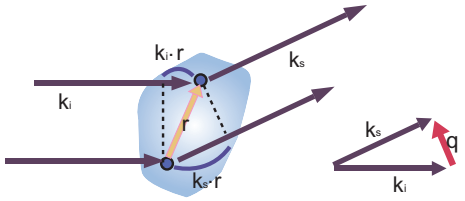

Figure 4.1: Difference of the phase

Total scattering is

$$A(\boldsymbol{q}) = \int_{matter} \rho(\boldsymbol{r}) e^{-i\boldsymbol{q}\cdot\boldsymbol{r}} d\boldsymbol{r} \tag{4.2}$$

Equation 4.2 indicates that the scattering amplitude is the Fourier transform of the electron density. If incident x-ray is horizontal wave, the scattering amplitude is

$$E_s = -r_e A(\boldsymbol{q}) \frac{e^{-i\boldsymbol{q}\cdot\boldsymbol{r}}}{r} \tag{4.3}$$

where r_e and r are Thomson scattering length and the camera distance. The intensity is the square of the amplitude

$$I_s = I_0 \frac{{r_e}^2}{r^2} |A(\boldsymbol{q})|^2 \tag{4.4}$$

It is noteworthy that we can write the dependence of scattering intensity on the wavelength and on the scattering angle by single parameter q. Normally, we observe the superposition of the scattering from horizontal wave and vertical wave because the light source is generally unpolarized. We have to take into account the polarization effect, because we observe only portion of the vertical wave which are vertical to the wavevector. Besides the correction of polarization, we normalize the scattering intensity in Equation 4.4 with respect to solid angle and incident intensity by multiplying r^2 and dividing by I_0. The normalized scattering intensity is called differential scattering cross section.

$$\frac{d\sigma}{d\Omega} = P{r_e}^2 |A(\boldsymbol{q})|^2 \tag{4.5}$$

where P is the polarization factor, defined by $P = (1 + \cos^2 2\theta)/2$. Thereafter, we refer $|A(\boldsymbol{q})|^2$ as to scattering intensity for brevity.

The scattering intensity $I(\boldsymbol{q})$ is uniquely determined by the electron density. However, we can obtain limited information of $I(\boldsymbol{q})$ by single measurement. It is because the scattering vector is confined within sphere surface, which is called Ewald sphere. We observe the cross-section of the Ewald sphere and the Fourier transform of electron density in reciprocal space. The curvature of Ewald sphere is usually approximated as planer in the case of SAXS.

We have to treat the scattering data remembering that the solid angle from each pixel of detector is different. As illustrated in Figure 4.2, pixel at wider scattering angle corresponds to smaller area of the Ewald sphere. The ratio of the projected areas of pixel A and pixel B is $(dt/dr)^2$, and $dt/dr = \cos 2\theta$. Therefore, detected scattering intensity of each pixel has to be divided by $\cos^2 2\theta$. This correction is useful when the datum from different camera length are connected for wider q-range information.

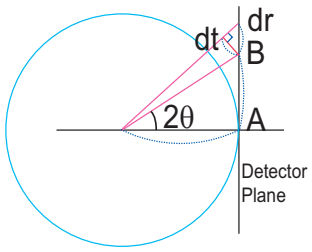

Figure 4.2: The solid angle of the pixel

4.1.2 Fourier transform and Patterson function

The scattering intensity $I(\boldsymbol{q})$ is solely determined by the electron density. In contrast, we cannot determine $\rho(\boldsymbol{r})$ by scattering intensity because the information as to the phase of scattering amplitude is lost in the intensity. Instead, we obtain auto-correlation function of electron density, sometimes referred to as Patterson function.

$$I(\boldsymbol{q}) = A(\boldsymbol{q})A^*(\boldsymbol{q}) = \int\int \rho(\boldsymbol{r_1})\rho(\boldsymbol{r_2})e^{-i\boldsymbol{q}\cdot(\boldsymbol{r_1}-\boldsymbol{r_2})} \tag{4.6}$$

Transformation by setting $\boldsymbol{r} = \boldsymbol{r_1} - \boldsymbol{r_2} = const$ gives

$$I(\boldsymbol{q}) = \int \tilde{\rho}^2(\boldsymbol{r})e^{-i\boldsymbol{q}\cdot\boldsymbol{r}}d\boldsymbol{r} \qquad \tilde{\rho}^2(\boldsymbol{r}) = \int \rho(\boldsymbol{r'})\rho(\boldsymbol{r'}+\boldsymbol{r})d\boldsymbol{r'} \tag{4.7}$$

We now rewrite auto-correlation function into more useful form. We set the averaged electron density as $\bar{\rho}$. We introduce new form of auto-correlation function

$$\tilde{\rho}^2_{new}(\boldsymbol{r}) = \int (\rho(\boldsymbol{r'}) - \bar{\rho})(\rho(\boldsymbol{r'}+\boldsymbol{r}) - \bar{\rho})d\boldsymbol{r'} \tag{4.8}$$

Using above Equation 4.8, the scattering intensity is

$$I(\boldsymbol{q}) = \int \tilde{\rho}^2_{new}(\boldsymbol{r}) e^{-i\boldsymbol{q}\cdot\boldsymbol{r}} d\boldsymbol{r} + V\bar{\rho}^2\delta(\boldsymbol{q}) \tag{4.9}$$

where V_{rad} is the irradiated volume. The term of delta function is not observable. This formula indicates that deviation of electron density from average value determines the scattering intensity. Thereafter, the auto correlation function of electron density is $\tilde{\rho}^2_{new}(\boldsymbol{r})$.

In the following, we further consider the case of isotropic system such as solution scattering. The average of the phase factor $e^{-i\boldsymbol{q}\cdot\boldsymbol{r}}$ with respect to solid angle is

$$\langle e^{-i\boldsymbol{q}\cdot\boldsymbol{r}} \rangle = \frac{\sin qr}{qr} \tag{4.10}$$

Therefore, Equation 4.7 can be simplified into

$$I(\boldsymbol{q}) = \int_0^\infty 4\pi r^2 \tilde{\rho}^2(\boldsymbol{r}) \frac{\sin qr}{qr}\, dr \tag{4.11}$$

The inverse Fourier transform is

$$\tilde{\rho}^2(\boldsymbol{r}) = \frac{1}{2\pi^2} \int_0^\infty q^2 I(q) \frac{\sin qr}{qr}\, dq \tag{4.12}$$

Therefore we reach the equation

$$\tilde{\rho}^2(0) = \frac{1}{2\pi^2} \int_0^\infty q^2 I(q) dq = V_{rad}(\overline{\Delta\rho})^2 \tag{4.13}$$

where $\overline{\Delta\rho}$ is the average of the deviation from the average electron density $\overline{\Delta\rho} = \overline{\rho - \bar{\rho}}$. This value $\tilde{\rho}^2(0)$ is called invariant Q because it is constant regardless of the movement or deformation of the system, unless it entails the change of electron density. In the case of biphase system, invariant is

$$Q \propto (\rho_1 - \rho_2)^2 \phi(1 - \phi) \tag{4.14}$$

where the volume fraction of one component is ϕ, and electron densitites of the two phase are ρ_1 and ρ_2.

4.1.3 Form factor and structure factor

Here we assume that the matter consists of identical particles or lattice. The electron density of j th particle is $\rho(\boldsymbol{r} - \boldsymbol{r_j})$. The electron density of the matter as a whole is $\sum_{j=1}^n \rho(\boldsymbol{r} - \boldsymbol{r_j})$. Then the scattering amplitude is

$$A(\boldsymbol{q}) = \sum_{j=1}^n \int \rho(\boldsymbol{r} - \boldsymbol{r_j}) e^{-i\boldsymbol{q}\boldsymbol{r}} d\boldsymbol{r} = \sum_{j=1}^n e^{-i\boldsymbol{q}\boldsymbol{r}_j} \int \rho(\boldsymbol{r'}) e^{-i\boldsymbol{q}\boldsymbol{r'}} d\boldsymbol{r'} \tag{4.15}$$

We can factorize the scattering amplitude into intraparticle term and interparticle term, which are sometimes referred to as form factor $F(\boldsymbol{q})$ and structure factor $S(\boldsymbol{q})$, respectively. The scattering intensity is $I(q) = |F(\boldsymbol{q})|^2 |S(\boldsymbol{q})|^2$.

We can have the similar equation as that of the auto-correlation function by transforming the structure factor.

$$
\begin{aligned}
|S(\boldsymbol{q})|^2 &= |\sum_{j=1}^{n} \exp(-i\boldsymbol{q}\cdot\boldsymbol{r_j})|^2 = \sum_{i=1}^{n}\sum_{j=1}^{n} \exp(-i\boldsymbol{q}\cdot(\boldsymbol{r_i}-\boldsymbol{r_j})) && (4.16)\\
&= n + \sum_{i\neq j} \exp(-i\boldsymbol{q}\cdot(\boldsymbol{r_i}-\boldsymbol{r_j})) && (4.17)\\
&= n\left(1 + \sum_{j=1}^{n} \exp(-i\boldsymbol{q}\cdot\boldsymbol{r_j})\right) = n\left(1 + \sum_{j=1}^{n} \frac{\sin(qr_j)}{qr_j}\right) && (4.18)
\end{aligned}
$$

The last transform is averaging about whole solid angle. We define the radial distribution function $g(r)$ as the number of particles per unit volume at the distance r from certain particle. The number of $4\pi r^2 g(r)$ particles are in the sphere shell whose radius is r and thickness is dr. Substituting the summation in Equation 4.18 to integral,

$$
\int_0^\infty 4\pi r^2 g(r)\frac{\sin(qr)}{qr}\,dr = \int_0^\infty 4\pi r^2 (g(r)-g_0)\frac{\sin(qr)}{qr}\,dr + \int_0^\infty 4\pi r^2 g_0 \frac{\sin(qr)}{qr}\,dr \tag{4.19}
$$

where the average particle density is g_0. The second term is unobservable as in the case of Equation 4.9. With Equation 4.18, we obtain

$$
|S(\boldsymbol{q})|^2 \propto 1 + \int_0^\infty 4\pi r^2 (g(r)-g_0)\frac{\sin(qr)}{qr}\,dr \tag{4.20}
$$

The fluctuation of the particle density determines the structure factor, as the deviation from average electron density determines the scattering intensity.

Summarizing above, the structure factor and the radial distribution function are connected by Fourier transformation.

4.1.4 Informations from SAXS

Guiner analysis

As explained above, the electron density cannot be directly reproduced from the scattering intensity. For example, the scattering pattern and auto-correlation function of oriental averaged sphere and those of cube are hard to distinguish. Therefore, we usually analyze the scattering intensity by assuming structural model. Without such models, however, we can extract useful information from $I(q)$, such as the ratio of surface to volume and approximate shape and radius of gyration of particles. Here the most popular analysis of SAXS, Guiner plot is introduced.

Guiner analysis is the measure to obtain radius of gyration of the particles, assuming that particles are identical and separate from each other so that the interference between them are negligible. The particle size is D, in other words,

$$\tilde{\rho}^2(\boldsymbol{r}) = 0 \qquad if: \ r > D \tag{4.21}$$

Using Equation 4.11 and Taylor expansion of sin qr,

$$I(q) = \int_0^D 4\pi r^2 \tilde{\rho}^2(\boldsymbol{r})\left(1 - \frac{q^2 r^2}{6}\right) dr = (\Delta\rho)^2 V_{par}^2 \left(1 - \frac{q^2}{6}\frac{\int_0^D 4\pi r^2 \tilde{\rho}^2(\boldsymbol{r}) r^2 \, dr}{\int_0^D 4\pi r^2 \tilde{\rho}^2(\boldsymbol{r}) \, dr}\right) \tag{4.22}$$

The radius of gyration is defined as follows;

$$\frac{\int_0^D 4\pi r^2 \tilde{\rho}^2(\boldsymbol{r}) r^2 dr}{\int_0^D 4\pi r^2 \tilde{\rho}^2(\boldsymbol{r}) dr} = 2R_g^2 \tag{4.23}$$

Finally, we obtain

$$I(q) = I(0)\left(1 - \frac{R_g^2 q^2}{3}\right) \approx I(0)\exp\left(-\frac{R_g^2 q^2}{3}\right) \tag{4.24}$$

Therefore, plotting log $I(q)$ against q^2 gives the radius of gyration. This approximation holds true under the condition $qR_g < 1$.

Debye-Bueche equation

Debye indicated that the auto-correlation function $\tilde{\rho}^2(\boldsymbol{r})$ of random biphase system is proportional to $e^{-r/a}$, where a is called correlation length. Approximation of random two phase can be applied to the crystal and amorphous biphase in polymer crystal, such as amorphous pockets existing among the bundles of lamellae (fibril). The scattering intensity is

$$I(q) \propto V_{rad}(\bar{\Delta\rho})^2 \int_0^\infty e^{-\frac{r}{a}} 4\pi r^2 \frac{\sin qr}{qr} \, dr \tag{4.25}$$

The result of the Fourier transform (Debye-Bueche equation) is

$$I(q) \propto \frac{a^3}{(1 + a^2 q^2)^2} \tag{4.26}$$

Small angle scattering of lamellar structure

Here, we discuss the SAXS analysis of lamellar structure, approximating lamellae is biphase structure composed of crystal and amorphous [2].

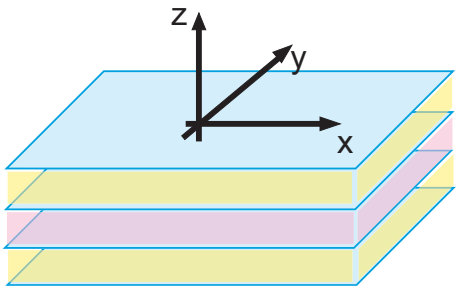

Figure 4.3: Lamellar coordinate. Pink and yellow correspond to crystal and amorphous

The electron density of lamellar structure (Refer Figure 4.3) is

$$\rho(x,y,z) = \Pi(x,L_x)\Pi(y,L_y)\rho(z) \tag{4.27}$$

where the definition of $\Pi(x,a)$ is

$$\Pi(x,a) = \begin{cases} 1 & (|x| < a/2) \\ 0 & (|x| \geq a/2) \end{cases} \tag{4.28}$$

The Fourier transform of $\rho(x,y,z)$ is

$$A(\boldsymbol{q}) = \int \Pi(x,L_x)e^{-iq_x x}dx \int \Pi(y,L_y)e^{-iq_y y}dy \int \rho(z)e^{-iq_z z}dz \tag{4.29}$$

With the formula of sinc function,

$$\int \Pi(x,L_x)e^{-iq_x x}dx = \int_{-\frac{L_x}{2}}^{\frac{L_x}{2}} e^{-iq_x x}dx = \frac{\sin(\frac{q_x L_x}{2})}{q_x} \tag{4.30}$$

We obtain

$$A(\boldsymbol{q}) = \frac{\sin(\frac{q_x L_x}{2})}{q_x}\frac{\sin(\frac{q_y L_y}{2})}{q_y} \int \rho(z)e^{-iq_z z}dz \tag{4.31}$$

If L_x, L_y are large enough, the term of sinc function can be approximated as delta function.

$$I(\boldsymbol{q}) = |A(\boldsymbol{q})|^2 = \delta(q_x)\delta(q_y) \int K(z)e^{-iq_z z}dz \tag{4.32}$$

where $K(z)$ is defined as the auto correlation function of the deviation of $\rho(z)$ from average value $K(z) = \int \rho(z'+z)\rho(z')dz'$.

We can calculate $K(z)$ from Fourier transform of the scattering pattern. The information of lamellar period and lamellar thickness can be extracted from $K(z)$.$K(z)$ is uniquely determined if the lamellar thickness d_c, lamellar period d_{ac}, and the difference of electron density between crystal and amorphous $\rho_c - \rho_a$ are given.

Before we calculate $K(z)$, we introduce the autocorrelation function of the deviation from amorphous region.

$$K_a(z) = \int (\rho(z'+z) - \rho_a)(\rho(z) - \rho_a)\, dz' \tag{4.33}$$

$K_a(z)$ is the overlapping area of the original image and ghost image, which moves z from the former.

$$K_a(z) = \begin{cases} (\rho_c - \rho_a)^2 (d_c - z)/d_{ac} & |z| < d_c \\ 0 & d_c < |z| < d_{ac} - d_c \end{cases} \tag{4.34}$$

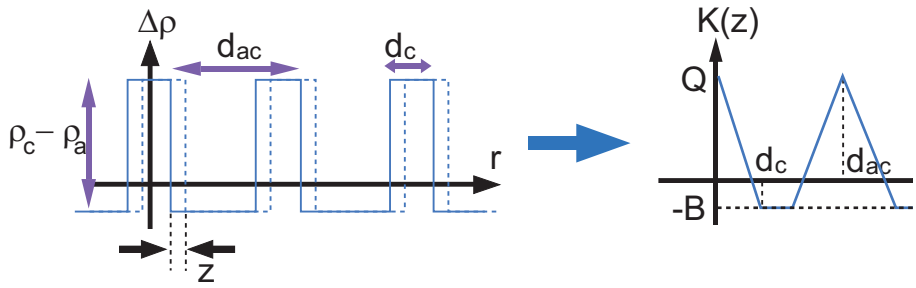

Figure 4.4: Calculation of auto-correlation function

We obtain $K(z)$ using the equation $K(z) = K_a(z) - (\langle\rho\rangle - \rho_a)^2$. the minima and second maxima of $K(z)$ corresponds to lamellar thickness and lamellar period, respectively. This analysis is useful if the crystallinity rate is below 0.3 or above 0.7, otherwise, we cannot obtain clear baseline.

4.1.5 Wide angle scattering from crystalline material

We can apply the concept of form factor and structure factor to the crystal. Form factor is the interference within unit cell, structure factor is the interference among unit cells. Typical example of structure factor is the Fourier transform of the grid $x = m_1 a, y = m_2 b, z = m_3 c$ $(m_1, m_2, m_3 :$ integer).

$$\rho_{lattice}(\boldsymbol{r}) = \sum_{m_1=-\infty}^{m_1=\infty} \delta(x - m_1 a) \sum_{m_2=-\infty}^{m_2=\infty} \delta(y - m_2 b) \sum_{m_3=-\infty}^{m_3=\infty} \delta(z - m_3 c) \tag{4.35}$$

Using the theorem of Fourier transform of inpulse train, we obtain the reciprocal lattice

$$S(\boldsymbol{q}) = \mathcal{F}(\rho(\boldsymbol{r})) \propto \sum_{m_1=-\infty}^{m_1=\infty} \delta\Big(q_x - \frac{2\pi}{a} m_1\Big) \sum_{m_2=-\infty}^{m_2=\infty} \delta\Big(q_y - \frac{2\pi}{b} m_2\Big) \sum_{m_3=-\infty}^{m_3=\infty} \delta\Big(q_z - \frac{2\pi}{c} m_3\Big) \tag{4.36}$$

In practical, the finite size of crystal gives broad peaks. The sharpness of peaks depends on the repetition number of the periods N, which is mathematically written by the Laue function

$$|S(\boldsymbol{q})|^2 = \frac{\sin^2\left(\frac{N}{2}\boldsymbol{q}\cdot\boldsymbol{a}\right)}{\sin^2\left(\frac{1}{2}\boldsymbol{q}\cdot\boldsymbol{a}\right)} \tag{4.37}$$

where $\boldsymbol{a}$ is the lattice vector. Full width at half maximum of the peak and the maximum value of this function are proportional to $1/N$ and N^2, respectively. Assuming the constant periodicity, we can estimate the crystal size from Δq.

In reality, the polymer crystal is not ordered completely. The disorder is classified into two groups [63]. The disorder of first kind describes the lattice where the average position of lattice coincides with the ideal position, and long range order is maintained. Therefore, the FWHM of the diffraction peak is constant at higher order peaks. This disorder corresponds to thermal vibration or the conformation deviation around the chain axis. The disorder of second kind is the disarray where the systematic displacements exist among neighboring lattice points, and the long range order is lost. This leads to the broadening of the higher order peaks.

4.1.6 Lorentz correction

Assuming the random orientation of lamellae in the irradiated area, the reciprocal spots of the lamellae with the same period are distributed on the sphere shell (Thereafter we call it reciprocal lattice sphere). Only the reflection from lamellae which satisfy Bragg condition is observable. As illustrated in Figure 4.5(Left), at smaller angle, the region where the reciprocal lattice sphere cross the Ewald sphere are larger with respect to solid angle. Without correction, this leads to the overestimation of the scattering intensity at smaller angle region. This problem is avoidable by multiplying $4\pi q^2$ to raw data at scattering vector q. The correction is called Lorentz correction [68][69].

This correction must be applied to the small angle scattering. Let us compare the case of wide angle scattering where the curvature of Ewald sphere is not negligible. As shown in Figure 4.5(Right), the thickness of the cross section of reciprocal lattice sphere at the diffraction angle 2θ is thicker by the factor $1/\cos\theta$. Therefore, we have to multiply $\cos\theta$ and q^2 to differential scattering cross section $I(q)$ to integrate the reciprocal spots in whole reciprocal space.

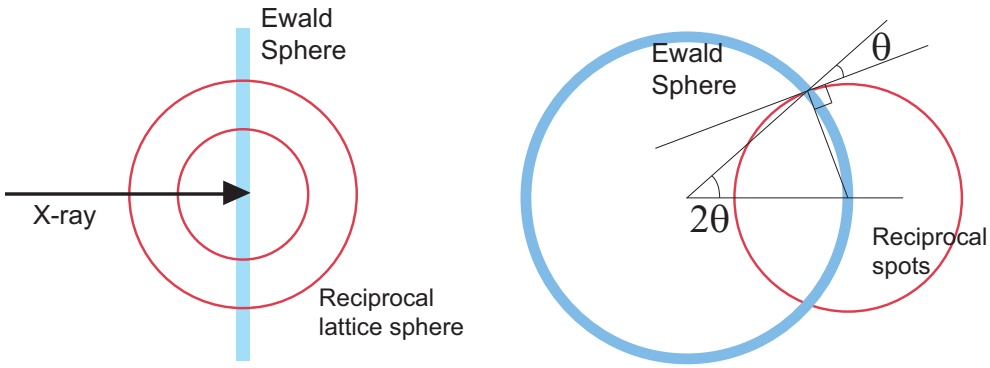

Figure 4.5: Left: Lorentz correction of SAXS. Right: Lorentz correction of WAXS.

Fundamentally, Lorentz correction is applicable provided that the crystal is randomly oriented and the scattering pattern is isotropic. However, it is sometimes mistakenly applied to anisotropic patterns as shown in Figure 4.6.

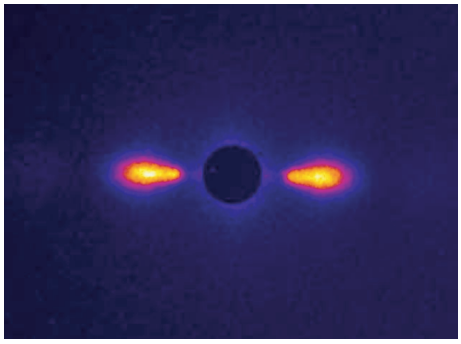

Figure 4.6: Anisotropic scattering pattern of PCL lamellar structure

When dealing with anisotropic scattering pattern from lamellae, further consideration is needed. We have to take into account that the distribution of reciprocal spots is cylindrically symmetrical. In this case, the raw data have to be multiplied by $2\pi q \sin\alpha$ where α is the angle between spherulite radial direction and the scattering vector, because the twist angle which corresponds to the cross-section of Ewald sphere is different depending on α even at the same q region [66]. After that, the data is integrated azimuthally.

4.2 Polarized optical microscopy

Porlarization state changes through anisotropic crystalline material such as polymer crystal, where long chain molecules are arranged in certain direction [56]. It is because the electric potentials of vertical and horizontal direction are different. Therefore, when we place spherulite between mutually orthogonal polarizer and analyzer, the transmittance varies depending on the phase of lamellar twist. In this section, we prepare the fundamentals for analyzing method of lamellar twist by polarized optical microscopy (POM).

4.2.1 Ellipsoidal optical indicatrix

In optically isotropic system, dielectric flux density $\boldsymbol{D}$ is proportional to electric field vector $\boldsymbol{E}$; $\boldsymbol{D} = \varepsilon \boldsymbol{E}$. In anisotropic system, they are connected by symmetrical tensor $\boldsymbol{\varepsilon}$, which is diagonalized by setting proper coordinates [57].

$$\boldsymbol{D} = \boldsymbol{\varepsilon} \boldsymbol{E} \tag{4.38}$$

Such coordinates is referred to as optical elastic axes. In the case where three axes of crystal unit cell are orthogonally crossed, the optical elastic axes coincide with the unit cell axes. Anisotropic numerical index is described by ellipsoidal optical indicatrix in xyz space. First, we calculate the numerical index of horizontal wave and vertical wave. We start from Maxwell equations as follows.

$$\nabla \times \boldsymbol{E} = -\frac{\partial \boldsymbol{B}}{\partial t} \tag{4.39}$$

$$\nabla \times \boldsymbol{H} = \frac{\partial \boldsymbol{D}}{\partial t} \tag{4.40}$$

We can rewrite them for travelling wave $\exp(i(\omega t - \boldsymbol{k} \cdot \boldsymbol{r}))$

$$\boldsymbol{k} \times \boldsymbol{E} = \omega \mu_0 \boldsymbol{H} \tag{4.41}$$

$$\boldsymbol{k} \times \boldsymbol{H} = -\omega \boldsymbol{D} \tag{4.42}$$

With Equation 4.40, we obtain

$$\boldsymbol{k} \times (\boldsymbol{k} \times \boldsymbol{E}) + \omega^2 \mu_0 \boldsymbol{\varepsilon} \boldsymbol{E} = 0 \tag{4.43}$$

From Equation 4.42, $\boldsymbol{D}$ is on the plane perpendicular to $\boldsymbol{k}$, hence, the normal vibration mode of $\boldsymbol{D}$ is to be analyzed. Using $\boldsymbol{E} = \boldsymbol{\varepsilon}^{-1} \boldsymbol{D}$, $\boldsymbol{\eta} = \varepsilon_0 \boldsymbol{\varepsilon}^{-1}$, $\boldsymbol{k} = k\boldsymbol{u}$, $n = k/k_0$, $k_0^2 = \omega^2 \mu_0 \epsilon_0$, Equation 4.43 can be transformed into

$$-\boldsymbol{u} \times (\boldsymbol{u} \times \boldsymbol{\eta} \boldsymbol{D}) = 1/n^2 \boldsymbol{D} \tag{4.44}$$

Left hand is equivalent to the projection of $\boldsymbol{\eta D}$ onto the plane perpendicular to $\boldsymbol{u}$. Now we set the indices of a, b, c axis are n_a, n_b, n_c and the reciprocal of them are N_a, N_b, N_c. When we define $\boldsymbol{u} = (\sin\theta\cos\phi,\ \sin\theta\sin\phi,\ \cos\theta)$ and $t = 1/n$, Equation 4.44 leads to the quadratic equation

$$\begin{aligned} t^2 - t\Big(N_a(\cos^2\theta + \sin^2\theta\sin^2\phi) + N_b(\cos^2\theta + \sin^2\theta\cos^2\phi) + N_c\sin^2\theta\Big) \\ + N_a N_b \cos^2\theta + N_b N_c \sin^2\theta\cos^2\phi + N_a N_c \sin^2\theta\sin^2\phi = 0 \end{aligned} \tag{4.45}$$

Let us show the examples of solutions:

$$t = N_0, t = N_0\cos^2\theta + N_c\sin^2\theta \qquad if:\ \ N_a = N_b = N_0 \tag{4.46}$$

$$t = N_b, t = N_a\cos^2\theta + N_c\sin^2\theta \qquad if:\ \ \phi = 0 \tag{4.47}$$

4.2.2 Polarized optical microscopy

Here, qualitative understanding of the principle of POM is described. We assume the numerical index of *a* axis and that of *b* axis are identical, which approximately holds true for most of the polymer crystals. Samples are placed between orthogonally crossed polarizer and analyzer. Light is detected only when the polarization state changes through the sample. If anisotropic axis is parallel with analyzer or polarizer, the polarization remains the same. This is why the Maltese cross pattern is observed. Polarization state also does not change if the wave vector is within *ab*-plane, which corresponds to the extinction bandings of spherulite.

The orientation of index ellipsoid is illustrated in Figure 4.7. POM is appreciated as a powerful tool to investigate molecular orientation not only of polymer crystal, but also of emulsion and crystalline liquid.

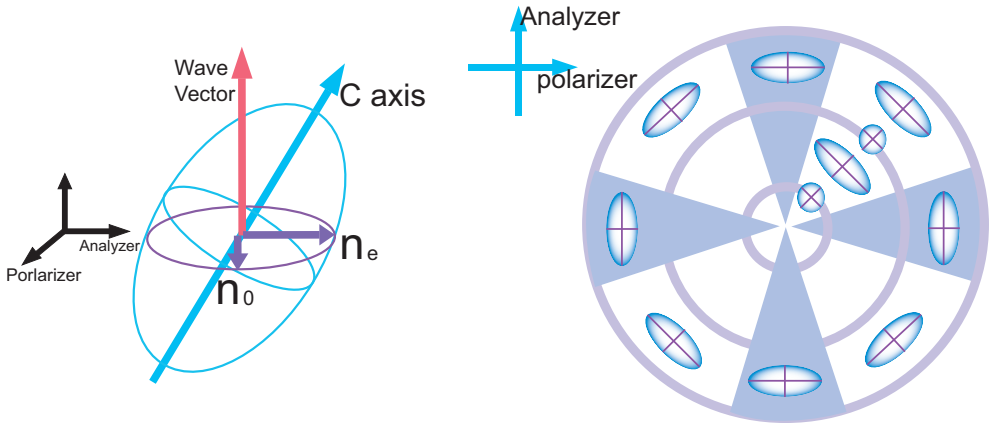

Figure 4.7: Index ellipsoid and its orientation within spherulite

Chapter 5

Synchrotron radiation and related instrumentation

Synchrotron x-ray is widely used for structure analysis. When an electron travelling at nearly the light speed changes its direction in the magnetic field, the electromagnetic wave is radiated along the tangential of the electron orbit. This radiation is called synchrotron radiation after the fact that it was first observed in the synchrotron accelerator. The features of synchrotron radiation are as follows [71]. It is the necessities for the small angle x-ray scattering where the scattering is weak and sometimes no peak involved. It is also essential for the microbeam x-ray scattering which needs low divergent light source. The low divergence also has the advantage in that loss of the photon flux by the reflection at the monochrometer is relatively small. In this chapter, the principle of the generation of synchrotron radiation is summarized.

- Brilliance of the 10^3-10^6 times larger than the laboratory light source.
- Extremely low divergent (the order of mrad).
- Wide range spectra ranging from x-ray to infrared ray.
- Horizontally polarized light

In addition to the advent of synchrotron radiation, recent development of insertion light source, which is the feature of the third synchrotron facilities, further encouraged the microbeam scattering measurement. The insertion light source and the process of making microbeam are also described. When we conduct experiments at beamlines of synchrotron facilities, we have to optimize the setup and detecting systems for individual purposes. Characteristics of beamline and detecting system are summarized.

5.1 The principle of the generation of synchrotron radiation

When an electron is moving at nearly the light speed, the ratio of its velocity to the light speed is expressed as

$$\beta = \frac{v}{c} = \sqrt{1 - \frac{1}{\gamma^2}} \tag{5.1}$$

where gamma is the ratio of its energy the static mass energy, $\gamma = E_e/m_e c^2$.

First, we consider the divergence of the synchrotron radiation. If the electron velocity is much less than the light speed, electron dipole radiation is generated. By contrast, if the velocity approaches the light speed, the relativity effect is pronounced and the dipole radiation is Lorentz transformed and distorted as illustrated in Figure 5.2.

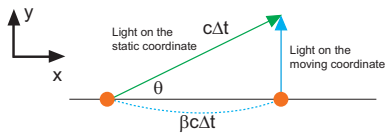

Figure 5.1: Light pass on static coordinate and electron coordinate

Here we define the time in electron coordinate τ and the time in the stationary observers' coordinate t. We assume the situation where light is radiated at $\tau = t = 0$ toward right angle in electron coordinate. In the static coordinate, the electron travels $\beta c\Delta t$ in x direction at $t = \Delta t$. In the electron coordinate, it advances $c\Delta\tau$ in y direction. The light is observed to proceed $c\Delta t$ in the direction θ as shown in Figure 5.1 in static coordinate. Therefore, the right angle in the electron coordinate corresponds to θ in static coordinate.

$$\cos\theta = \frac{\beta c\Delta t}{c\Delta t} \tag{5.2}$$

With Taylor expansion, we obtain

$$1 - \frac{\theta^2}{2} = 1 - \frac{1}{2\gamma^2} \tag{5.3}$$

Therefore, we obtain $\theta = 1/\gamma$. The knot in the right angle of the static dipole corresponds to the angle $1/\gamma$ of the dipole of the radiation. When $E = 2.5$ GeV, we can obtain $1/\gamma = 0.2$ mrad.

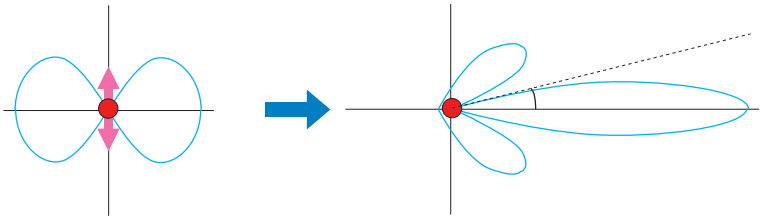

Figure 5.2: Dipole radiation seen from static coordinate. Left: $v << c$, Right : $v \approx c$

Next, the spectrum distribution is considered. In the non relativistic case, the circular frequency of the radiation is the same as that of electron rotation $\omega_0 = v/R$. If $c \approx v$, the radiation from the arc with central angle $d\theta = 2/\gamma$ is observable because the divergence of radiation is $2/\gamma$.

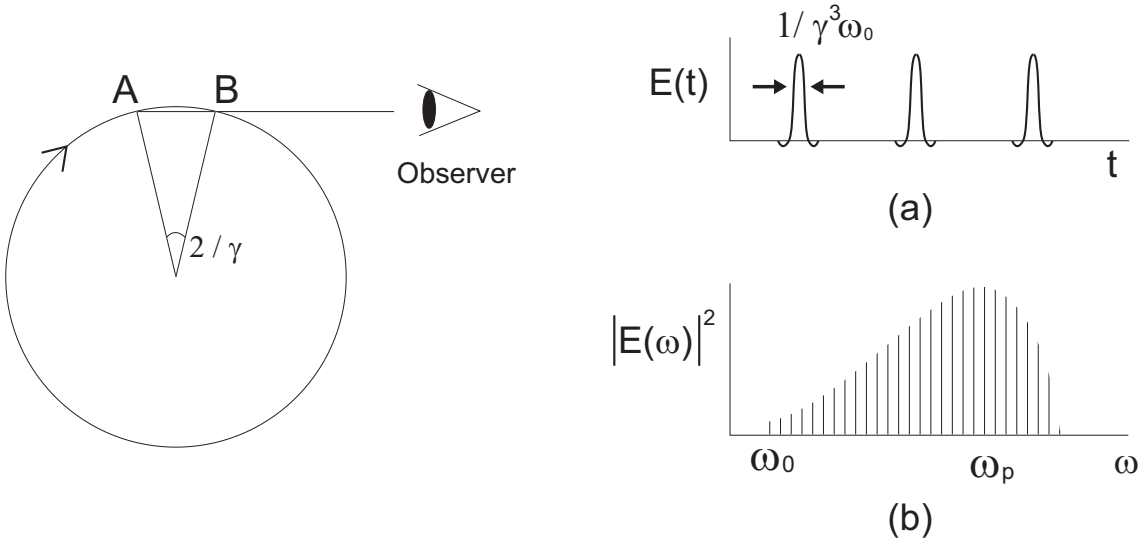

Figure 5.3: Left: The x-ray emitted from the arc AB is observable. Right: the electric field at the observer (a) and its power spectrum (b)

The period during which the observer detects the radiation is the time electron takes in travelling the arc minus the time light takes in passing the chord.

$$\Delta t = \frac{2R}{v\gamma} - \frac{R}{c}\sin\frac{2}{\gamma} \approx \frac{R}{c\gamma^3} \approx \frac{1}{\gamma^3\omega_0} \tag{5.4}$$

Therefore, the electric field $E(t)$ consists of the periodic pulses, whose interval is ω_0 , and period is $1 \,/\, \gamma^3\omega_0$. Its power spectrum is the squared absolute value of the Fourier transform of the electricfield, $|E(\omega)|^2$, which reaches its maxima at

$$\omega_p \approx \frac{2\pi}{\Delta t} = 2\pi\gamma^3\omega_0 \tag{5.5}$$

5.2 Insertion light source

Radiation generates when the electron orbit is bent as explained above. The insertion light source is placed in the linear section of the electron orbit. It changes the magnetic field periodically, so that the electron wriggles to amplify the radiation. The magnetic field is along z-direction, and the electron moves in the xy plane.

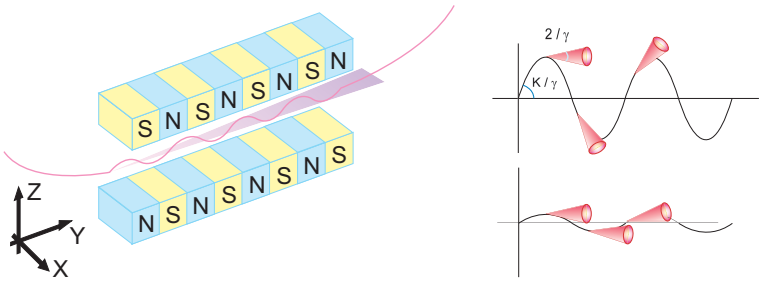

Figure 5.4: Left: Schematic view of insertion light source. Right: Difference of wiggler ($K >> 1$) and undulator ($K < 1$).

Here parameter K is introduced to characterize insertion devices.

$$K = \frac{eB_u\lambda_u}{2\pi m_e c} \tag{5.6}$$

where e: electron charge, B_u: amplitude of the magnetic field, λ_u: the period of the magnetic field, m_e: static mass of the electron, c: light speed. Using K parameter, the maximum gradient of the sine curved electron orbit is K/γ. Comparing with the divergence of the radiation $2/\gamma$, the characteristic of the radiation is different depending on the value of K. When $K >> 1$, the radiation only from the orbital apices is observed. When the number of the magnetic period is N, the sum of the intensity is superposition of the radiation from the each apices, and the intensity increases by N times. This kind of insertion device is called wiggler. In the case where $K < 1$, all the radiation is observed and it interferes internally, hence the amplitude and the intensity increases by N times and N^2 fold, respectively. Moreover, the quasi-monochromatic light is achieved.

In the following, the dependence of the wavelength on the K parameter is described. The electron starting at $y = 0$ wriggles in the undulator, and reaches $y = \lambda_u$. The amplitude is $K\lambda_u/\gamma 2\pi$. The pass length is

$$\ell = \int_0^{\lambda_u} \sqrt{1 + \left(\frac{K\lambda_u}{\gamma 2\pi}\sin\left(\frac{2\pi}{\lambda_u}y\right)\right)^2}\, dy \approx \lambda_u\left(1 + \frac{K^2}{4\gamma^2}\right) \tag{5.7}$$

When the electron moves ℓ at the speed βc, the light reaches at $y = \frac{\ell}{\beta c}c = \frac{\ell}{\beta}$. Therefore, the wavelength from the undulator is

$$\lambda = \frac{\ell}{\beta} - \lambda_u = \frac{\lambda_u}{2\gamma^2}\left(1 + \frac{K^2}{2}\right) \tag{5.8}$$

This indicates that longer wavelength is achieved when the magnetic field increases. The monochromaticity is proportional to the number of the magnetic period. $\Delta\lambda/\lambda = 1/N$. In this regard, higher harmonic wave cannot be ignored in the case where $K \approx 1$.

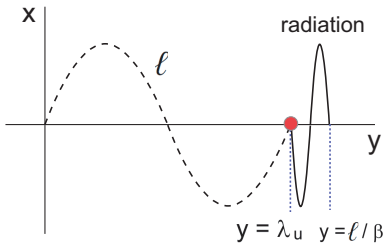

Figure 5.5: Wavelength of the radiation from undulator.

5.3 Characteristics of beamlines

When we choose beamline and optimize optical systems for experiments, following characteristics are taken into account, such as small angle resolution, camera length, energy resolution, and coherence.

Small angle resolution and camera length

The concept of small angle resolution is explained here, taking three slits system as an example, which is the standard arrangement for beam shaping [74]. This value determines upper limit of the observable scale. It is critical for small angle scattering. Here we define the distance ℓ_0, ℓ_1, ℓ_2, ℓ_3, ℓ_4 as illustrated in Figure 5.6. The aperture of the three slits are S_1, S_2, S_3.

First and second slit determines the beam divergence and brilliance. The eyesight size from the second slit through the first focus is called effective focus size f_{eff}. $f_{eff} = S_1(\ell_0 + \ell_1)/\ell_1 + S_2\ell_0/\ell_1$. f_{eff} needs to be set smaller than the light source. The beam divergence is $\omega = (S_1 + S_2)/\ell_1$.

After the first slit and second slit are set, the third slit is placed at the downstream to eliminate the parasitic scattering from them. Using the relation $\triangle ABC \backsim \triangle ADE \backsim \triangle AFG$, the beam size at the third slit is $FG = \ell_2 S_2/\ell_1 + (\ell_1 + \ell_2)S_2/\ell_1$. The aperture of the third slit is adjusted not to interfere the direct beam.

It is noteworthy that there is smeared region $2b$ around direct beam $2a$, where eliminating the parasitic scattering is principally impossible (Figure 5.6). Therefore, the small angle resolution is determined by the region completely free from parasitic scattering. Using the relation such as $\triangle A'DE \backsim \triangle AFG \backsim \triangle AHI$, we obtain $b = S_2\ell_3/\ell_2 + S_3(\ell_2 + \ell_3)/\ell_2$. The small angle resolution is

$$2\theta_{min} = \tan^{-1}(b/\ell_4) \tag{5.9}$$

Better small angle resolution is not necessarily achieved by the longer camera length. Longer camera length increases the angular resolution. The camera length has to be optimized based on these points.

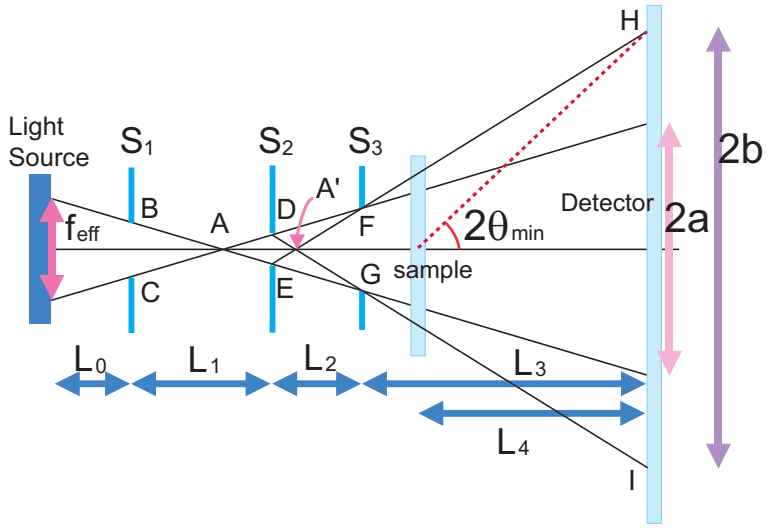

Figure 5.6: Arrangement of three slits and the small angle resolution

Energy resolution

Energy resolution, in other word, monochromaticity is defined as $\Delta\lambda/\lambda = \Delta E/E$. Combined with the differential Bragg formula, the dependence of the energy resolution on the diffraction angle can be obtained.

$$\frac{\Delta\lambda}{\lambda} = \frac{\Delta\theta}{\tan\theta_B} \tag{5.10}$$

According to this formula, angular resolution is sensitive to the monochromaticity at wider scattering angle. It can be improved by shorter wavelength.

Emittance

In microbeam x-ray scattering experiments, beam divergence is very important parameter, because it affects the angular resolution of the diffraction, particularly in the small angle region. This is ascribable to the Liouville's theorem that the product of beam size and divergence is constant under the same brilliance. Before the introduction of the theorem, concept of phase space is summarized [79].

When the photon is moving in the zx plane as illustrated in Figure 5.7, movement of the photon at z_0 is described by its position x_0 and its moving direction $x'_0 = dx/dz|_{x=x_0}$. The horizontal axis and vertical axis of phase space is its position and direction.

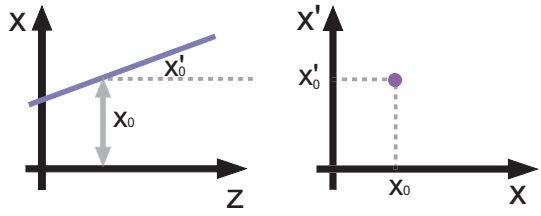

Figure 5.7: Real space and Phase space

Let us plot group of photons in the phase space, as illustrated in Figure 5.8. Divergent beam is (a), and convergent beam is (b). Arranging the beam shape by a slit corresponds to cutting out the clouds of photons is illustrated in (c).

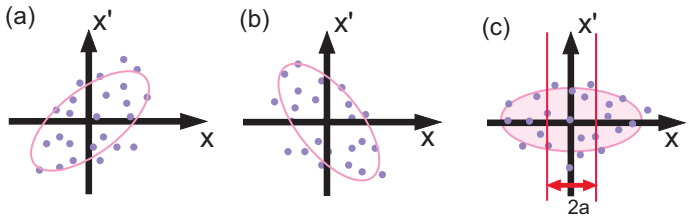

Figure 5.8: Cloud of photons in phase space. (a) Divergent beam. (b) Convergent beam. (c) Shaping of the beam by silts.

Emittance is defined as the ellipsoidal area of the phase space, which is the product $W = \sigma_x \sigma'_x$, where the variance of beam size and the direction are σ_x、 σ'_x respectively. According to Liouville's theorem, it remains constant unless the beam size is not arranged by slits, which indicates that the light source with low emittance is requisite for microbeam experiments. The emittance of synchrotron radiation is the sum of the emittance of electron orbit W_e and that of photon W_p. W_p is constant and beamline is designed to minimize W_e. Normally, W_e is around 10 nm rad – 100 nm rad, and the vertical emittance is a few percent of the horizontal.

5.4 Microbeam x-ray scattering

5.4.1 Application of microbeam x-ray scattering

Synchrotron radiation with high brilliance enabled time-resolved measurement and space-resolved measurement, both of which resulted in broadening the variety of the x-ray application. Microbeam x-ray scattering measurement is suitable for the structural analysis of soft materials which sometimes have an inhomogeneity of micrometer order.

The application of the microbeam scattering is classified into the two groups [5]. One is the scanning measurement of the sample, which has inhomogeneity of the μm order. The other is local time-resolved measurement with fixed beam position. The example

of the former application is the analysis of the twisting lamellar in the spherulite in this work, and mutually penetrated spherulites of crystalline/crystalline polymer blend, and the spatial distribution of the filament protein in the hair. The examples of the latter are crystallization process of the alkane in single emulsion, and the transition of the lamellar orientation of Polypropylene during elongation.

5.4.2 Optics for microbeam x-ray scattering

There are some ways to prepare microbeam, for example, pinhole, mirrors, and zone plate [77].

Figure 5.9: Optics for microbeam.

Owing to the low divergence of the synchrotron radiation, microbeam can be obtained by pinhole or by slit systems. However, the flux is reduced drastically and not suitable for the scattering measurement. BL40XU at SPring-8 with the helical undulator is the exception, because monochromaticity without double crystal monochrometer is achieved, hence the flux is incomparably high.

Light condensing device like lens of the visible light is not practically available in the x-ray region, because the refractive index of the x-ray is nearly equal to unity. Recent development of the fine processing technology enables the focusing mirror and the focusing device making use of the x-ray diffraction.

Typical example of the reflecting mirror is Kirpatrik Baez mirror [73]. The critical angle of the total reflection of the x-ray is $\theta_c = \sqrt{2\delta}$, where x-ray refractive index is $n = 1 - \delta$. X-ray is incident upon the mirror in minute angle, and the two mirrors are placed to focus the incident beam horizontally and vertically. It is suitable for x-ray absorption fine structure (XAFS) measurement, where the energy of x-ray is adjusted. It is because the reflection angle is constant regardless of the energy of incident beam.

Another type of x-ray condensing device is Fresnel zone plate (FZP). It is composed of concentric rings where obscure to x-ray region and transmissive to x-ray region are alternatively arranged. The period between each zone is designed so that every light from transmissive region are coherently superimposed. When the incident x-ray are focused to the point F in Figure 5.10, we obtain following expression

$$\sqrt{f^2 + r_n^2} = f + \frac{n\lambda}{2} \tag{5.11}$$

where r_n is the distance from the center of zone plate, and f is the focal distance, λ is wavelength. Approximation $(n\lambda/2)^2 << f$ leads to

$$r_n^2 = nf\lambda \tag{5.12}$$

The advantage of FZP compared with the KB mirror is that it is relatively indifferent to the coma aberration problem. The disadvantage is that it is not suitable for the experiments where λ changes, and that monochromatic light source is requisite. From Equation 5.12, the focal distance is dependent on λ.

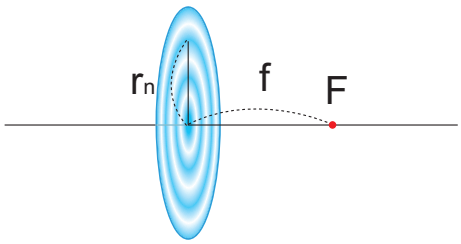

Figure 5.10: Fresnel zone plate.

5.5 X-ray detecting system

5.5.1 Characteristics of x-ray detector

X-ray detectors have to be appropriately chosen for individual purposes. For example, if weak signals from solution scattering have to be detected in wide q range, sensitive and non-distortive detector is suitable. Here, specific features of the x-ray detectors are explained [72].

- Sensitivity

In the case of photon-counting detector, the definition of sensitivity is

$$\eta = \frac{\text{Counted photons}}{\text{Incident photons}} \tag{5.13}$$

And it is determined by its absorptiveness. In the case of integral detector, the sensitivity is written by the signal to noise ratio of the output and that of the input.

$$DQE = \frac{(\text{mean output signal})/(\text{fluctuation of output})}{(\text{mean input signal})/(\text{fluctuation of input})} \tag{5.14}$$

Assuming Poisson distribution of incident photons, $DQE = n/N$ where n and N are the number of incident photons and counted photons, respectively.

- Dynamic Range

The dynamic range is the region where the linearity between input and output is maintained. The data in the non-linear range have to be corrected. The dynamic range is in the relation with DQE such that improving DQE by augmenting the signal per photon leads to the reduction of the dynamic range.

- Time resolution

Time resolution is the number of the read out frames per unit time. Film detector is inferior in this point, for the read out time is relatively longer. If phosphor is contained in the detector, the afterglow has to be paid attention. Normally, the half decay time of phosphor is in the order of 10 ms.

- Spatial resolution

Spatial resolution is defined by the signal spread from the point light source. Point spread function (PSF) is defined by the response of the infinitesimal beam. The output signal is written by $h(x, y) * \mathrm{PSF(x, y)}$ when the intensity distribution of the input is $h(x, y)$. The FWHM of PSF(x, y) is the indicator of the spatial resolution. In this context, line spread function (LSF) is one of the commonly used indicators of spatial resolution, which is defined by the integral of PSF in certain direction. LSF can be measured by moving knife-edge in front of the uniform light source.

5.5.2 Types of x-ray detectors

X-ray detectors are grouped into pulse counting type and integral type. Salient features of pulse counting detector are noiseless and useful for weak signal because it senses the photon one by one. The disadvantage is that there is a non-sensitive period after the counting, which leads to miss-counting. It is, therefore, not suitable for the intense signals. Integral type detectors accumulate electrical signals and detect them collectively. It is necessary for highly brilliant synchrotron radiation facilities, because the miss-counting does not matter. By contrast, it is not appropriate for the weak signal measurement, because of the dark-noise arising from read-out noise.

X-ray detectors can be classified in another way into those which directly transform the x-ray photon into electrical signal and those which intermediate fluorescence emitted from x-ray phosphor. The direct type features the high position resolution, but the dynamic range is narrow. The indirect type has advantage of dynamic range, large acceptance surface. The disadvantage is the problems of non-uniform sensitivity and image distortion.

Typical examples of the classifications above are summarized in the table below.

	Pulse counting	Integral
Direct type	PILATUS	Flat panel
Indirect type	Scintillation counter	Image plate, I.I.+CCD

5.5.3 Image intensifier + charge coupled device detector

The signals of x-ray photon are detected by charge coupled device (CCD) camera through the process as follows [75] (Figure 5.11 Left);

1. Transformation of transmissive x-ray into manageable visible photons and electrons by x-ray phosphor.
2. Image intensification
3. Dismagnification at lens system
4. Transformation from visible photons into electrons
5. Data transfer

X-ray phosphors of image intensifier (I.I.) stop the highly transmissive x-ray, and change it into visible light. CCD itself has sensitivity for x-ray. However, direct x-ray into CCD is impractical because it narrows dynamic range. It is because x-ray generates thousands of electron-hole pairs per single x-ray photon and the charge capacity of each pixel is limited (up to 1 million electrons). High DQE is achieved because hundreds of photons are generated per x-ray photon in the phosphor. CsI and NaI are very energy efficient phosphors. They are hydroscopic and readily poisoned by humidity, which necessitates hermetic sealing. Beryllium is used as the sealing material because it is x-ray transparent and impervious to water vapor. There are various morphology of phosphor crystals; powder, single crystal, and columns (Figure 5.11 Right), which affects the spatial resolution of detector. For example, florescence transmits with the minimum lateral diffusion through the column shaped phosphors. It is designed to have enough thickness for sufficient number of visible photons. The phosphor has to be appropriately chosen so that the wavelength of output signal matches the sensitivity of CCD.

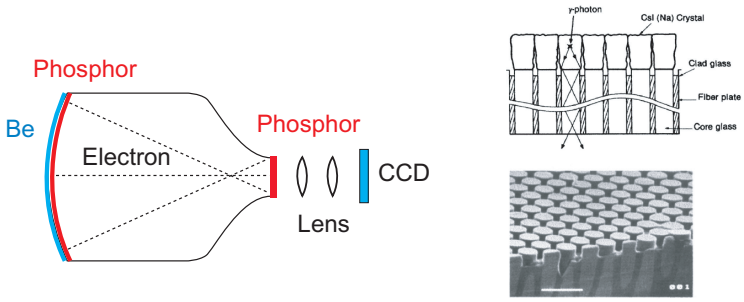

Figure 5.11: Left: Schematic view of I.I. + CCD detector. Right: Columnar crystal of phosphor.

In the image intensifier, the photoelectrons generated by bialkali of photoelectron cathode are accelerated in the electric field. Then the electron is stopped by the termi-

nal phosphor and converted into visible photon again. The number of photon is multiplied in this process. In addition, electrostatic I.I. reduces the image size for CCD, which necessitates the curvature of photoelectroncathode.

The visible photons thorough the lens system are detected at CCD. The devices are arrayed horizontally and vertically. CCD turns visible photons into electrical signals by photoelectric effect, where the gap between valence band and conductance band are at play. The electrons are accumulated in the potential well, where about 10 voltage is applied between silicon substrate and insulating film of SiO_2. The electrons are transferred by the cooperative works of neighboring devices.

There are two types of CCD; frame transfer type and interline transfer type. Frame-transfer CCD is composed of the photoactive region and electron-charging region. The yielded photons are transferred to charging region by the transparent electrode on the photoactive region. Electron transfer is suspended during exposure, and then they are transferred while the mechanical shutter is closed. Therefore, inactive time exists in frame transfer type. By contrast, non sensitive time does not exist in interline transfer CCD, where the photoactive region of photodiode and transfer region of vertical CCDs are separate. Exposure and readout are simultaneously conducted. It is suitable for time-resolved measurement. On the other hand, the capacity of the electron well is inferior to the frame transfer type. Thus, frame transfer type is appropriate for the measurement of weak signals.

Finally the problems of image distortion and uniformity of sensitivity are briefly summarized. The distortion of the image is ascribable to the bent photoelectron cathode and the distortion from the lens optics. The distortion and uneven thickness of phosphor and beryllium window lead to non-uniform sensitivity. The distortion is estimated by placing grid mask just upstream of the I.I. and measuring the scatter pattern of glassy carbon. The correction method for image distortion is proposed [76]. It is desirable to set the incident beam at the center of I.I. to minimize the distortion problem.

Chapter 6

Experiment

6.1 Sample preparation

In our research, two kinds of polymers (PCL/PVB or PVDF/PEA) were blended by dissolving into the mutual solvent. We used tetrahydrofuran for PCL/PVB blend and dimethyl fluoride for PVDF/PEA blend. After the solvent was evaporated, a piece of sample was cut out from the film and placed on mica substrate. The sample was heated above melting point for 10 minutes, and then applied onto the substrate so that the sample thickness was about $20 - 30$ μm. Finally, the sample was quenched to isothermal crystallization temperature (Figure 6.1 and Figure 6.2).

We also prepared the spherulites grown in three dimensional space. After the sample was completely crystallized, it was cut to 50 μm thick with a microtome. To prevent the artifact from friction, the sample and knife were immersed in liquid nitrogen just before the cutting work. Samples which contains spherulite center was selected (Figure 6.3).

6.2 Microbeam WAXS measurement

Microbeam WAXS measurement was performed at BL-4A, photon factory [78]. BL-4A is designed for x-ray microbeam measurement equipped with Kirkpatrik-Baez (KB) mirror system. State analysis by X-ray absorption fine structure (XAFS) and microbeam scattering measurement are conducted. After the synchrotron radiation from storage ring was made monochromatic by double-crystal monochromator or multi-layer monochromater, the x-ray is focused to 5 μm by KB mirror. The facets of double crystal monochromator is (111) of Silicon, and the energy resolution is about $\Delta E/E = 10^{-4}$. Because of the narrow width of diffraction angle, monochromaticity of double crystal type is higher than multi-layer type by three orders of magnitude, whereas the intensity is inferior by two order of magnitude. Normally, double crystal type is chosen for XAFS measurement where the energy resolution is a severe constraint. We chose multi-layer type for shorter exposure time.

The setup for our research is schematically shown in Figure 6.4. The beam size at the

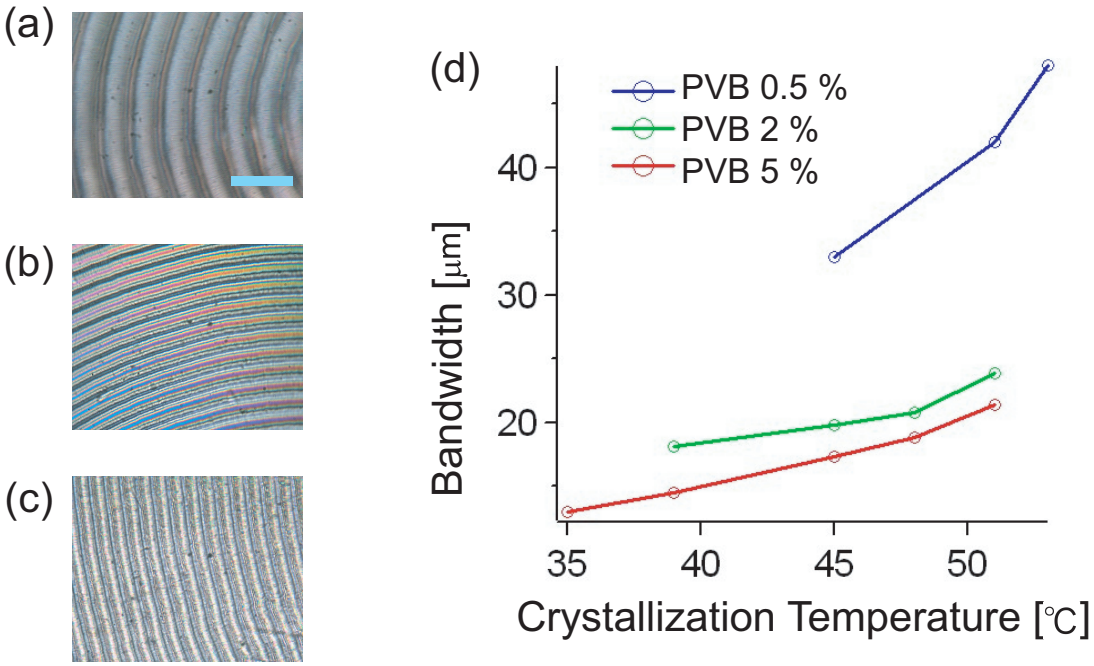

Figure 6.1: (a) PCL/PVB = 99.5/0.5, Tc = 45 ℃. (b) PCL/PVB = 98/2, Tc = 45 ℃. (c) PCL/PVB = 95/5,Tc = 45 ℃. (d) Bandwidth of the spherulite under various conditions. Scale bar: 50 μm.

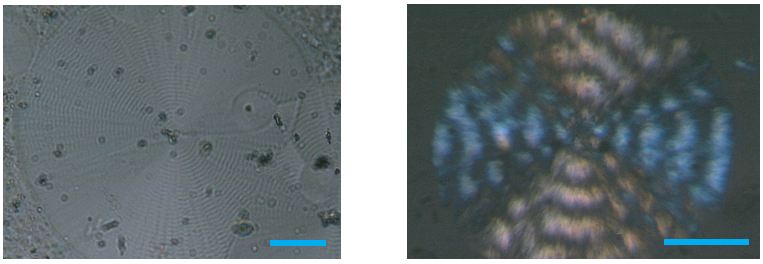

Figure 6.2: Left: Banded spherulite of pure PVDF spherulite. Right: Banded spherulite of PVDF/PEA = 30/70 blend. Scale bar: 50 μm

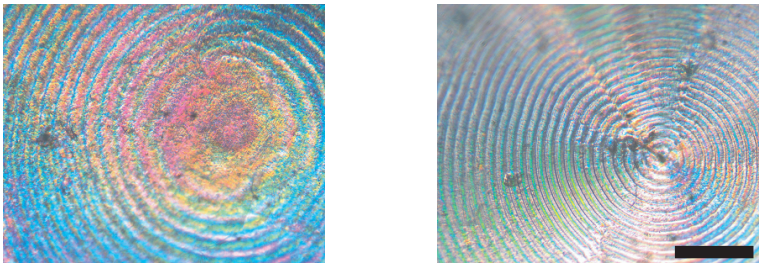

Figure 6.3: Cross section of spherulite grown in three dimensional space. Left: Samples without spherulite center. Right: Samples with the center. Scale bar: 100 μm.

sample was measured to be 5.0 μm $\times$ 5.0 μm in FWHM by wire-scanning. We used I.I.+ CCD detector. The CCD camera C4880-50 is full frame transfer type. The phosphor of the I.I. was P43, whose decay time is 1 ms.

The variable of this setup was wavelength and camera length. The requirements of the setup were as follows;

1. Higher angular resolution. We had to separate 110 refletion of PCL from neighboring 111 reflection.

2. Less image distortion. As summarized in Section 5.5.3, I.I. bears the image distortion problem. The problem is remarkable at outer region of I.I..

3. Less radiation damage

As Bragg-formula indicates, the diffraction moves toward small angle region with shorter wavelength. Longer camera length can achieve higher angular resolution. Certain degree of camera distance or longer wavelength was necessary for the requirement 1. In contrast, shorter wavelength or shorter camera length is favorable for the requirement 2. There is upper limit of wavelength (9 keV) because the higher order light of radiation cannot be completely excluded. Radiation damage increases at longer wavelength. Considering above, we set camera length and wavelength to be about 15 cm and 15 keV, respectively.

In standard x-ray scattering measurement, vacuum pipe are used for reducing noise stemming from air scattering. However, because of the short camera length, the vacuum pipe was not available. Instead, a small beam stop was placed just downstream of the sample. The exposure time was adjusted for each sample so that the CCD is not saturated. We scanned the spherulite along radial direction of spherulites with a micron step (Figure 6.4).

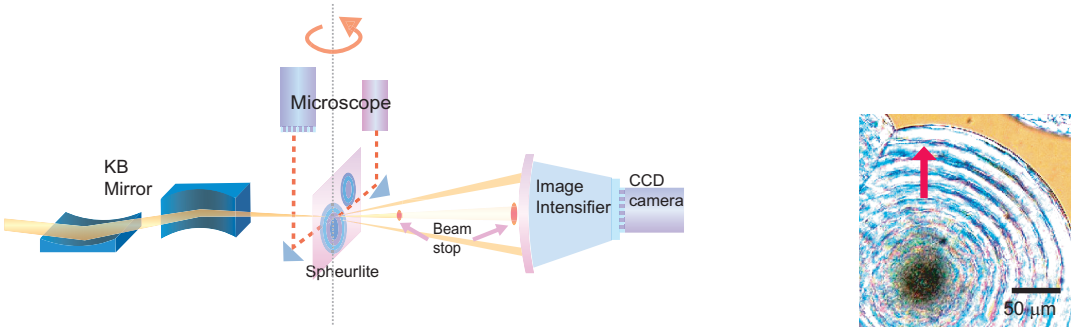

Figure 6.4: Left: Optical setup for microbeam WAXS measurement. Right: Microbeam was scanned in radial direction of spherulite.

6.3 Microbeam SAXS-WAXS simultaneous measurement

Microbeam SAXS-WAXS simultaneous measurement was performed at BL40XU, SPring-8. The light source is helical undulator. High flux is the feature of this beamline, because we can obtain quasi-monochromatic x-ray ($\Delta\lambda/\lambda \approx 10^{-2}$) without monochromator. Time resolved scattering measurement and X-ray photon correlation spectroscopy are conducted. The helical undulator in Spring-8 BL40XU consists of the magnet arrayed in side to side and up and down. The electron does not move in the xy-plane, but moves helicoidally. Higher harmonic waves are emitted out of the optical axis, and the high monochromaticity is achieved in the helical undulator. The wavelength ranging from 7 keV to 15 keV is available. The radiation from undulator is focused horizontally and vertically, by bending mirrors. To increase the critical angle and the cross section of incident beam, the surface of mirrors are coated with heavy atoms.

The experimental setup for our research is illustrated in Figure 6.5. The detectors of SAXS and WAXS were I.I.+ CCD and flat panel, respectively. The microbeam was made by placing a pinhole (ϕ = 5 μm). Guard pinhole (ϕ = 200 μm) was set at the downstream of the first pinhole to cut out the parasitic scattering. We could change the x-ray wavelength and camera distance. The camera distance of SAXS was set to be 3 m for high angular resolution, because we had to separate the lamellar reflections deriving from two kinds of PCL lamellar structure. The flat panel was placed close to the direct beam so that 110 reflection and 200 reflection of PCL were within the light sensitive area of flat panel of 5 cm squared. The wavelength was adjusted to be 10.5 keV to observe wider azimuthal range of WAXS reflections. 200 μm thick aluminum attenuator was placed at the upstream of the sample to relieve the radiation damage.

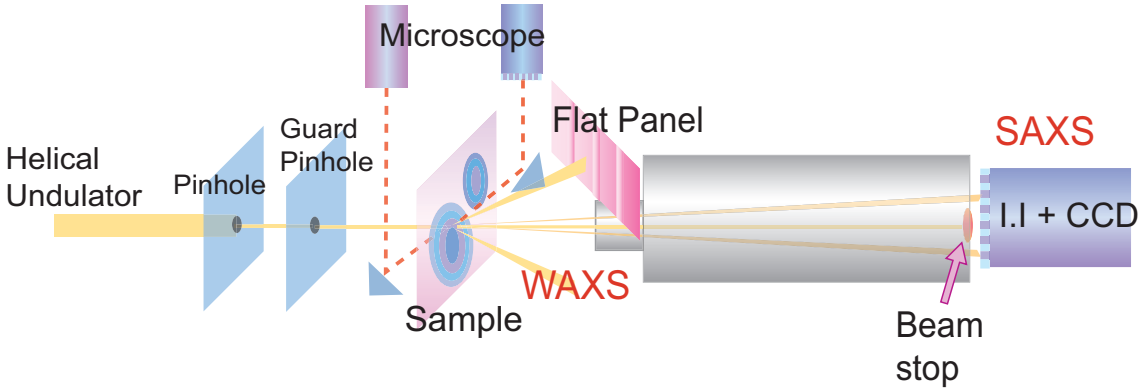

Figure 6.5: Experimental setup for microbeam SAXS-WAXS simultaneous measurement

Central pixel of the flat panel image was calibrated by the following procedure. The perpendicular bisector lines of arbitrary arcs of 110 reflection of PCL were drawn and the common intersection point was determined as the center. A circle was drawn from the calibrated central pixel to confirm that the 110 reflection was certainly on the circle (Figure 6.6).

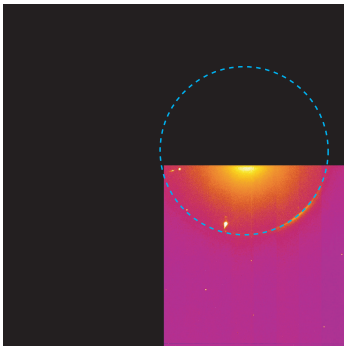

Figure 6.6: Center of the flat panel was finally confirmed by drawing a circle.

6.4 Polarized optical microscopy observation

BX50 (Olympus) was used for POM observation. The sample grown on the mica substrate was peeled off and placed on glass substrate when we analyze the lamellar orientation quantitatively. We employed the color filter IF546 (Olympus) for monochromatic light source. The dynamic range of the camera was 8 bit. We adjusted the brilliance of light source so that the maxima and minima of signal are within the range. The linearity of the signal was calibrated by rotating the analyzer by 2 degree at a time. The transmittance of analyzer is $\cos^2\theta$, if the angle between analyzer and polarizer is θ. The signals of 100 square pixels at the center of image were integrated for the confirmation of the linearity (Figure 6.7 Right).

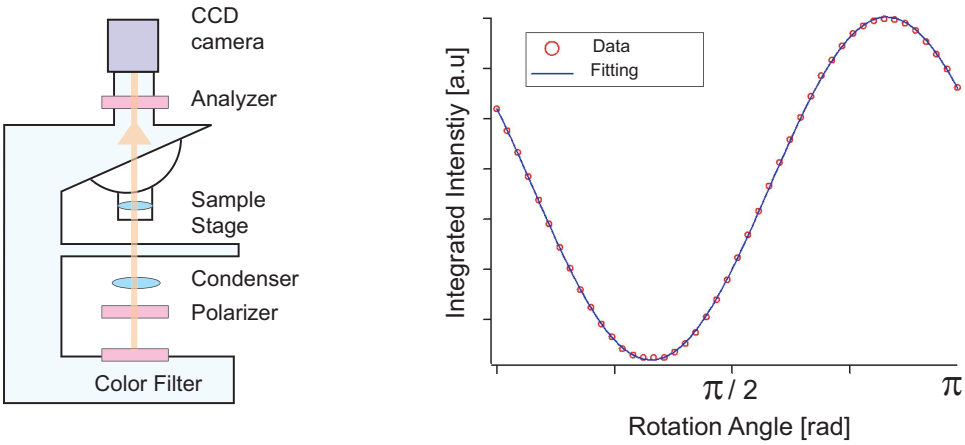

Figure 6.7: Left: Schematic view of POM. Right: Integrated intensity around the image center depending on the angle between the polarizer and analyzer. The profile was fitted with $\cos^2\theta$ to confirm the linearity.

Chapter 7

Data analysis and simulation

7.1 Analysis of lamellar twist by microbeam x-ray scattering

In this section, we consider how to determine if the stepwise lamellar twisting exists in spherulite form diffraction pattern of microbeam x-ray scattering.

7.1.1 Plot of azimuthal intensity distribution against radial distance in spherulite (Image-plot)

Diffraction pattern of microbeam WAXS is shown in Figure 7.1, where azimuthal intensity distribution broadens compared with single crystal. The patterns change depending on the lamellar orientation within the incident beam.

In the case of PCL, the diffractions from different facets are readily superimposed because of the extraordinary length of *c* axis. The doubling problem is less pronounced in lower facets.

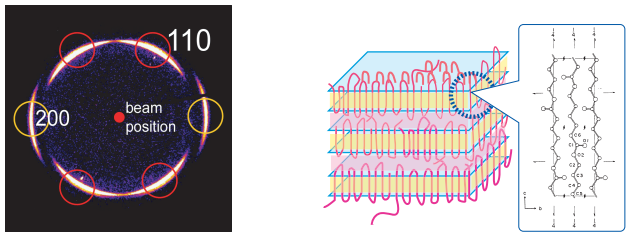

Figure 7.1: Left: hk0 reflections of PCL spherulite when folded chain is parallel with the incident x-ray. Right: Crystal structure of PCL. *c* axis is longer by more than two times than other axes.

When we plot the azimuthal intensity distribution of 110 diffraction against scanning distance (radial distance), the image in Figure 7.2 appears. In this thesis, we call it image-plot.

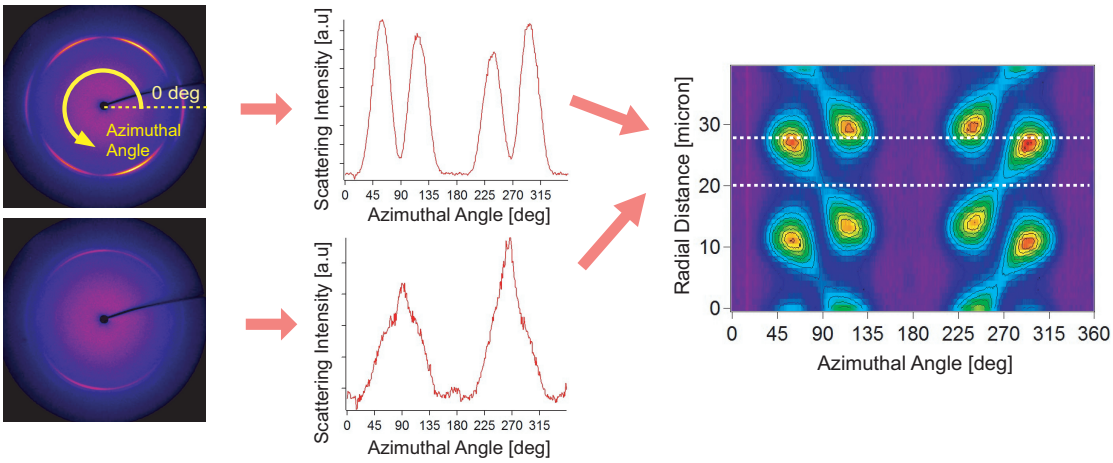

Figure 7.2: Left: 110 reflection of WAXS pattern was azimuthally rolled out. Center: Azimuthal intensity distribution of 110 reflections. Right: A series of the azimuthal profiles along radial direction of spherulite were plotted against radial distance.

We can determine twist sense and approximate twist phase from the image-plot. The information of twist sense can be obtained because of the curvature of Ewald sphere, which is lost at small angle region.

In the following, we consider the simulation of the azimuthal profiles of 110 reflection and how to determine whether or not stepwise lamellar twist exist by microbeam WAXS. The summary of previous works is given first [1]. After that, some modifications for better simulation are proposed.

When we analyze lamellar twisting phase, some unknown parameters are set. One is the distribution of crystal facet orientation with respect to solid angle. We also have to take into account the fluctuation of facets' spacing and limited stack number of unit cells. Finally we introduce the parameter representing the degree of non-uniformity of lamellar twisting.

7.1.2 Summary of previous simulation

Several sets of parameters describing the oriental distribution of crystal facet can be assumed. In the previous work, the concentration distribution on the reciprocal lattice sphere was assumed to be described by the norm defined as follows.

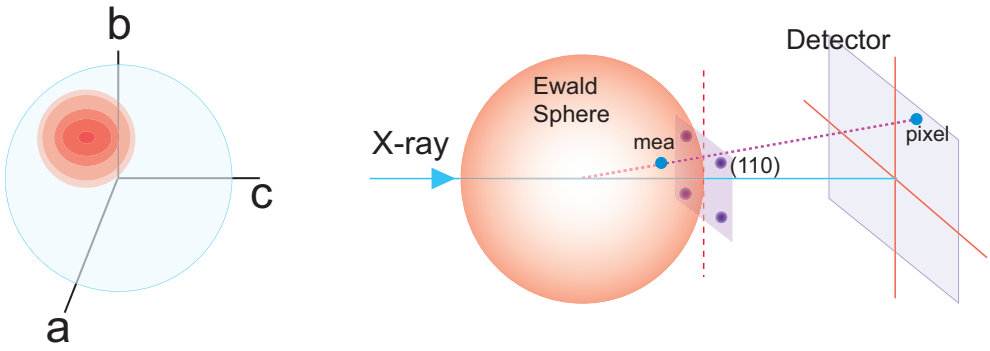

Figure 7.3: Left: Angular spread of (110) reciprocal spots on the reciprocal lattice sphere. Right: The position *mea* on the Ewald sphere corresponds to certain pixel of detector.

$$d^2_{reciprocal} = \frac{\cos^2\theta(\phi_{mea} - \phi_{lat})^2}{(\Delta\phi)^2} + \frac{(\theta_{mea} - \theta_{lat})^2}{(\Delta\theta)^2} \tag{7.1}$$

where rotational angle about b axis ϕ, the protruding angle from ac plane is θ. The FWHM of ϕ and θ are $\Delta\phi$ and $\Delta\theta$, respectively. *lat* is the ideal position of the reciprocal spot when the reciprocal spot could be written by delta function. The factor $\cos\theta$ on ϕ was adopted because the length on the reciprocal lattice sphere is not the same even if the difference of θ between the two points are identical.

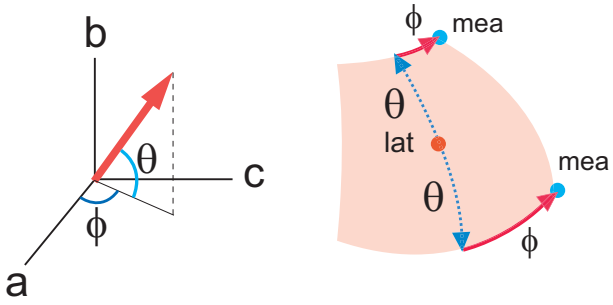

Figure 7.4: Left: Definitions of angular parameters in previous works. Right: The difference of ϕ at different θ position.

Next, the radial distribution of reciprocal spots was taken into account, which corresponds to the limited stack number of the unit cells and the fluctuation of facets' spacing as described in Section 4.1.5. The FWHM is defined as Δq. Combining with the oriental distribution, the concentration of reciprocal spot $\rho_{Fou}(\boldsymbol{q})$ is written as follows.

$$\rho_{Fou}(\boldsymbol{q})\, d\boldsymbol{q} = \exp\left(-\left(\frac{(q_{mea} - q_{lat})^2}{(\Delta q)^2} + \frac{\cos^2\theta(\phi_{mea} - \phi_{lat})^2}{(\Delta\phi)^2} + \frac{(\theta_{mea} - \theta_{lat})^2}{(\Delta\theta)^2} \right) \right) d\boldsymbol{q} \tag{7.2}$$

where $q = |\boldsymbol{q}|$. The step parameter t is defined in such a way that the phase of twist at x is $\theta_{twist}(x)$ is described

$$\theta_{twist}(x) = \pi\frac{x}{P} - t\sin\left(2\pi\frac{x}{P}\right) \tag{7.3}$$

where P is the band spacing (Figure 7.5). Note that lamellae twist 180 degree in a single banding.

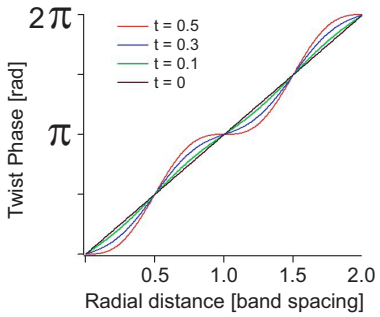

Figure 7.5: Step parameter

7.1.3 The issues to be overcome in previous works

Previous works leaves some points to be desired as following.

- Setting of unknown parameters
- Correction factor about the lamellar twist
- The range of θ

Before we consider the setting of unknown parameters, three kinds of the degree of rotational freedom of lamellae are introduced for convenience as illustrated in Figure 7.6. The rotational angle around b axis is defined as ϕ. The rotational angle around c axis is defined as θ. The rotational angle around a axis is defined as ψ.

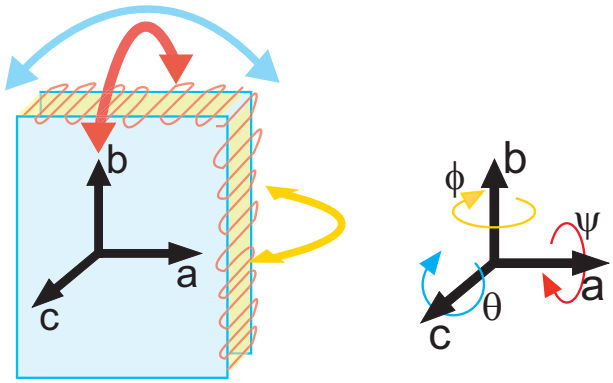

Figure 7.6: Definitions of angular parameters

The first issue of the previous work is that the degree of freedom around a axis is not considered. θ and ϕ corresponds to rotation around c axis, and b axis, respectively.

Secondly, the calculated scattering intensity have to be corrected to compare with the experimental data, considering the lamellae grow helicoidally along radial direction, b axis. As briefly summarized previously (Refer Section 4.1.6), the scattering intensity of the region with shallower α (α is the angle between rotational axis and the position vector in q space) is observed to be brighter than the area near equatorial. It is because the lamellae twist around the fixed axis. We can imagine this correction qualitatively with a spinning ring as illustrated in Figure 7.7. If it rotates around the fixed axis, the density is concentrated near the rotational axis than near the equatorial. Therefore, when we compare the calculated intensity with the experimental data, the calculated intensity has to be inversely Lorentz corrected, that is, multiplying $1/\sin\alpha$. It is because the differential ring shaped area dS at the angle α is $dS = 2\pi \sin\alpha d\alpha$.

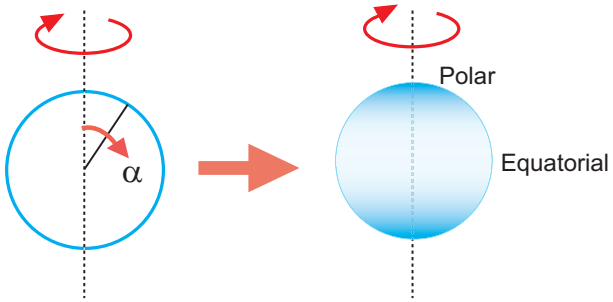

Figure 7.7: Spinning ring

Thirdly, the range of θ is limited by 90 degrees in previous works, which is inpractical because the 110 reflection is frequently over the right angle.

7.1.4 Proposal of modified simulation

We reconsidered the simulation method for above problems. Ideal simulation have to take into account the three types of freedom, however, it was not possible partly because the rotation manipulations are not commutative and thus mathematically difficult. Some compromise trials are shown in the following.

- Simulation I

First, we tried the case with two unknown parameters describing the oriental distribution of reciprocal spots. From section 8.3.6, it was found that the angular spread around a axis is narrow compared with other axes. Thus, we chose the bigger two angular distributions from the above three. The concentration of the reciprocal spot was assumed to be written in the form

$$\rho_{Fou}(\boldsymbol{q})\, d\boldsymbol{q} = \exp\left(-\left(\frac{(q_{mea} - q_{lat})^2}{(\Delta q)^2} + \frac{(\phi_{mea} - \phi_{lat})^2}{(\Delta\phi)^2} + \frac{(\theta_{mea} - \theta_{lat})^2}{(\Delta\theta)^2} \right) \right) d\boldsymbol{q} \qquad (7.4)$$

then, correction factor $1/\sin\alpha$ was applied. This proposal could not resolve the problems about the range of θ. The second problem is that the azimuthal intensity distribution when lamellae are edge-on is narrower compared with the observation results.

- Simulation II

Another example of the simulation was considered, where the distribution about solid angle is written by single parameter ω, which is defined by the angle between the position vector of the pixel and the reciprocal spot.

$$\omega = \cos^{-1}\left(\frac{\boldsymbol{q}_{mea}\cdot\boldsymbol{q}_{lat}}{|\boldsymbol{q}_{mea}||\boldsymbol{q}_{lat}|}\right) \tag{7.5}$$

This simulation is better in that it can avoid the problem about the range of θ.

$$\rho_{Fou}(\boldsymbol{q})\,d\boldsymbol{q} = \exp\left(-\left(\frac{(q_{mea}-q_{lat})^2}{(\Delta q)^2}+\frac{(\omega_{mea}-\omega_{lat})^2}{(\Delta\omega)^2}\right)\right)d\boldsymbol{q} \tag{7.6}$$

then, correction factor $1/\sin\alpha$ was applied. The simulation showed better result compared with Simulation I. The experimental data and the simulated data are shown in Figure 7.8.

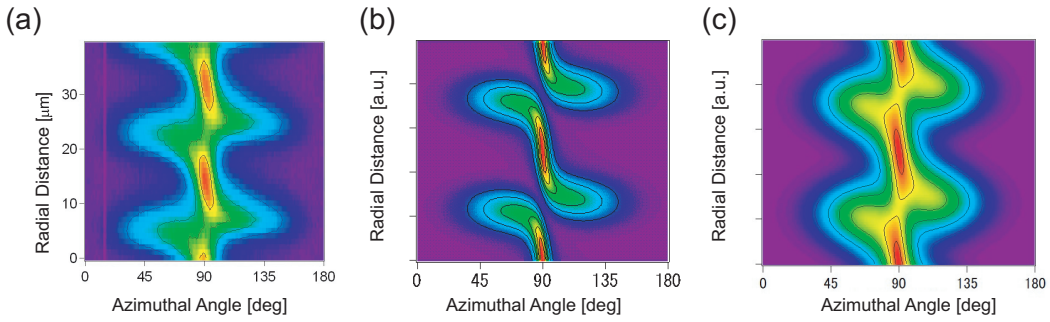

Figure 7.8: (a) Experimental data. (b) Simulation I (Δq = 0.05, $\Delta\theta$ = 25 deg, $\Delta\phi$ = 30 deg, stepparameter = 0.15). (c) Simulation II (Δq = 0.05, $\Delta\omega$ = 23.5 deg, stepparameter = 0.1).

7.1.5 Sample rotation

In previous works [1], image-plots of 110 reflection were simulated with the three unknown parameters; $\Delta\theta$, $\Delta\phi$, and the step parameter. As a result, any kinds of the image-plot of 110 reflection could be simulated with uniform rotation by changing the FWHM of θ, when the samples are perpendicular to the incident x-ray. Therefore, it was concluded that the existence of stepwise twisting cannot be determined by a single scanning measurement along spherulite radius [1]. To resolve this problem, diffraction measurement

with sample rotation was adopted to distinguish whether or not the stepwise twisting exists. As shown in Figure 7.9, the difference of the image-plot indicates that lamellae do not rotate uniformly.

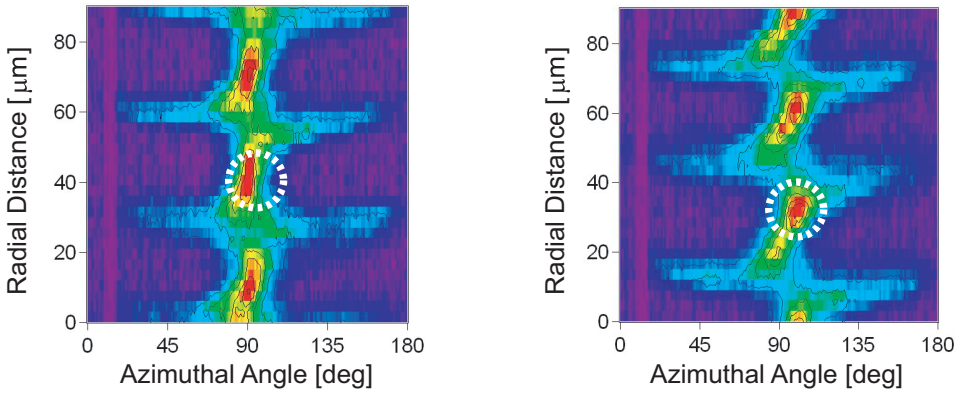

Figure 7.9: Difference of image-plot of 110 reflection depending on the sample rotation around spherulite radius (*b* axis). The rotational angle was 0 deg (Left) and 40 deg (Right).

7.1.6 Determination of stepwise twisting by analyzing other facets

In previous works, 110 reflections were used to determine whether or not the stepwise twist exist. However, in the case where the variance of reciprocal spot is small, in other words, crystal is well ordered, nonuniform lamellar twisting cannot be determined necessarily with shallow rotational angle of the samples, when we focus only on 110 reflection.

For example, if we assume the step function like Figure 7.10, where the twist phase is fixed when lamellae are edge-on, simulation gives almost no difference after the sample rotation when the rotational angle is 40 degree. The deviation from uniform twisting is undetectable while intense 110 reflection cannot be observed.

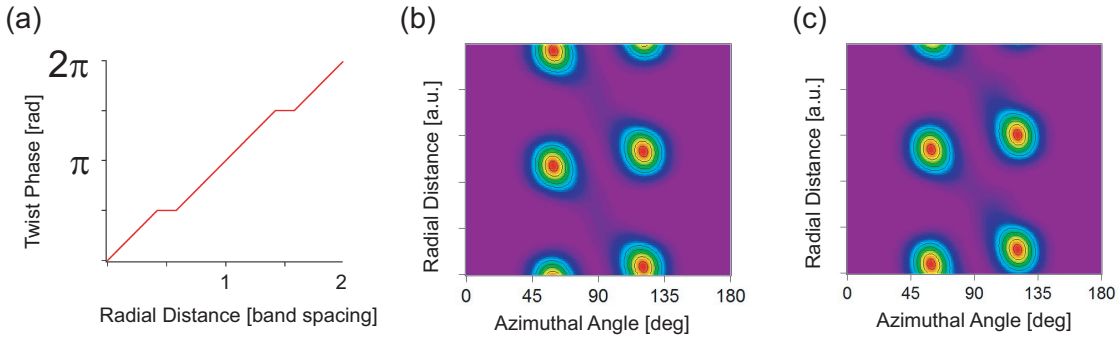

Figure 7.10: (a) New step function. (b)(c) Simulated image-plots of 110 reflection. Rotational angles of the sample are 0 degree (b) and 40 degree (c) (Simulation II, $\Delta\omega$ = 12 degree).

It is principally possible to determine the stepwise twisting by rotating the sample to much larger angle. However, it may be experimentally difficult, because the horizontal length where x-ray traverses increases proportionally to $1/\cos\omega_{rot}$, where ω_{rot} is the rotational angle of the sample (Figure 7.11). Large value of $1/\cos\omega_{rot}$ leads to the increase of the irradiated lamellae, and thus sometimes involves the lamellae which are not coherent with others. To resolve this problem, thinner sample have to be prepared for the experiment which involves large ω_{rot}. Nevertheless, thinner sample less than 5-10 μm frequently does not show regular bandings. Therefore, it may be desirable to conduct the sample rotation experiment with shallower ω_{rot}.

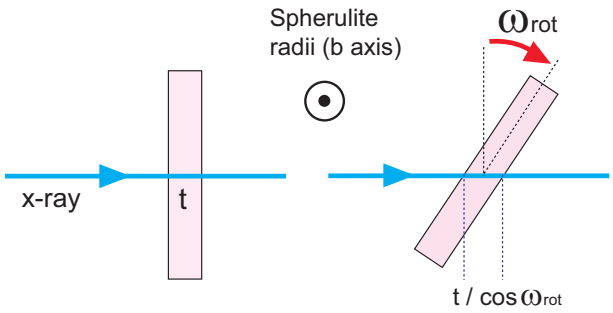

Figure 7.11: Horizontal length where x-ray traverses is proportional to $1/\cos\omega_{rot}$.

In order not to overlook the non-uniformity, the diffractions from other facets or from lamellae have to be simultaneously analyzed. For example, (102) facet satisfies Bragg condition two times more than hk0 reflections, thus the period without diffraction is comparatively short.

Moreover, focusing on 110 reflection has disadvantage in that the observation of 110 reflection is very sensitive to the sample inclination. The b^* axis is longer that a^* axis in reciprocal space, because a axis is longer than b axis in real space. Therefore, reciprocal spot of (110) facet is near the b axis. Hence, the degree of the asymmetry of diffraction pattern when the sample is inclined with respect to the x-ray normal (Figure 7.12) is enhanced, particularly in the case of 110 reflection than the case of h0ℓ reflections which are remote from b axis. The calculation result is shown in Figure 7.13 and Figure 7.14, where sample inclination by 2 degree is assumed. The degree of asymmetry is more remarkable in the case of 110 reflection than the case of 200 reflection. Therefore, we have to pay attention to h0ℓ reflections, which are relatively indifferent to the sample inclination problem.

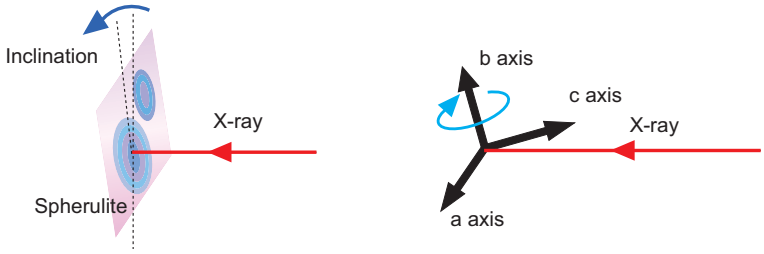

Figure 7.12: Left: Sample inclination with respect to the incident beam. Right: Twisting axis of lamellae (*b* axis) deviates from the plane normal to the incident x-ray.

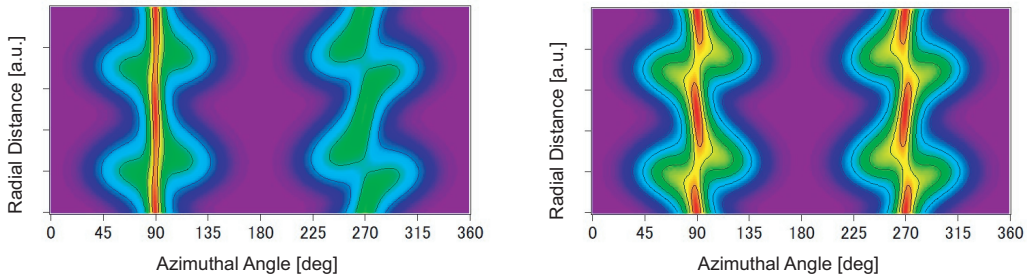

Figure 7.13: Calculated image-plot of 110 reflection (Simulation II, $\Delta\omega$ = 24 deg, stepparater = 0.1). Left: Image-plot of 110 reflection with the inclination by 2 degree. Right: Image-plot of 110 reflection without the inclination.

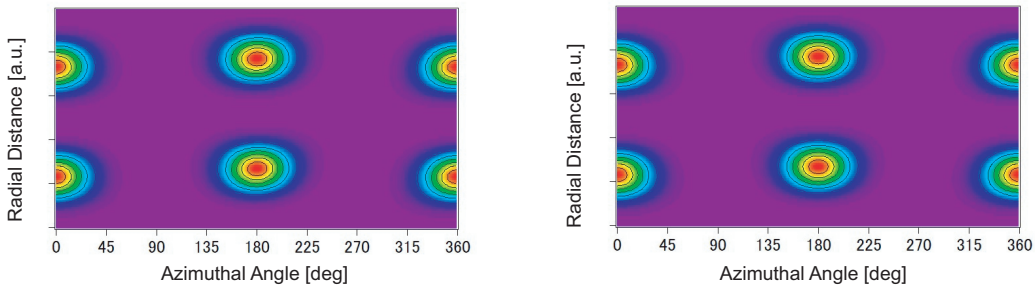

Figure 7.14: Calculated image-plot of 200 reflection (Simulation II, $\Delta\omega$ = 24 deg, stepparater = 0.1). Left: Image-plot of 200 reflection with the inclination by 2 degree. Right: Image-plot of 200 reflection without the inclination.

7.1.7 Microbeam SAXS

Existence of stepwise lamellar twisting can be determined by microbeam SAXS measurement, as in the case of WAXS described in Section 7.1.5. Previous work [1] demonstrated that the integrated intensity profile of lamellar reflection along spherulite raddi is different

when the sample is rotated. The result of microbeam SAXS in previous work is shown (Figure 7.15).

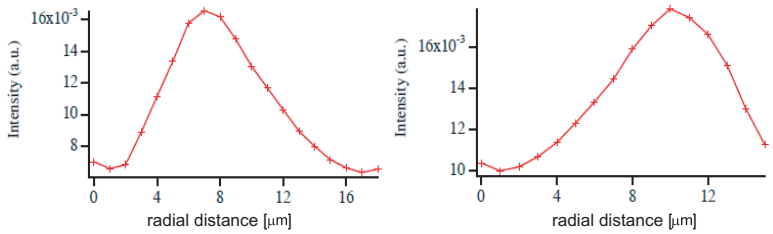

Figure 7.15: Integrated intensity of lamellar reflection along spherulite radial direction. Left: Sample rotation by -45 degree. Right : Sample rotation by +45 degree [1].

7.2 Analysis of lamellar twist with POM

Here, the quantitative analysis procedure of lamellar twist by POM is considered [58]. The numerical ellipsoid, analyzer, polarizer, and wavevector are placed in xyz-space as shown in Figure 7.16, where n_{long} and n_{short} are the indices of long axis and the short axis of the cross sectional ellipsoid. The amplitude of porlarized light can be decomposed into $E\cos\mu$ in n_{short} direction and $E\sin\mu$ in n_{long} direction. The phase difference of these two is $\delta = \frac{2\pi}{\lambda} d_0(n_{long} - n_{short})$, where λ is the wavelength.

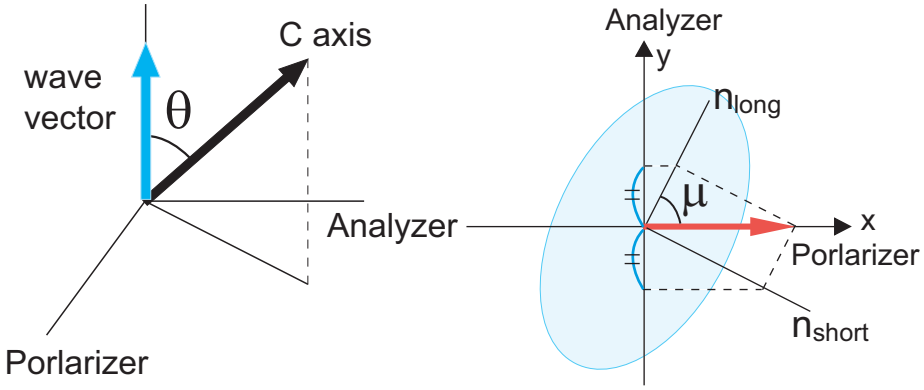

Figure 7.16: Coordinates of analyzer, polarizer and the cross section of index ellipsoid

The amplitudes of the two constituents are

$$y = \frac{E\sin 2\mu}{2}\sin(\omega t) \quad y' = \frac{E\sin 2\mu}{2}\sin(\omega(t-\tau)) \tag{7.7}$$

The synthesized waveform and its intensity are

$$y_{total} = E\sin 2\mu\cos\frac{\tau}{2}\sin\left(\omega\left(t-\frac{\tau}{2}\right)\right) \tag{7.8}$$

$$I = E^2 \sin^2 2\mu \sin^2 \left(\frac{\pi d_0 (n_{long} - n_{short})}{\lambda} \right) \tag{7.9}$$

In the case of uniaxial crystal where $n_a = n_b = n_0$, with Equation 4.47, we obtain

$$n_{long} = n_e = \frac{n_0 n_c}{\sqrt{n_0^2 \sin^2\theta + n_c^2 \cos^2\theta}} \tag{7.10}$$

$$n_{short} = n_0 \tag{7.11}$$

where θ is the angle between wave vector of the light and c axis. We can eliminate μ from above equations and obtain the information on θ by superimposing the image where polarizer and analyzer are rotated with respect to the sample by 45 degree.

$$I_{45} = I_0 \sin^2 2\left(\mu + \frac{\pi}{4}\right) \sin^2 \left(\frac{\pi d_0 (n_e - n_0)}{\lambda} \right) = I_0 \cos^2 2\mu \sin^2 \left(\frac{\pi d_0 (n_e - n_0)}{\lambda} \right) \tag{7.12}$$

$$I_{total} = I + I_{45} = I_0 \sin^2 \left(\frac{\pi d_0 (n_e - n_0)}{\lambda} \sin^2\theta \right) \tag{7.13}$$

The stepwise lamellar twisting can be principally analyzed by Equation 7.13. Here we assume uniaxial crystal, and set the unknown three parameters, that is to say, degree of refractive anisotropy n_c/n_0, the product of sample thickness and the index of ordinary wave $n_0 d_0$, and the step parameter t as described in the microbeam Section (Figure 7.5). The refractive anisotropy depends on the degree of crystallinity. The approximation of uniaxial crystal holds true, because the double extinction ring observed in biaxial crystal [59] was not detectable in PCL crystal. The wavelength distribution is not considered, because the light is mochromized to the order $\Delta\lambda/\lambda = 10^{-2}$ with color filter IF546-45 (Olympus).

Chapter 8

Result and Discussion

8.1 Polarized optical microscopy

8.1.1 Growth rate of PCL/PVB spherulite

The growth front of spherulite was defined as the radial position with the minimum of the light intensity around the contour of the spherulite (Figure 8.1).

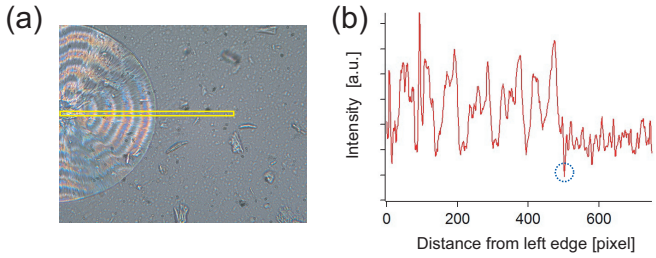

Figure 8.1: The line profile of the yellow area (a) is shown in (b). Growth front was defined as the position where the intensity reaches minimum near the growth front (The blue circle in (b)). 1 pixel corresponds to 0.19 μm.

It has been reported that the growth rate of the spherulite decreases under higher PVB concentration or higher crystallization temperature. This tendency was confirmed as shown in Figure 8.2. It is conceivable that PCL molecules are hard to creep out from the tangled melt, where PVB and PCL molecules strongly interact each other.

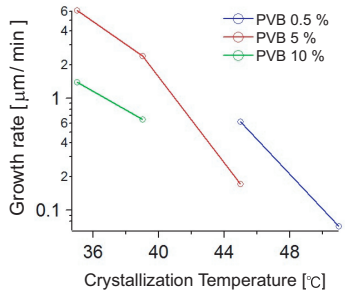

Figure 8.2: Growth rate of spherulite under various condition.

More time-resolved measurement was conducted with the sample (PCL/PVB = 95/5, Tc = 48 ℃). It was found that radial growth rate of the spherulite fluctuates, and that edge-on lamellae grow slower than flat-on lamellae as shown in Figure 8.3.

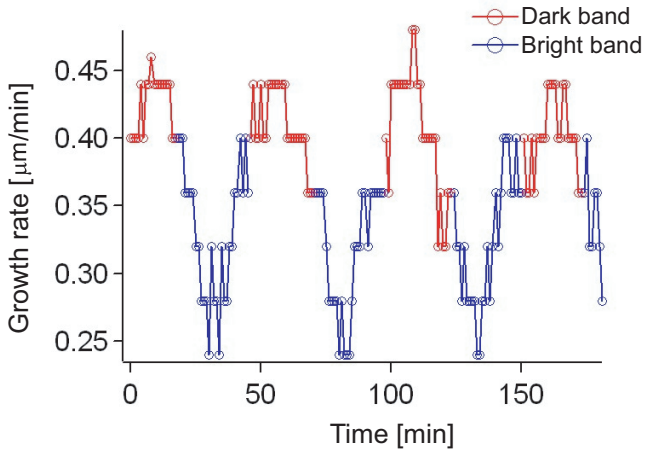

Figure 8.3: Growth rate of the spherulite (PCL/PVB = 95/5, Tc = 48 ℃). Dark band and Bright band correspond to flat on lamellae and edge on lamellae, respectively.

8.1.2 Analysis of stepwise twisting

The analysis of stepwise twisting was conducted according to the procedure in Section 7.2

First, two photographs with the two polarized directions differing by 45 degree were superimposed to eliminate the Maltese cross. After that, the line profile was sectored from the image (Figure 8.4).

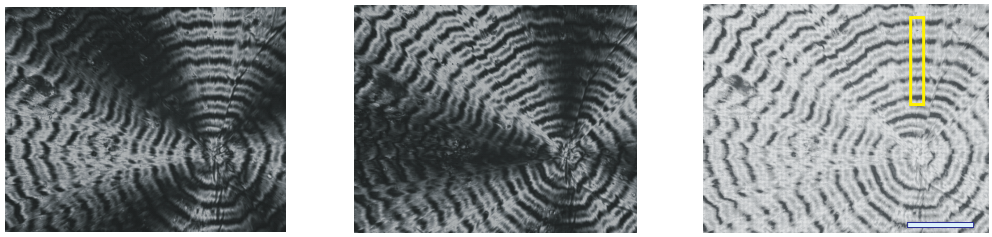

Figure 8.4: Left and Center: Two images with the two polarized directions differing by 45 degree. Right: Superimposed image. Scale bar: 50 μm.

Next, the profile was fitted with the equation

$$I_{total} = I_{0\ \mathrm{deg}} + I_{45\ \mathrm{deg}} = I_0 \sin^2\left(\frac{\pi d_0(n_e - n_0)}{\lambda} \sin^2\theta\right) \tag{8.1}$$

which involves three unknown parameters, the product of sample thickness and PCL refractive index $n_0 d_0$, the anisotropy of index ellipsoid n_c/n_0, and step parameter, as shown in Figure 8.5 (Refer Section 7.2). Some of the radial intensity distributions showed second valleys between the maxima. It is because the term $\pi d_0(n_e - n_0)\ /\ \lambda$ exceeds $\pi/2$.

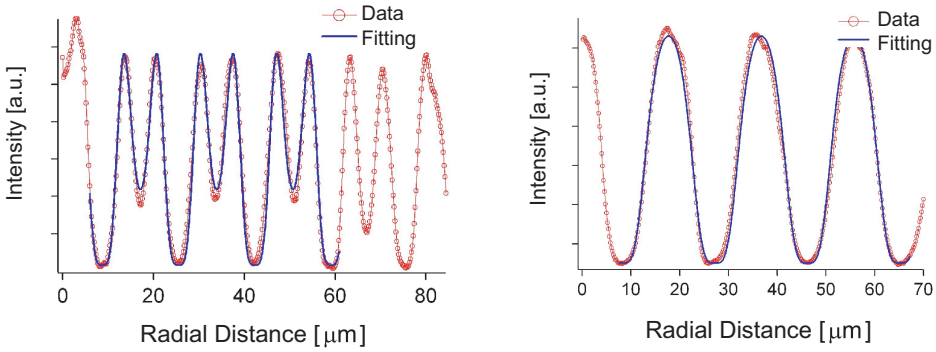

Figure 8.5: Typical examples of the radial profile of the POM images. Left: PCL/PVB = 95/5, Tc = 39 ℃. Right: PCL/PVB = 95/5, Tc = 45 ℃. Note that the apparent difference of the two derives from the sample thickness by a few micron.

The step parameter is plotted against the crystallization temperature as shown in Figure 8.6. It was confirmed that the nonuniformity of the lamellar twisting increases under high crystallization tempearature. Moreover, it was confirmed that the change rate of twist phase $d\theta/dr$ reaches minima when chains are parallel with the substrate. These result fall in well with the result of microbeam x-ray scattering in previous works [1].

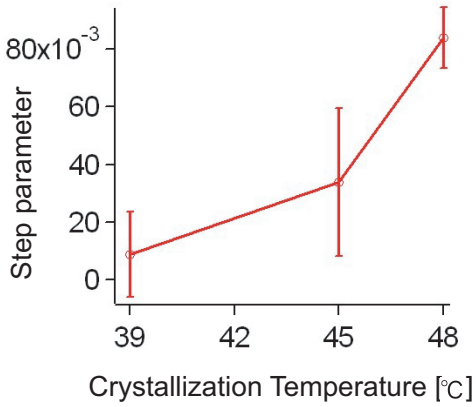

Figure 8.6: The dependence of the step parameter on the crystallization temperature. PCL/PVB = 95/5.

8.2 Microbeam SAXS and SAXS-WAXS simultaneous measurement

Sector with bright lamellar reflection was cut out from the two dimensional data of SAXS (Figure 8.7 Left). The radial intensity distribution was azimuthally averaged. After that, it was Lorentz corrected, as mentioned in Section 4.1.6 (Figure 8.7 Right).

It has been reported that two kinds of lamellar structure exist in PCL/PVB (Refer Section 2.4.1), thus the corrected profile was fitted with superimposed two Gaussians. We define the integrated scattering intensity from lamellae as the sum of the two Gaussian areas (Figure 8.7).

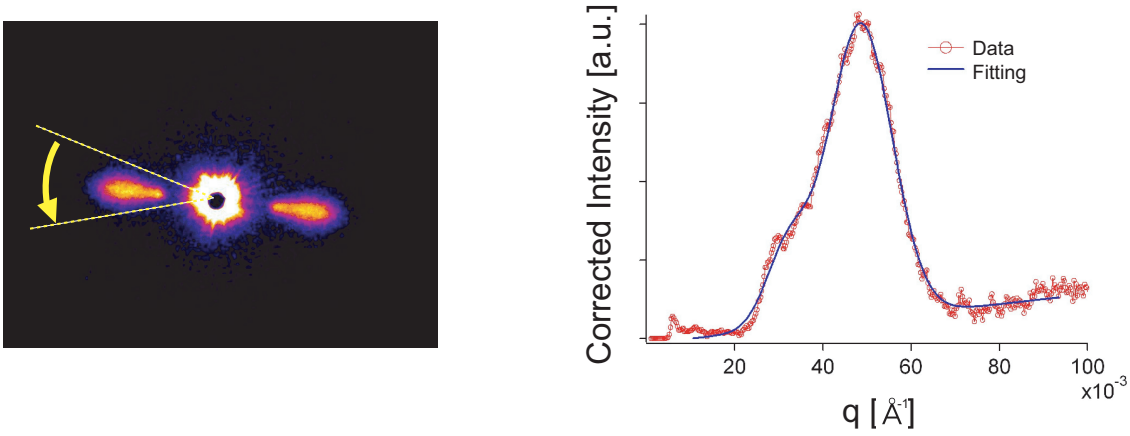

Figure 8.7: Left: The sector with bright lamellar reflection was cut out. Right: The corrected profile was fitted with two Gaussians.

8.2.1 Comparison of 2D sherulite and 3D spherulite

The integrated scattering intensity from lamellae was plotted against radial distance. The profiles with and without sample rotation around the radius of spherulite were compared (Figure 8.8). As explained in Section 7.1.7, the uniformity of lamellar twisting can be determined from the discrepancy between the two profiles. In the case of 2D spherulite, slight difference can be confirmed between the two, whereas the profiles of 3D spherulite relatively coincide. This indicates that non-uniformity of lamellar twist is more enhanced in 2D spherulite.

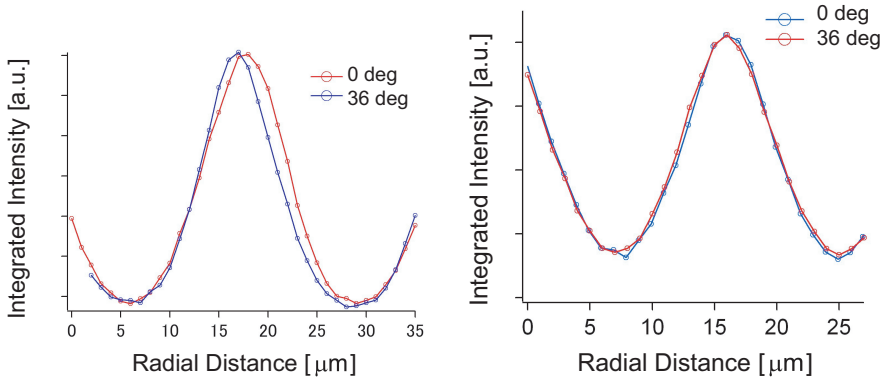

Figure 8.8: Integrated intensity profile of lamellar reflection along radial direction. Left: 2D spherulite, Right: 3D spherulite.

8.2.2 Azimuthal intensity distribution of lamellar reflection

The azimuthal intensity distribution of lamellar reflection was evaluated. Radial sector with lamellar reflection was cut out and azimuthally rolled out. FWHM of the azimuthal intensity distribution was estimated by fitting the profile by Gaussian (Figure 8.9 (a)(b)).

The dependence of the FWHM on the crystallization temperature is plotted in Figure 8.9 (c). All data are about the sample with 5 percent PVB. It was found that the FWHM of the azimuthal intensity distribution of lamellar reflection is around 7-9 degree, and that the FWHM slightly decreases under high crystallization temperature.

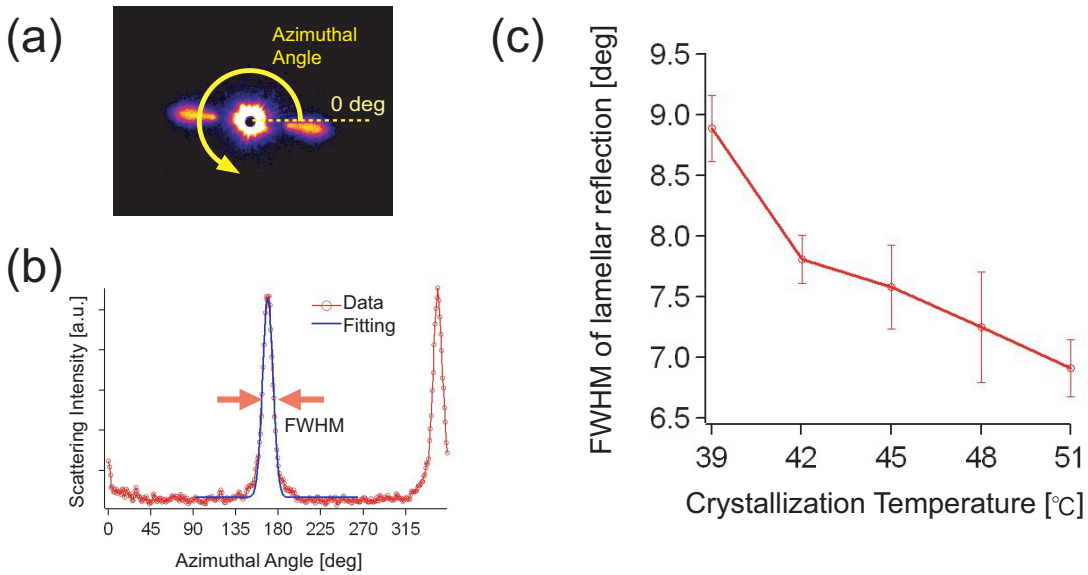

Figure 8.9: (a) Radial sector was cut out from the scattering pattern. (b) The azimuthal intensity distribution was fitted by Gaussian. (c) The FWHM of SAXS azimuthal intensity distribution is plotted against crystallization temperature.

8.2.3 Chain tilt in PCL/PVB spherulite

The twist phase of lamellae and that of folded chain can be determined from SAXS and WAXS, respectively. As discussed in Section 2.3.2, it is well known that the tilting angle of folded chain to lamellar normal increases under high crystallization temperature. Besides, it has been reported that the blend polymer may cause the crystalline polymorphism, where crystal structure changes from orthorhombic to monoclinic [49]. This means that the tilting angle may increase under high PVB concentration. The tilting angle can be estimated accurately if the bandwidth is longer under dilute PVB concentration.

Considering above, we observed the sample grown under high crystallization temperature and dilute PVB concentration (PCL/PVB = 99.5/0.5, Tc = 53 ℃), and the sample grown under high crystallization temperature and high PVB concentration (PCL/PVB = 95/5, Tc = 51 ℃).

The integrated intensity from lamellae and the azimuthal intensity distribution of 110 reflection are shown in Figure 8.10 about the sample with PCL/PVB = 99.5/0.5, Tc = 53 ℃ (Refer Section 7.1.1). Shift of the twist phase between lamellae and the folded chain was not detected, which means that the tilting angle is within 180/(bandwidth) = 3.6 degree, assuming the uniform rotation of lamellae along radial direction.

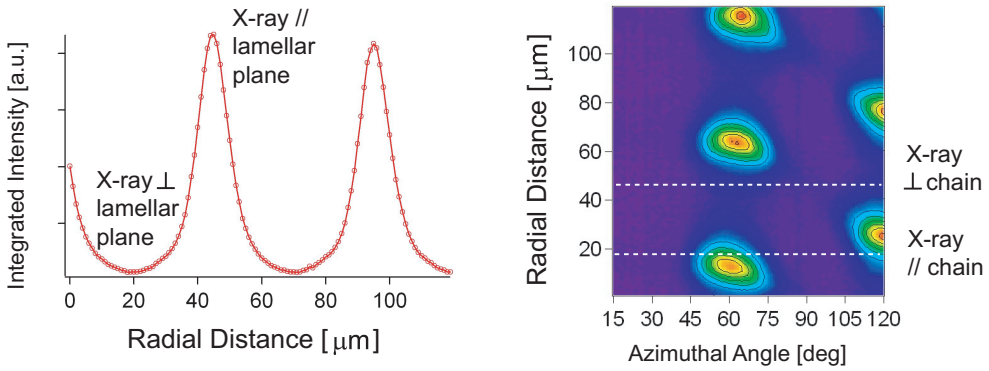

Figure 8.10: Left: Integrated intensity distribution of lamellar reflection along radial direction. Right: Image-plot of azimuthal intensity distribution of 110 reflection along radial direction. SAXS and WAXS were simultaneously measured.

Similar analysis was conducted on the PCL/PVB = 95/5, Tc = 51 ℃ sample. The discrepancy of the twist phase was also undetectable in this case (Figure 8.11).

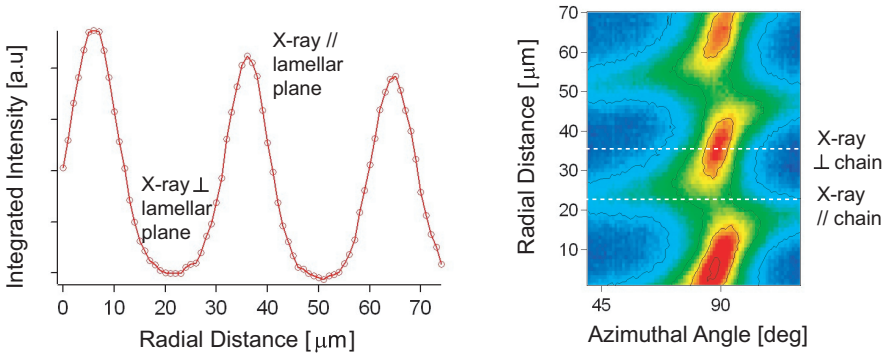

Figure 8.11: Left: Integrated intensity distribution of lamellar reflection along radial direction. Right: Azimuthal intensity distribution of 110 reflection along radial direction.

8.2.4 Chain tilt in PVDF/PEA spherulite

The WAXS pattern of PVDF/PEA spherulite is shown in Figure 8.12 (Left). We analyzed the twist phase of folded chain by azimuthally integrated 110 reflection. The azimuthally integrated data and 110 reflection was fitted with Gaussian. The twist sense was determined from the image-plot of the azimuthal intensity distribution of 110 reflection (Figure 8.12 (Right)).

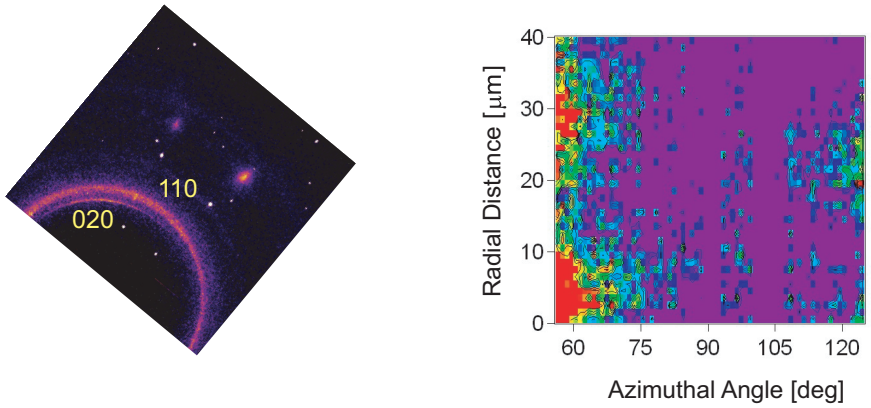

Figure 8.12: Left: WAXS pattern of PVDF/PEA spherulite. Right: The azimuthal intensity distribution of 110 reflection along spherulite raddi.

Two dimensional pattern of SAXS and Lorentz corrected intensity of PVDF/PEA spherulite are shown in Figure 8.13, where lamellar reflection is weak. The scattering from higher order scale was comparable with lamellar reflection. It derives probably from interference between the bundles of lamellae (fibrils). Therefore, the profile was fitted as the superposition of Debye-Bueche equation (Refer Section 4.1.4) and Lorentzian peak (Figure 8.13). The scattering intensity deriving from lamellae was defined as the area of the Lorentzian.

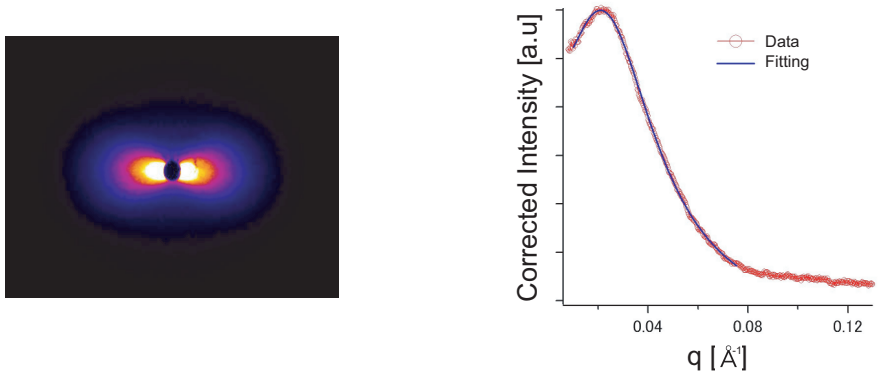

Figure 8.13: Left: SAXS pattern of PVDF/PEA spherulite. Right: Lorentz corrected SAXS intensity profile. Correlation length was about 1000 Å and lamellar period was about 250 Å.

The integrated intensity of lamellar reflection and integrated intensity from 110 reflection are plotted against radial distance (Figure 8.14). The twist sense was determined to be right-handed screw along radial direction from the image-plot (Figure 8.12). These results indicate that the twist phase of folded polymer chain proceeds compared with lamellar normal. This relationship is in accord with the previous reports [20][26]. The tilting angle was about 20 - 30 degree which coincides with the result of electron diffraction in single crystal [22].

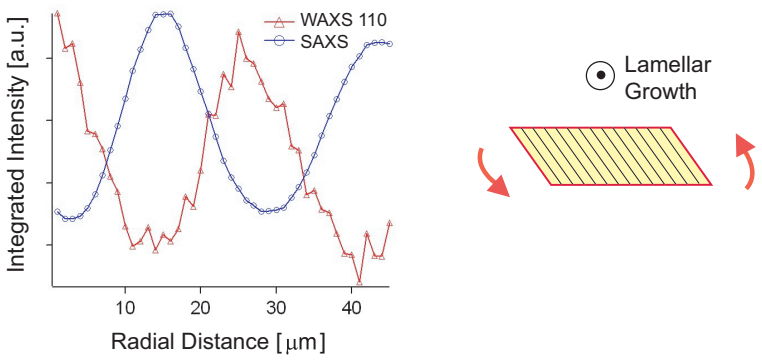

Figure 8.14: Left: Integrated scattering intensity from lamellae and 110 reflection. Right: The sense of lamellar twisting and its correlation with the tilt of folded chain.

8.3 Microbeam WAXS

8.3.1 Determination of stepwise lamellar twisting from 110 reflection

The sample was rotated around spherulite radii (Refer Section 7.1.5). We determined whether or not the stepwise twisting exist by the criterion that lamellae twist non-uniformly if the image-plot of 110 reflection changes when the sample was rotated. The image-plots of 110 reflection under various conditions are shown in Figure 8.16- Figure 8.24.

Summarizing matrix regarding the stepwise twisting is shown in Figure 8.15. It is certain that the stepwise twisting occurs under high PVB concentration or high crystallization temperature. We cannot determine whether or not stepwise lamellar twisting exist in the case where the distribution of reciprocal spots is narrow as shown in Figure 8.16 and Figure 8.17, because the non-uniformity of lamellar twist may exist during the period where 110 reflection does not appear (Refer Section 7.1.6).

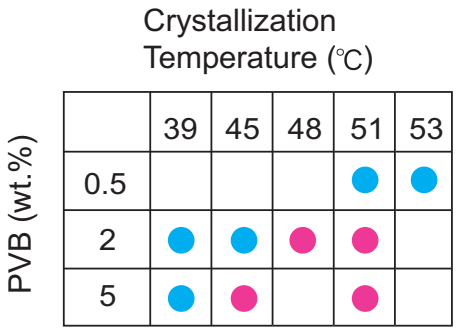

Figure 8.15: Determination of the stepwise twisting with 110 reflection. The difference of the image plot was detected (Pink) or was not detected (Blue).

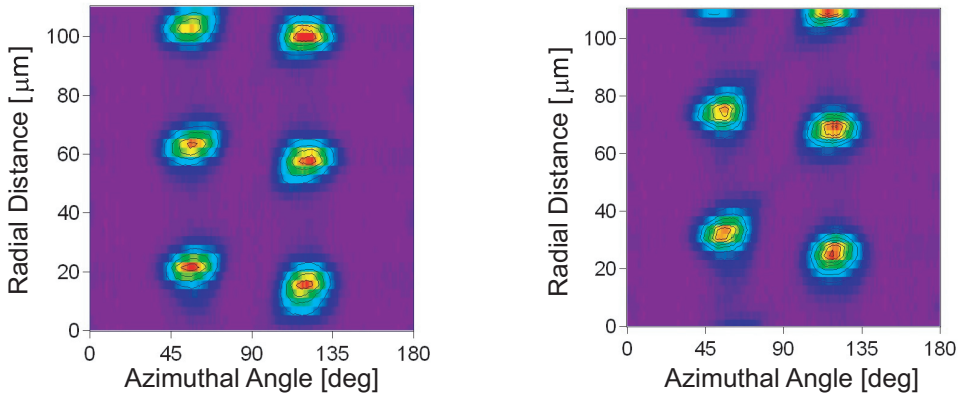

Figure 8.16: Image-plot of 110 reflection along the radial direction. PCL/PVB = 99.5/0.5, Tc = 51 ℃. Left: 0 degree, Right: 40 degree.

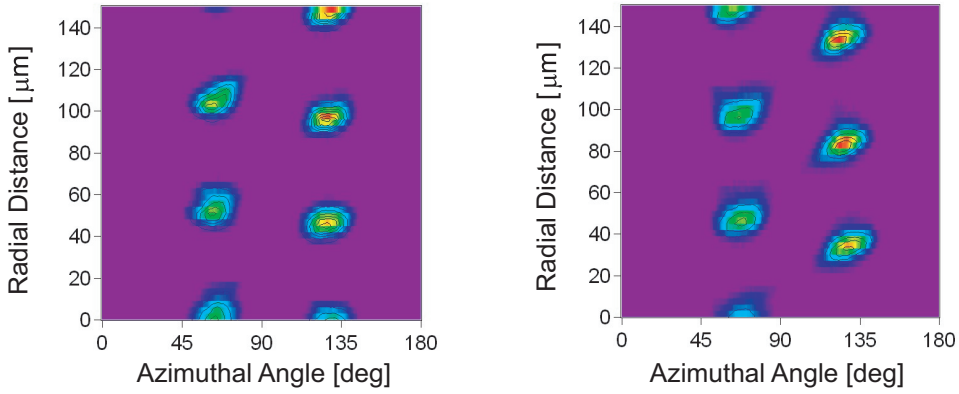

Figure 8.17: Image-plot of 110 reflection along the radial direction. PCL/PVB = 99.5/0.5, Tc = 53 ℃. Left: 0 degree, Right: 40 degree.

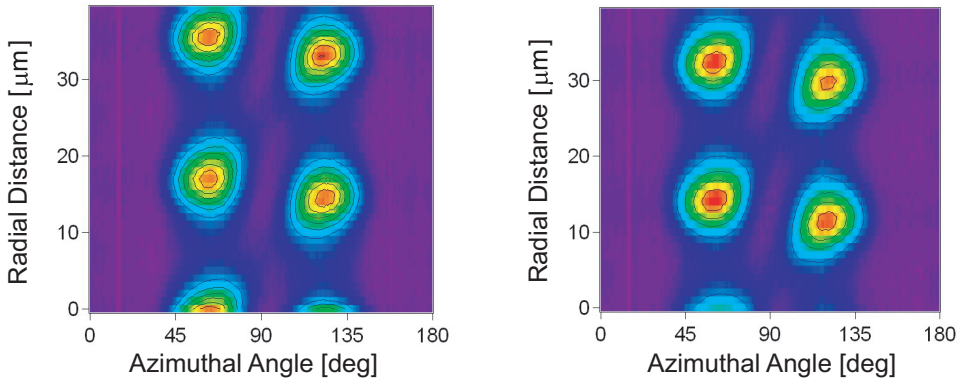

Figure 8.18: Image-plot of 110 reflection along the radial direction. PCL/PVB = 98/2, Tc = 39 ℃. Left: 0 degree, Right: 40 degree.

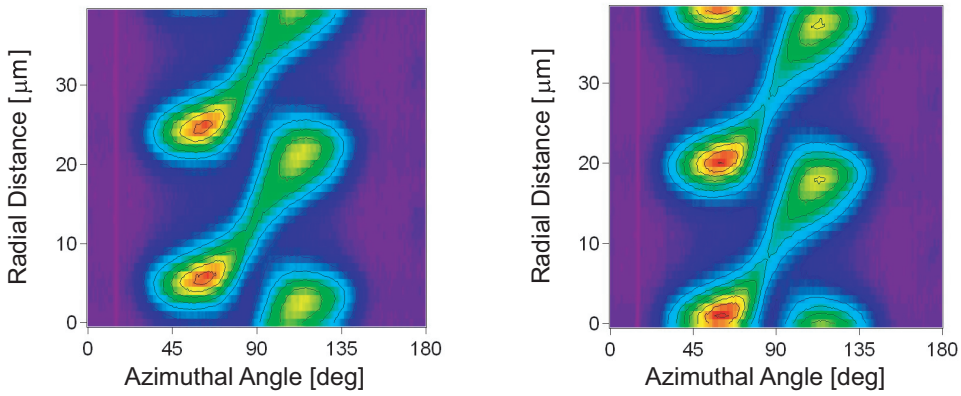

Figure 8.19: Image-plot of 110 reflection along the radial direction. PCL/PVB = 98/2, Tc = 45 ℃. Left: 0 degree, Right: 40 degree.

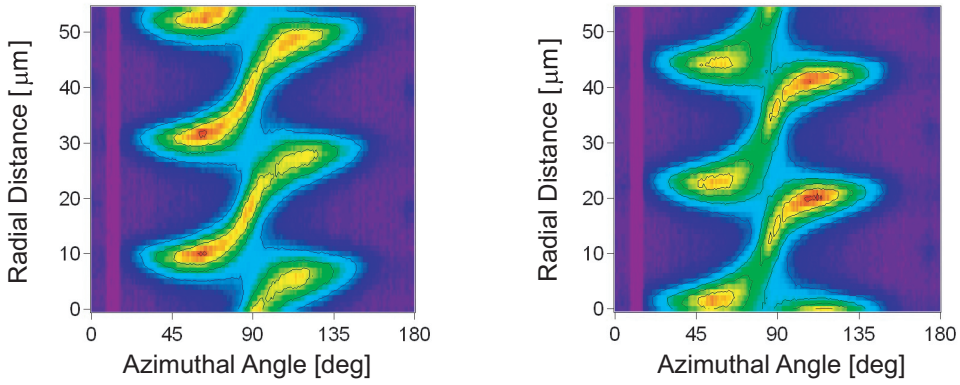

Figure 8.20: Image-plot of 110 reflection along the radial direction. PCL/PVB = 98/2, Tc = 48 ℃. Left: 0 degree, Right: 40 degree.

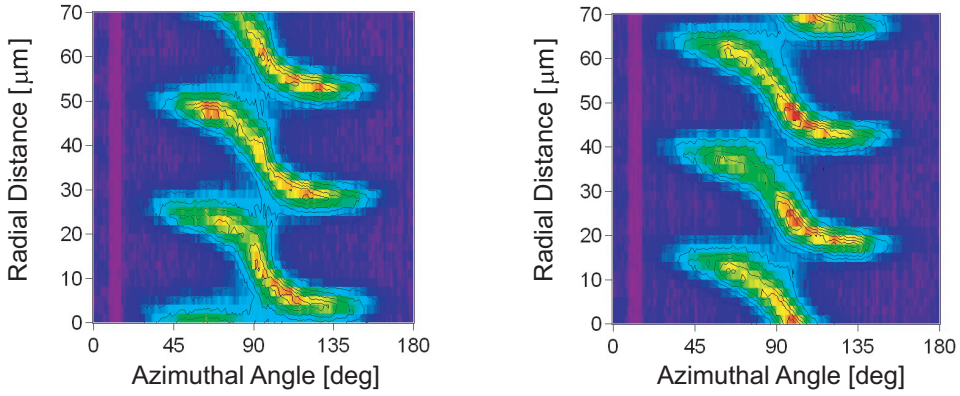

Figure 8.21: Image-plot of 110 reflection along the radial direction. PCL/PVB = 98/2, Tc = 51 ℃. Left: 0 degree, Right: 40 degree.

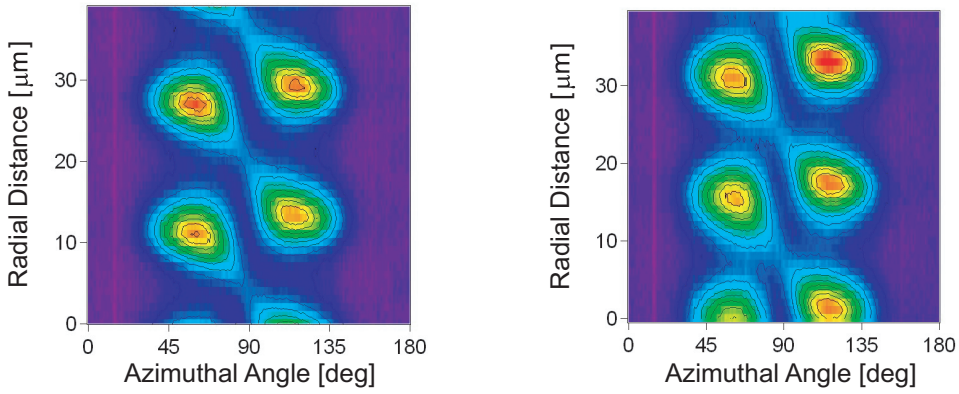

Figure 8.22: Image-plot of 110 reflection along the radial direction. PCL/PVB = 95/5, Tc = 39 ℃. Left: 0 degree, Right: 40 degree.

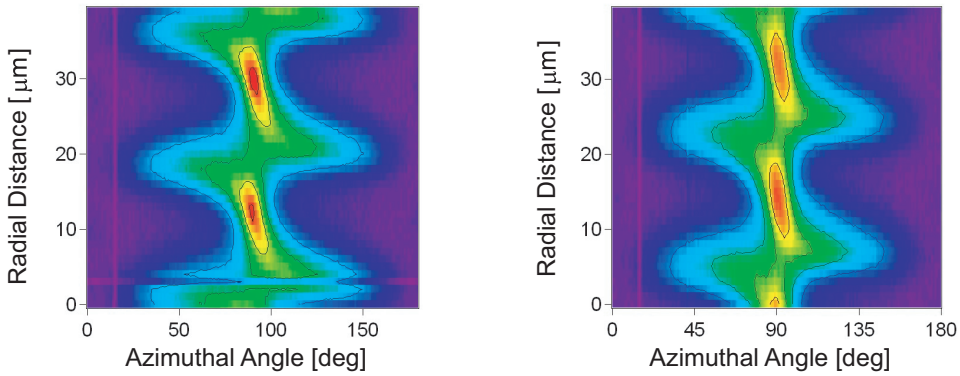

Figure 8.23: Image-plot of 110 reflection along the radial direction. PCL/PVB = 95/5, Tc = 45 ℃. Left: 0 degree, Right: 40 degree.

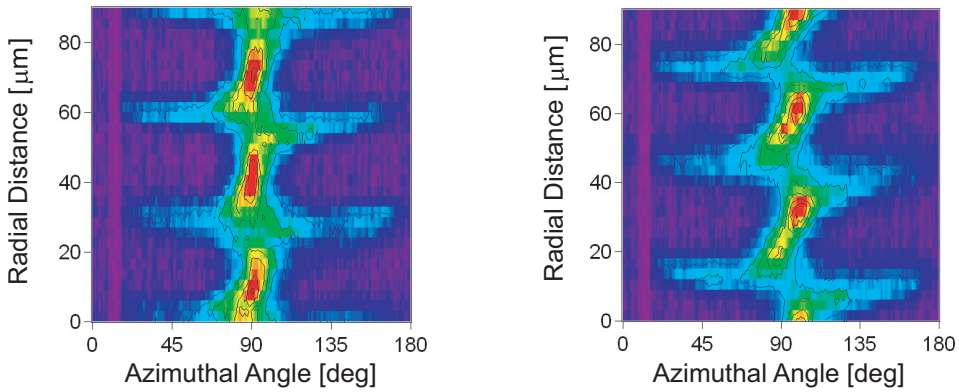

Figure 8.24: Image-plot of 110 reflection along the radial direction. PCL/PVB = 95/5, Tc = 51 ℃. Left: 0 degree, Right: 40 degree.

8.3.2 Determination of stepwise twisting by analyzing other facets

As discussed in Section 7.1.6, reflections from other facets than (110) were analyzed not to overlook the stepwise twisting. Azimuthal sector with 102 reflection or 200 reflection was cut out and azimuthally averaged. The peak was fitted with Gaussian, and we define the integrated intensity as the area of the Gaussian. The sample is PCL/PVB = 95/5, Tc = 45 ℃.

It is principally possible to determine the stepwiseness by analyzing 200 reflection. However, we could not detect apparent difference when the sample is rotated by 40 degree (Figure 8.25). The stepwise lamellar twisting of the same sample was confirmed by 110 reflection (Figure 8.23).

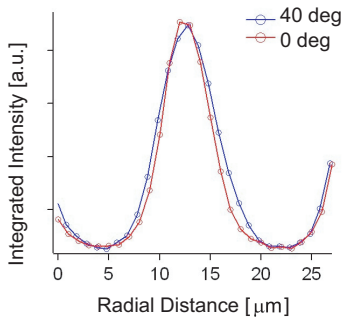

Figure 8.25: Integrated scattering intensity of 200 reflection with and without sample rotation around spherulite radii. PCL/PVB = 95/5, Tc = 45 ℃.

The reason why stepwise twisting cannot be observed with respect to 200 reflection is the same as described in Section 7.1.6. The deviation from uniform lamellar twisting when the reflection does not appear is undetectable. 200 reflection appears when lamellar are flat-on, whereas the deviation from uniform twisting is remarkable when lamellae are edge-on. Similar result can be obtained by simulation, where the asymmetric profile appears when the distribution of reciprocal spots broadens (Figure 8.26). If the angular spread of reciprocal spot is too wide, the difference between the maxima and the minima of the profile decreases.

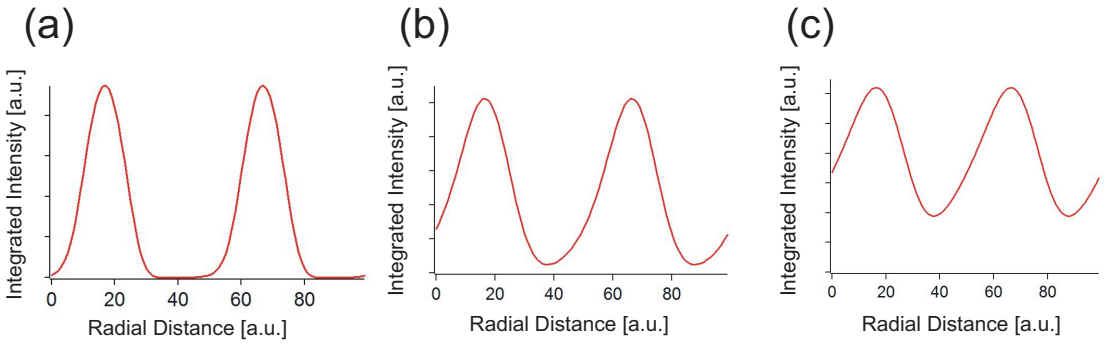

Figure 8.26: Calculated integrated intensity of 200 reflection. (a) $\Delta\omega$ = 20 deg, (b) $\Delta\omega$ = 40 deg, (c) $\Delta\omega$ = 60 deg. (Simulation II, stepparameter = 0.15, sample rotation angle = 40 deg). Radial distance of 50 corresponds to single banding.

The profile of integrated 102 reflection along radial direction was different as expected, when the sample was rotated as shown in Figure 8.27 (Refer Section 7.1.6). Similar result can be calculated assuming the stepwise lamellar twisting as shown in Figure 8.28.

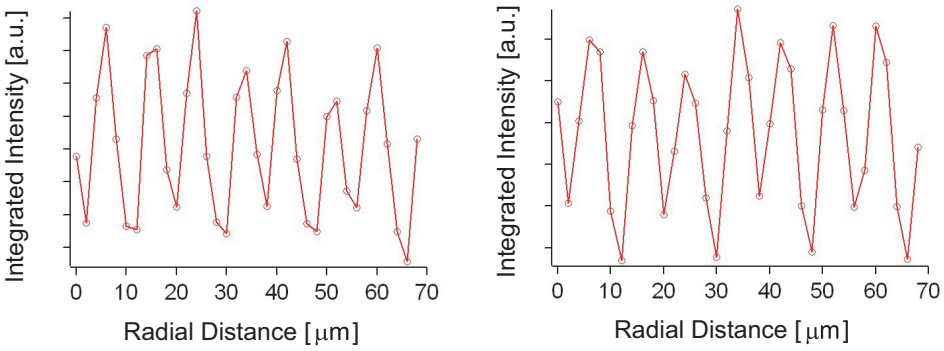

Figure 8.27: Integrated scattering intensity of 102 reflection with sample rotation around spherulite radii. Left: Sample rotation by 36 degree. Right: Sample rotation by -24 degree. PCL/PVB = 95/5, Tc = 45 ℃.

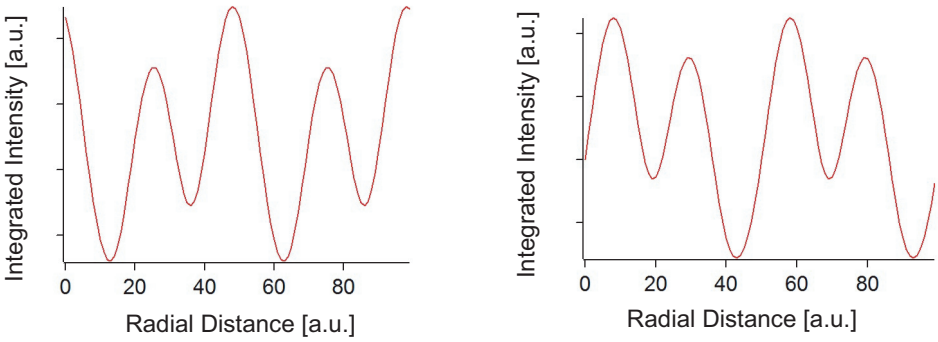

Figure 8.28: Simulated integrated intensity of 102 reflection along radial direction (Simulation II, $\Delta\omega$ = 20 deg, stepparater = 0.1). Rotation angle: 36 degree (Left) and -24 degree (Right).

8.3.3 Comparison of 2D spherulite and 3D spherulite

The image-plots of the azimuthal intensity distribution of 110 reflection with and without sample rotation are shown in Figure 8.29. Clear difference of the image-plot was not detectable in the case of the 3D spherulite when the sample was rotated. Slight difference was confirmed in the case of the 2D spherulite which was grown together with 3D spherulite, when the sample was rotated (Figure 8.30). This indicates that non-uniformity of lamellar twisting is relatively pronounced in the case of 2D spherulite.

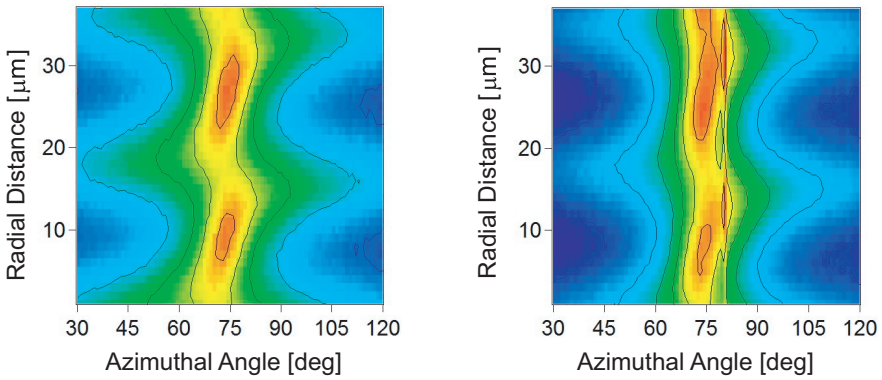

Figure 8.29: Image-plot of 110 reflection along the radial direction of 3D spherulite. Left: 0 degree, Right: 36 degree. PCL/PVB = 95/5, Tc = 48 ℃

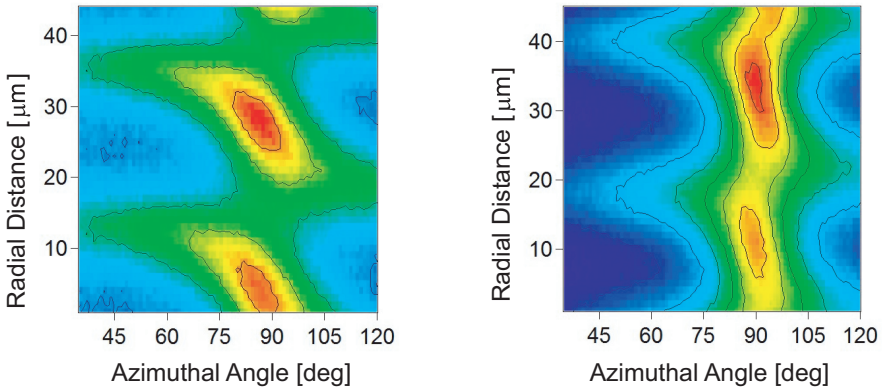

Figure 8.30: Image-plot of 110 reflection along the radial direction of 2D spherulite. Left: 0 degree, Right: 36 degree. PCL/PVB = 95/5, Tc = 48 ℃

It was possible to simulate the image-plot of 3D spherulite under the restriction of uniform rotation (Figure 8.31).

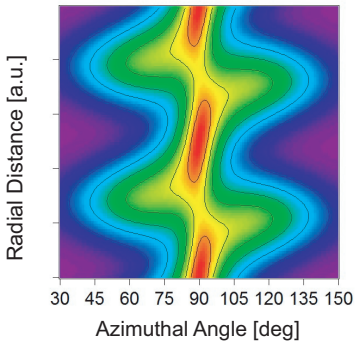

Figure 8.31: Calculated image-plot of 110 reflection. Simulation II, $\Delta\omega$ = 24 deg stepparameter = 0.0.

8.3.4 The ordering of chain packing

Ordering of chain packing was estimated from the FWHM of reflection in scattering angle direction. 200 reflection was unable to analyze because of the superimposing 201 and 104 reflections. Azimuthally averaged data was fitted with four Gaussians deriving from amorphous layer, 110 reflection, 111 reflection, and reflections around 200 (Figure 8.32). The FWHM of 110 reflection is plotted against the crystallization temperature with fixed PVB concentration (PCL/PVB = 95/5). It was confirmed that ordering of the chain packing is enhanced under high crystallization temperature (Figure 8.32). It is conceivable that the folded chain has more chances to fit in well ordered and thermodynamically stable state, under high crystallization temperature (Refer Section 2.2.2).

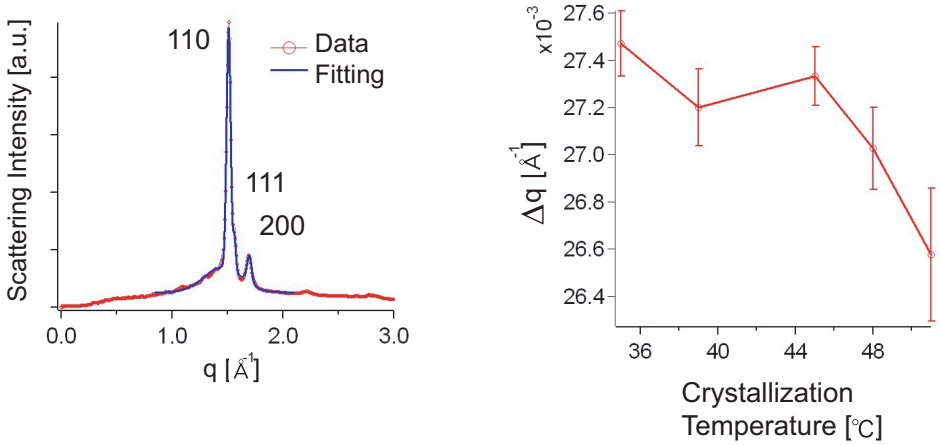

Figure 8.32: Left: WAXS intensity distribution along scattering angle direction was fitted with four Gaussians. Right: FWHM Δq was plotted against crystallization temperature. PCL/PVB = 95/5.

8.3.5 Azimuthal intensity distribution of hk0 reflection

It was found that the azimuthal intensity distribution of hk0 reflections changes depending on crystallization temperature and PVB concentration (Figure 8.33).

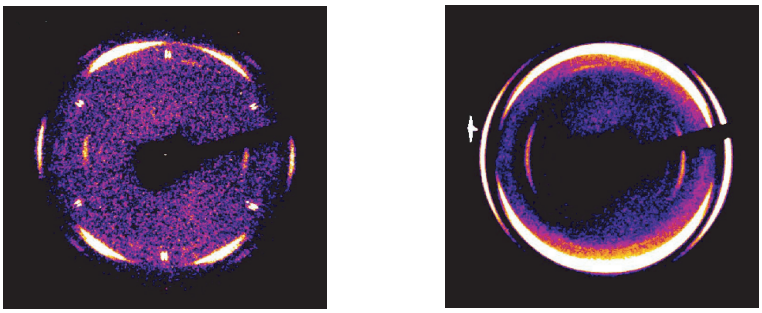

Figure 8.33: WAXS scattering pattern when folded chain is parallel with the incident x-ray. Left: PCL/PVB = 99.5/0.5, Tc = 45 ℃. Right: PCL/PVB = 95/5, Tc = 45 ℃.

The phenomenon where hk0 reflections broaden was quantitatively analyzed with 200 reflection. 110 reflection was unable to analyze partly because the neighboring two 110 reflections are connected together when the azimuthal intensity distribution broadens (Figure 8.33 Right).

Radial section of the 200 reflection was cut out and the azimuthal profile was fitted with Gaussian. If the Gaussian was not well fitted, the variance was evaluated with the Equation 8.2 by drawing a baseline (Figure 8.34 (b)). In this case, FWHM was defined as FWHM = $\sqrt{2}\sigma$, where σ is the variance defined as follows

$$\sigma^2 = \frac{\int (\theta - \bar{\theta})^2 f(\theta) d\theta}{\int f(\theta) d\theta} \tag{8.2}$$

where $\bar{\theta}$ is the mean value of θ and $f(\theta)$ is the observed azimuthal intensity distribution. The FWHM of 200 reflection under various conditions are plotted in Figure 8.34 (c).

It was found that azimuthal intensity distribution of hk0 reflection broadens under high crystallization temperature or high PVB concentration.

At this point, it has to be paid attention that the azimuthal intensity distribution is affected by the radial distance of the scanning point from spherulite center. We scanned the region apart from the center more than 150 μm. Therefore, the error deriving from the variance of the scanning position is within
(FWHM of beam)/(Radial distance) [rad] = $(5/150) \times (180/\pi)$ [deg] = 2 degree. The dependence of the FWHM on crystallization temperature and PVB concentration as stated above is beyond this value.

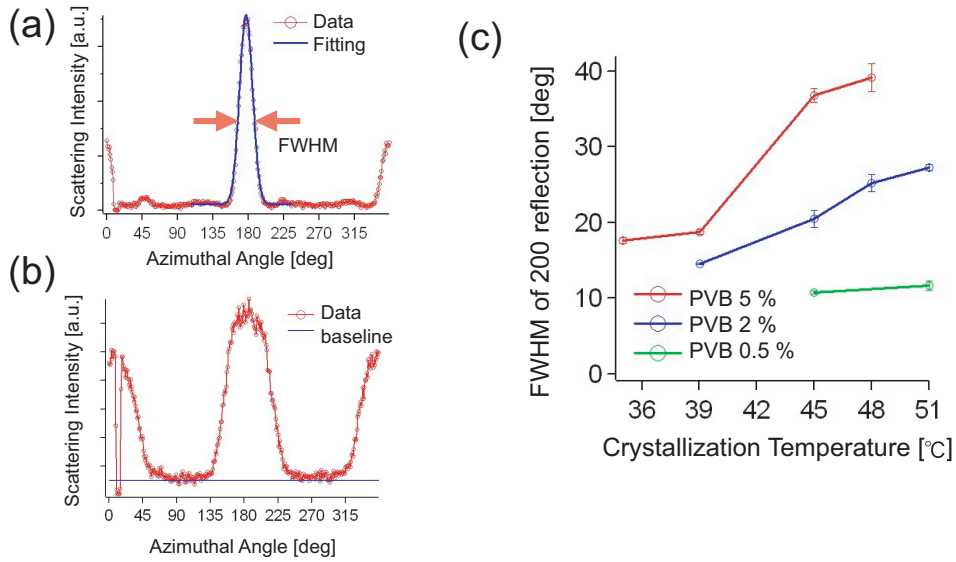

Figure 8.34: (a) FWHM of the azimuthal intensity distribution of 200 reflection was evaluated by Gaussian fitting. (b) If Gaussian did not fit well, the variance was calculated by drawing a baseline. (c) The FWHM of 200 reflection under various crystallization temperature and blend composition.

8.3.6 Evaluation of the angular spread of reciprocal spots around the three axes

It has been discussed in previous sections that the degree of freedom around three axes has to be evaluated. The rotational angle around b axis is referred to as ϕ. The rotational angle around c axis is referred to as θ. The rotational angle around a axis is defined as ψ (Figure 8.35).

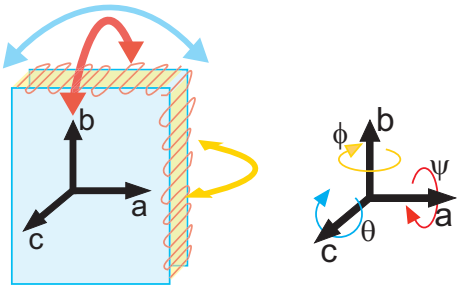

Figure 8.35: Definitions of angular parameters

Here, the three angular distribution are compared with respect to the PCL/PVB = 95/5, Tc = 45 ℃ sample. The angular distribution around *c* axis was estimated by 200 reflections, which satisfy Bragg condition when folded chains are parallel with the incident beam, as described in Section 8.3.5.

Next, we consider the distribution around *a* axis. When the angular spread of the reciprocal spot is broad, it seems possible to evaluate the distribution around *a* axis with azimuthal intensity distribution of 110 reflection when folded chains (*c* axis) are perpendicular to the x-ray. However, it is probably not practical. The reason is as follows. As discussed in Section 7.1.3, we have to take into account the correction factor $1/\sin\alpha$ considering that the lamellae rotate arond *b* axis. Moreover, the growth direction of lamellae flucuates as described in Section 8.4.4, which means that simply multiplying $1/\sin\alpha$ cannot be the correction. Therefore, we have to choose the reflections which are the most remote from *b* axis and meet Bragg condition when folded chains are perpendicular to the x-ray, such as 00ℓ. In general, 00ℓ reflections of polymer crystal are weak, because the stack number along *c* axis is small compared with those of other axes. Therefore, long exposure time was necessary. It was found that the FWHM of the azimuthal intensity distribution is about 6 degree. (Figure 8.36)

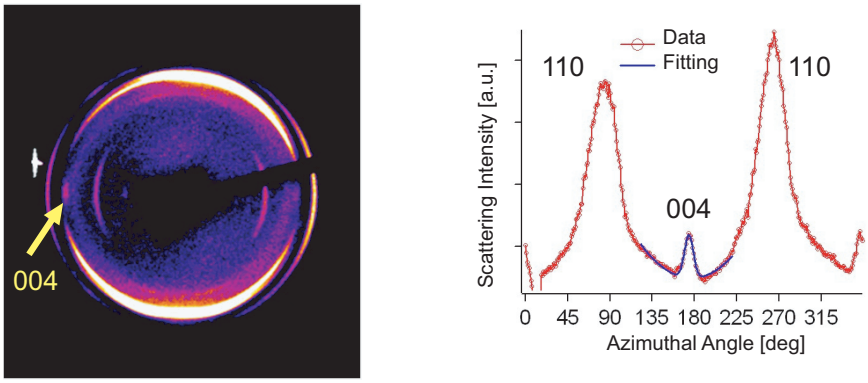

Figure 8.36: Left: 004 reflection appears when folded chains are perpendicular to the x-ray. Right: The azimuthal intensity distribution of 004 reflection was fitted with Gaussian.

The distribution around *b* axis, which is the lamellar growth direction, cannot be estimated directly from the single scattering pattern, because *b* axis was always

perpendicular to the incident beam. It was estimated by the radial integrated intensity profile of 200 reflection as shown in Figure 8.37. The integrated intensity of 200 reflection includes the information of the angular variance around *b* axis. If (beamsize)/(bandwidth) is larger, the convolution effect of the incident beam is pronounced, and thus the peak broadens. It is possible to eliminate the convolution effect by the equation

$$\sigma_{obs}^2 = \sigma_{real}^2 + \sigma_{conv}^2 \tag{8.3}$$

where σ_{obs} is the observed FWHM, σ_{real} is the true value of the variance. σ_{conv} is the convolution effect defined by $\sigma_{conv} = \sigma_{beamsize}/(\text{bandspacing}) \times 180$ [deg], using FWHM of the Gaussian beam $\sigma_{beamsize}$. It was found that the variance around *b* axis was about 14 degree.

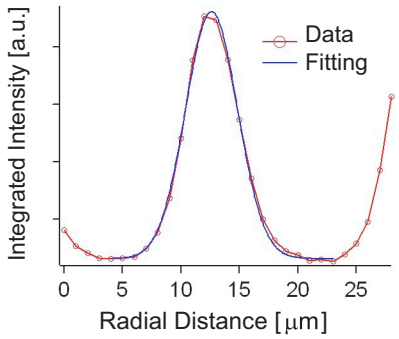

Figure 8.37: Integrated intensity of 200 reflection along radial direction was fitted with Gaussian.

Summarizing above, the magnitude relationship about the degree of rotational freedom around the three axes was concluded about the sample PCL/PVB = 95/5, Tc = 45 ℃.

$$\sigma_{c\ axis} > \sigma_{b\ axis} > \sigma_{a\ axis} \tag{8.4}$$

The relationship 8.4 is reflected in the simulation method as discussed in Section 7.1.4.

8.3.7 Lamellar orientation in unbanded area

Banding structure was not observed occasionally (Figure 8.38 (a)(b)). It may be partly because of the effect of space confinement. We cannot completely exclude the possibility that PVB is diluted at the area. However, it is probably not the case because the crystal nucleation frequency would increase drastically and 110 reflection would not be observed because of the narrow angular spread of reciprocal spot, if PVB is diluted in the area. When the microbeam was scanned along radial direction, 110 reflection was continuouly observed in radial direction. In addition, 200 reflection was not observed. This indicates that the lamellae in the area are fixed to edge-on orientation.

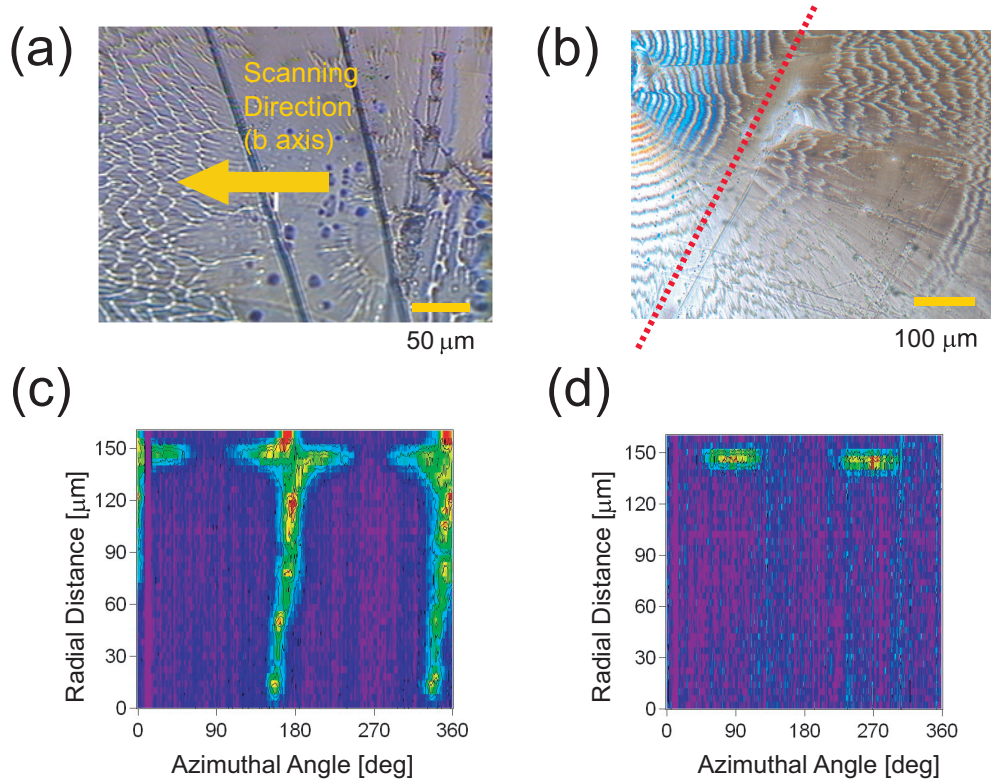

Figure 8.38: (a) Unbanded area of the spherulite (PCL / PVB = 98 / 2, Tc = 48 ℃). (b) Unbanded area of the spherulite (PCL / PVB = 95 / 5, Tc = 48 ℃). This sample was prepared to confirm the effect of space confinement. Left half over the red line is about 20 - 30 μm thick, and right half is less than 10 μm thick. The difference of the thickness is apparent from the birefringence. (c) Imageplot of 110 reflection in the area. (d) Imageplot of 200 reflection in the area. The region around 150 μm corresponds to the banding of POM image in (a).

Similar results have been reported in previous works [83][84], where all lamellae are edge-on in thin film. The polymer-substrate interaction may change depending on crystallization temperature [84].

8.3.8 Specific structure around spherulite center

When spherulites were grown in two-dimensional space under high crystallization temperature, specific structure as shown in Figure 8.39 (a) was observed. When the microbeam was scanned along the radial direction, 200 reflection was continuously observed in radial direction. Therefore, the radial direction of the area coincides with *a* axis. Moreover, the azimuthal intensity distribution of hk0 reflections is considerably narrow compared with the normal sperulite. It can be speculated that the wing-shaped region consists of the structure akin to single crystal. It is also conceivable that lamellar branching, which leads to broadening of the azimuthal intensity distribution, is less frequent.

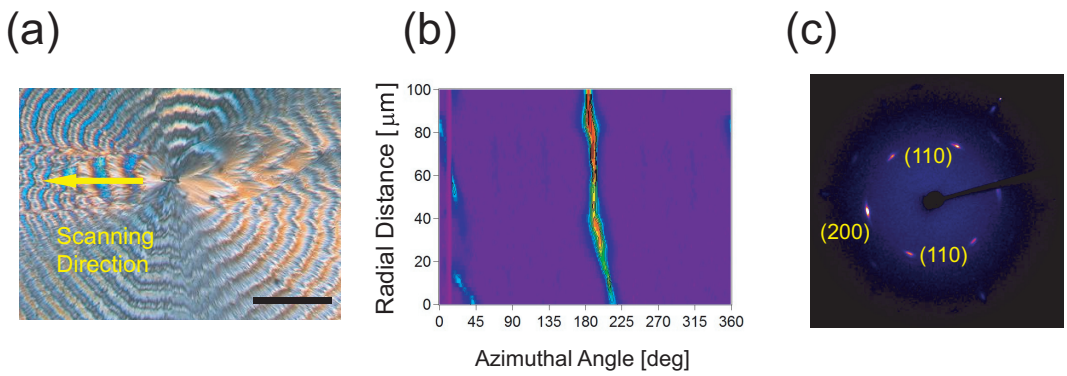

Figure 8.39: (a) Specific structure near the spherulite center (PCL/PVB = 95/5, Tc= 48 ℃). (b) The image-plot of 200 reflection along the scanning direction. (c) WAXS pattern at the area. Note that the scanning direction is horizontal. Scale bar: 100 μm.

Similar result has been reported in previous research as shown in Figure 8.40, where the wing-shaped structure derives from the difference of the growth speed between *a* axis and *b* axis [83][89]. This specific morphology has been reported to appear under high crystalizaion temperature. The formation of the structure may derive from the low branching frequency under high crystallization temperature as described in Section 2.2.4.

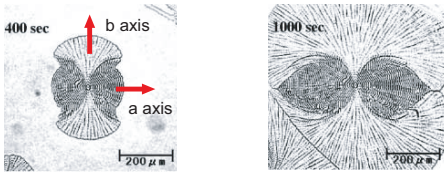

Figure 8.40: Wing-shaped structure reported in thin film ($\sim\mu$m) of Poly-(ethylenesuccinate) [83].

8.4 Discussion

8.4.1 Determination of the existence of stepwise lamellar twisting

Here we summarize the method how to determine whether or not stepwise lamellar twisting exists.

It was concluded from POM analysis that the degree of non-uniformity of twisting is enhanced under high crystallization temperature, which is consistent with the results of microbeam x-ray scattering (Refer Section 8.1.2). Moreover, POM analysis has the advantage that the signal is continuously observed, regardless of the angular spread of crystal facet. The disadvantage of POM is that it is sensitive to

the irregularity of sample thickness. As discussed in Section 8.4.3, the surface of spherulite grown in two dimensional space frequently ripples.

In contrast, microbeam x-ray scattering does not matter such variance of sample thickness. The disadvantage of x-ray scattering is that it may overlook the non-uniformity in the case where angular spread of reciprocal spot is narrow, and the sample rotation angle is limited. Large angle of rotation may be experimentally difficult, as discussed in Section 7.1.6. We may be able to overcome the issue by focusing on the reflections which satisfy the Bragg condition during relatively longer period, such as 102 reflection (Refer Section 8.3.2). However, observation of reflections other than hk0 reflections necessitates long exposure time. Hence, the radiation damage of the sample has to be carefully estimated in advance.

8.4.2 Rhythmic growth

Specific phenomena, which seem unlikely in the three-dimensional growth, are sometimes observed when spherulite grows in restricted space, such as thin film. In general, spherulite grows at constant rate as explained in Section 2.2.2 unless it entails phase separation or thermal perturbation. However, rhythmic growth has been reported where the radial growth speed fluctuates periodically [19]. There is another kind of rhythmic growth, where the sample thickness periodically changes [16]. These phenomenon sometimes occur simultaneously.

The fluctuation of radial growth rate is explained by Landau phenomenological theory [19], or the different growth speeds of edge-on lamellae and flat-on lamellae [82]. Here, previous reports on PCL/SAN blend system is introduced [15][14], which is quite similar to PCL/PVB blend in this work. Radial growth rate fluctuates, and slow growth rate is observed when lamellae take edge-on orientation (Figure 8.41 (Left)). SEM micrograph of the PCL/SAN blend is shown in Figure 8.41 (Right), where edge-on lamellae are seemingly fixed for a distance.

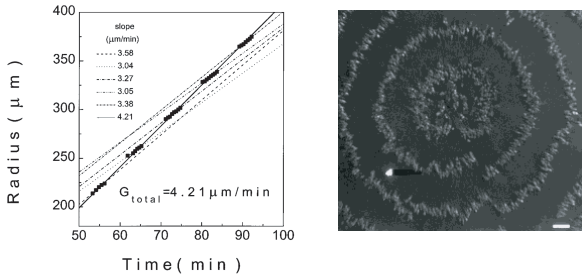

Figure 8.41: Left: Rhythmic growth rate of spherulite in PCL/SAN blend [14]. Right: SEM image of PCL/SAN spherulite surface. Scale bar: 10μm. [15]

The periodic change of the thickness is observed in both solution crystallization and melt crystallization [16][17][18]. The mechanism is explained as the balance between polymer depletion by the adsorption of molecules onto the crystal surface and the polymer supply by diffusion [16]. This phenomenon is also observed in pure PCL solution under two dimensional circumstance with sub-micron thickness.

The nonbirefringent spherulite of Figure 8.42 mainly consists of flat-on lamellae near the substrate. The lamellae near the top surface turned out to be edge-on by TEM.

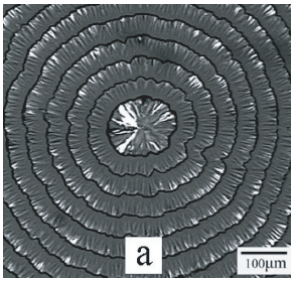

Figure 8.42: POM image of nonbirefringent banded spherulite of PCL grown under solution. The banding structure derives from the periodic fluctuation of sample thickness [16].

As described above, the polymer-substrate interaction and restricted thickness may well give rise to the spherulitic morphology or crystallization process which seems to be different from the three dimensional crystallization.

It is deduced that the rhythmic growth of PCL/SAN blend previously reported, where the edge-on lamellae grow slower than flat-on lamellae, can be explained by the same mechanism with the PCL/PVB, for they are common in that edge-on lamellae grows slowly than flat-on lamellae. Previous works on the theoretical assessment of rhythmic growth by Kyu [19] cite PCL/SAN blend as the supporting data. However, the theory may not be applied to the specific rhythmic growth which involves slower growth of edge-on lamellae, because the theory does not take into account the space confinement. It is noteworthy that edge-on lamellae of PCL/SAN blend is fixed, which is similar to the result in this work. The stepwise lamellar twisting may exist in the case of PCL/SAN blend. Considering above, space confinement or polymer-substrate interaction contribute to the rhythmic radial growth of PCL/PVB spherulite.

Combining with the results of microbeam x-ray scattering in previous works and growth rate analysis, we can qualitatively estimate the relative angular speed of lamellar twisting ω with the equation

$$\frac{d\theta}{dr} = \frac{d\theta/dt}{dr/dt} = \frac{\omega}{V} \tag{8.5}$$

where r is the radial distance from spherulite center, V is the spherulite growth rate, and θ is the lamellar twist phase. Microbeam x-ray scattering measurement gives the information of $d\theta/dr$, and V can be analyzed by POM. Both $d\theta/dr$ and V is smaller when lamellae are edge-on. Therefore, the angular speed reaches minima at edge-on orientation. The fluctuating value of ω indicates that the driving force of lamellar twist may be affected by the lamellae-substrate interaction.

8.4.3 The origin of stepwise lamellar twisting

Considering the origin of the stepwise lamellar twisting, we start from the results of the previous section.

- Rhythmic growth along the radial direction was observed by POM image analysis. Edge-on lamellae grow slowly than flat on lamellae (Section 8.1.1).
- All lamellae in unbanded region were observed to be fixed to edge-on orientation by microbeam WAXS measurement (Section 8.3.7).
- It was suggested by microbeam SAXS measurement and microbeam WAXS measurement that the nonuniformity of lamellar twisting is relatively enhanced in two dimensional spherulite compared with three dimensional spherulite (Section 8.2.1, Section 8.3.3).
- It was confirmed by microbeam WAXS involving sample rotation that stepwise twisting, where twist phase proceeds slowly when lamellae are edge-on, appears at high crystallization temperature, or high PVB concentration (Section 8.3.1).

It can be deduced from above four results that the growth in confined space which involves intimate contact with substrate contributes to the nonuniformity of lamellar twisting. It is likely that the space confinement has an effect to fix the lamellar orientation to edge-on. Supposing that these proposals are true, the remaining question is why the stepwise twisting occurs under high crystallization temperature. If the stepwise twisting derives from the space confinement, it is natural that the balance between the driving force of lamellar twisting and the effect of space confinement is the critical factor for the stepwise twisting. As explained in Section 2.3.2, the degree of structural asymmetry, which is the driving force of lamellar twisting, decreases under high crystallization temperature. The stepwise twisting might occur under high crystallization temperature, where the two conflicting factors are comparable.

Moreover, it is conceivable that the increase of the fluctuation of lamellar growth direction under high crystallization temperature or high PVB concentration leads to the protruding lamellae from the sample surface (Refer Section 8.4.4). Previous reports about the AFM observation of spherulite surface of Poly-(methylene terephthalate) indicate that the edge-on lamellae region is thicker than flat-on lamellae [82]. SEM observation of elevated edge-on lamellae in PCL/SAN blend [15] may well fall in line (Figure 8.41 Right).

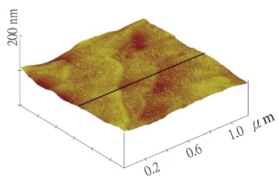

Figure 8.43: AFM image of the surface of Poly-(methylene terephthalate) [82].

The twist phase of the protruding lamellae may be fixed because of the lack of free space for further growth as schematically illustrated in Figure 8.44. The speculation may correlate with the fixed edge-on lamellae of PCL/SAN as shown in Figure 8.41 Right. It is noteworthy that the previous reports about PCL/SAN correlate the fixed orientation of edge-on lamellae with the discontinuous twisting model of Bassett as summarized in Section 2.3.2. It may be unreasonable deduction because twist phase proceeds slowly specifically when lamellae are edge-on, providing that stepwise twisting exist in PCL/SAN blend as discussed in Section 8.4.2.

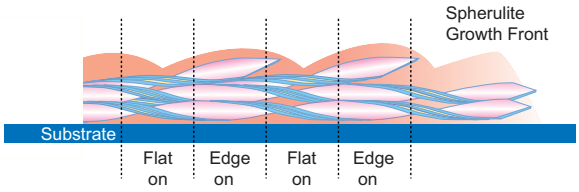

Figure 8.44: Protruding edge-on lamellae from spherulite surface.

8.4.4 The influence of PVB on PCL lamellar structure

When we consider the influence of PVB on PCL lamellar structure, we start from the results of the previous section.

- Ordering of chain packing is enhanced under high crystallization temperature (Refer Section 8.3.4).
- Azimuthal intensity distribution of hk0 reflection broadens under high crystallization temperature or high PVB concentration (Refer Section 8.3.5).
- Azimuthal intensity distribution of lamellar reflection is around 7-9 degree and slightly decreases under high crystallization temperature, about PCL/PVB = 95/5 sample (Refer Section 8.2.2).

There are two possible origins of the broadening of hk0 reflection. The disorder of chain packing or the fluctuation of lamellar growth direction. It is deduced that the former is not the case because the ordering of the chain packing enhances whereas the azimuthal distribution broadens at high crystallization temperature. Therefore, the distribution of hk0 reflection is attributable to the fluctuation of the lamellar growth direction.

As a consequence, it is conceivable that the growth direction of lamellae fluctuates under high crystallization temperature, or under high PVB concentration. This proposal is in accord with the coarse banding structure under high PVB concentration (Figure 8.45).

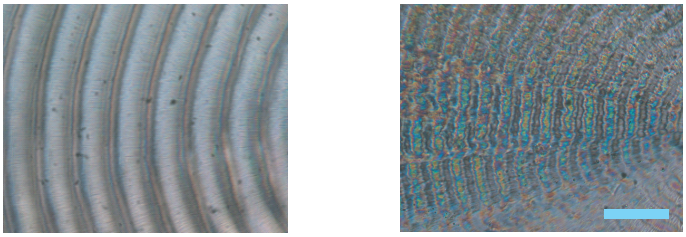

Figure 8.45: The banding structure of PCL/PVB. Left: PCL/PVB = 99.5, Tc = 45 ℃. Right: PCL/PVB = 90/10, Tc = 45 ℃. Scale bar: 50 μm.

Next, we compare the angular distribution of hk0 reflection with that of lamellar reflection. The former derives from the distribution around *c* axis, and the latter derives from the distribution around *a* axis. We can conclude from the experimental results that the variance of the growth direction has selectivity that variance around *c* axis is bigger than that of *a* axis, particularly under high crystallization temperature as illustrated in Figure 8.46 (Left).

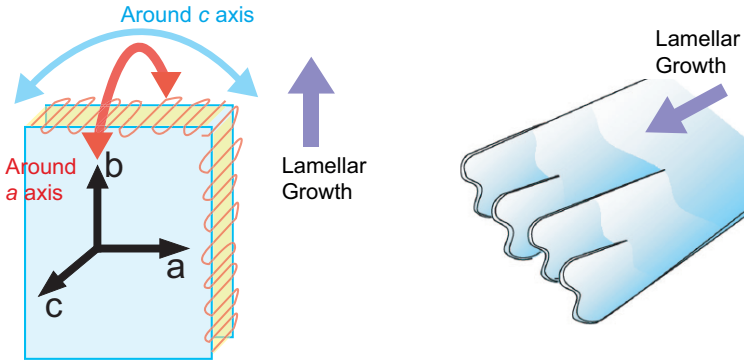

Figure 8.46: Left: The selectivity of the variance of lamellar growth direction. Right: The overlap of lamellae associated with lamellar branching [12].

Then, what is the cause of the fluctuation of the lamellar growth direction? In Section 2.2.4, it has been introduced that the frequency of lamellar branching reduces with higher concentration of uncrystallizable material, or high crystallization temperature. According to the theory [10], less frequency of lamellar branching leads to more free space among the lamellae, which allows more fluctuation of lamellar growth direction.

The increase of the azimuthal intensity distribution of 200 reflection under high crystallization temperature can be explained with the lamellar branching. The specific morphology which appeared under high crystallization temperature (Refer Section 8.3.8) may support the speculation. Moreover, lamellar branching entails the overlap of lamellae, which leads to the variance of lamellar growth direction around *a* axis (Figure 8.46 (Right)). If the frequency of lamellar branching reduces under high crystallization temperature, the result in Figure 8.9 falls in line, which indicates the low angular variance around *a* axis under high cyrstallization temperature. The selectivity of the growth direction may derive from the anisotropy of

space confinement around lamellae.

On the other hand, the dependence of the fluctuation on PVB concentration cannot be explained simply by the branching, because it is unthinkable that a few percent of PVB cause the drastic change of the amorphous phase. It has been reported that the degree of crystallinity is almost constant regardless of the PVB concentration within 5 percent by DSC analysis [80]. However, PVB molecules may contribute to the stabilization of planer growth front, which inhibits lamellar branching by the hydrogen bonding [12][49].

Summarizing above, it was suggested that the frequency of lamellar branching decreases under high crystallization temperature, or high PVB concentration, assuming that the widening of the azimuthal intensity distribution of 200 reflections means the low frequency of lamellar branching. This assumption has to be examined by real space observations.

8.4.5 Driving force of lamellar twist in PCL/PVB spherulite

In our research, the chain tilt with respect to lamellar normal was not detected in PCL/PVB with the accuracy of 3-4 degree. The sample was crystallized at 53 ℃, which is nearly the highest degree within the practicability. It is well known that the tilting angle of folded chain to lamellar normal increase at high crystallization temperature. The tilting angle in the case of other achiral polymers, such as PE and PVDF, are reported to be more than 15 degree. Therefore, it is deduced that chain tilt does not contribute to the torque of lamellar twist in pure PCL/PVB spherulite.

If folded chain does not tilt with respect to lamellar normal in PCL/PVB spherulite, what is the driving force of lamellar twisting? Two possibilities are considered in the following.

Uneven distribution of PVB on the lamellar surface has been suggested in previous works. The existence of two kinds of lamellar structure supports the hypothesis. However, it cannot be applied to the spherulite grown under low crystallization temperature which has single lamellar structure and narrow banding structure. Provided that the uneven distribution of PVB molecules exists, why does it happen without chain tilt? The asymmetric structure without chain tilt as discussed in Section 8.4.6 may be the reason.

There is a possibility that the PVB molecules increase the frequency of lamellar branching, which accompanies the quantum increment of lamellar twist phase as introduced in Section 2.3.2. This explanation with screw dislocation model gives clear solution to the drastic reduction of bandwidth under high PVB concentration. However, as discussed in Section 8.4.4, there is a possibility that the widening of the azimuthal intensity distribution of 200 reflection may indicate the low frequency of lamellar branching. If it is the case, the screw dislocation model is incorrect. It has to be examined by real space observation techniques, how PVB molecules affects the frequency of the branching.

8.4.6 Chiral factor in pure PCL spherulite

The chain tilt was not observed in PCL/PVB spherulite including 0.5 percent PVB. The chain tilt was not detectable when 5 percent PVB was added. Therefore, it is deduced that PVB does not have an influence on the chain tilt, and that chain does not tilt in pure PCL spherulite [88].

In contrast, there are several reports which indicates the asymmetry of lamellar structure in pure PCL. The coarse banding structure at higher crystallization temperature has been reported [49][52][53]. Even if the coarse banding structure does not necessarily mean lamellar twist (Refer Section 8.4.2), the unbalanced surface stress may exist in the nonbanded spherulite [21]. It is commented by B.Lotz that the absent of the banding is not necessarily the criteria to rule out the asymmetric structure. As shown in Figure 8.47, PCL shows torsional stress even though it does not exhibit clear banding structure.

Figure 8.47: Split bent crystal of PCL in thin film [21].

These facts are incompatible if the commonly accepted theory by Keith holds true, where the surface stress cannot exist without the chain tilt in the case of achiral and nonhelical polymers.

Keith and Padden cite the other chiral factor than the chain tilt which causes the unbalanced surface stress [30] in helical polymer crystal. As briefly referred in Section 2.1.1, the crystal structure of achiral polymers can be classified into helical and non-helical. In the case of helical polymer, helical structure of right and left handedness compensate each other and usually forms non-band spherulite [30]. However, there exist some exceptions such as isotactic poly (1-butene) and isotactic polypropylene. These polymers show banding structure under specific conditions. As the chain tilt is not observed in the single crystal of these polymers, incomplete compensation of both hands of helix may exist in these polymers [30].

Lotz explains the chiral factor in isotactic poly(1-butene) [20] as follows. Banded spherulite formIII crystallize among non-banded formII spherulite. The crystal structure of form3 Poly(1-butene) is 4_1 helix orthorhombic structure. The c-axis projection of (110) is illustrated in Figure 8.48. As the Figure indicates, loops of the top side draw an arc leaving from lamella, whereas loops of the bottom side move into the lamella. This asymmetric structure results in surface stress. The asymmetric structure can exist even without chain tilt in achiral and helical polymer crystal.

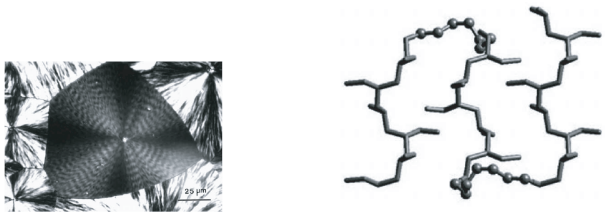

Figure 8.48: Left: The POM image of poly(1-butene) FormIII spherulite. Banded spherulite forms among non-banded spherulite. Right: Simulated conformation of (110) plane, where upside and downside of lamellae are not symmetrical [20].

In this context, one possibility resolving the discrepancy regarding the chain tilt in pure PCL spherulite as mentioned earlier is that the crystal structure of PCL is quasi-helical and the asymmetric structure may exist without chain tilt. It has been reported that the carbonyl group of PCL deviate from zig-zag plane of PCL chain [51]. This deduction falls in line with the fact that the banding structure of pure PCL spherulite is coarse and broad like achiral and helical polymer [49], such as β-polypropylene [81] (Figure 8.49).

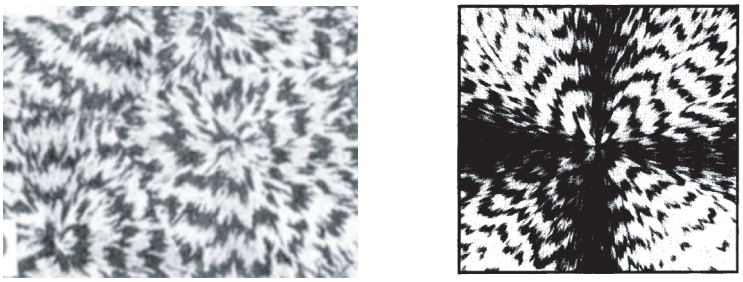

Figure 8.49: Left: Banded spherulite of pure PCL [49], Right: Banded spherulite of β-polypropylene [81]

Chapter 9

Conclusions and Future works

9.1 Conclusions

In this work, we analyzed the lamellar twisting of polymer spherulites in PCL/PVB and PVDF/PEA with the goal to figure out the mechanism of lamellar twisting and its non-uniformity. The summary of the conclusions are as follows;

- Non-uniformity of lamellar twisting could be estimated by POM and microbeam SAXS and microbeam WAXS.
- Chain tilt with respect to lamellar normal in intact spherulite of PCL/PVB and PVDF/PEA could be estimated by microbeam SAXS-WAXS simultaneous measurement.
- It was suggested that the origin of the stepwise lamellar twisting resides in the growth in two dimensionally confined space.
- PCL lamellar growth direction varies under high crystallization temperature, or high PVB concentration. This variance may correlate with the frequency of lamellar branching.
- The variance has selectivity that the variance around *c* axis of the unit cell is wider than *a* axis. This tendency is conspicuous under high crystallization temperature.
- It was suggested that the driving force of lamellar twisting in PCL/PVB is not the chain tilt. This may hold true for the coarse banding structure of pure PCL spherulite under high crystallization temperature.

9.2 Future works

Here, unresolved problems in this work, what we conceive about the lamellar twist, and the perspective for the future works are briefly mentioned. We expect that future works will achieve further elucidation of lamellar twisting mechanism.

- Simulation

It is assumed in the present simulation that the lamellar growth direction is uniform, which was not found to be the case. The second point is that the degrees of freedom around three axes have to be considered. These points have to be taken into account in future works.

- Non-banded spherulite of pure PCL

Lamellar twisting may well exist in the unbanded spherulite, where the cooperativity is lost. In our research, we observed the unbanded spherulite of pure PCL, however the twisting structure was unable to analyze. It may be because of the lost of cooperative twisting of lamellae. Even if the distinct cooperativity is lost, we may be able to analyze the periodic change of lamellar twist by Fourier analysis of the imageplot.

In the context of the discussion in Section 8.4.6, the asymmetrical structure without the chain tilt may exist in the crystal structure of PCL. The detailed analysis of the crystal structure of PCL is expected.

- POM analysis

In the present study the sample thickness was restricted in POM analysis. This problem may be resolved by the compensator, which adjusts the retardation.

- Localization of PVB molecule

In section 8.4.5, it was discussed that uneven distribution of PVB on PCL lamellar surface may give rise to lamellar twisting. In order to examine such possibility, observation of the localization of PVB molecule is important. Previous works indicates that one of the two kinds of lamellar structure in PCL/PVB is akin to pure PCL lamellar structure and that PVB localize in one of the two kinds of lamellae, based on the observation results as follows;

1. Lamellar period of pure PCL is approximately equal to one of the lamellar period of the blend.

2. The transition of SAXS pattern during melting procedure can be construed as the superposition of pure PCL and the another lamellar structure

The localization of PVB molecules can be analyzed more apparently by neutron scattering. It is expected that the reflection from one lamellar structure will change depending on the degree of deuteration of PVB molecule, if PVB molecule localize in one of the lamellar structure. Without neutron scattering, we may be overcome this issue by x-ray scattering, if the PVB molecule can be chemically modified with heavy atoms.

- The influence of PVB on lamellar branching

In Section 8.4.5 and Section 8.4.4, we discussed the possibility that PVB may increase or decrease the frequency of lamellar branching. We have to examine these possibilities by real space observations, such as AFM. We speculate the assumption that PVB decrease the frequency is more reasonable, because it was deduced in Section 8.4.4 that the widening of the azimuthal distribution of 200 reflection means the low frequency of lamellar branching. As discussed in Section 8.4.5, even if the quasi-discontinuous model based on the assumption that PVB increases the frequency of branching is rejected, the uniform rotation model with the asymmetrical structure still remains as a reasonable mechanism of lamellar twisting.

- Causal linkage between the regime transition and two kinds of lamellae

It has been reported that PCL turns non-banded spherulite into banded spherulite depending on the crystallization temperature [52]. The discontinuous change of growth speed derives from the crystallization mode at the growth front. Although regime transition was not confirmed in PCL/PVB in this work because of the inadequacy of the number of data points, the regime transition may well exist in PCL/PVB blend. We speculate that this may correlate with the two kinds of lamellar structure.

- Application to other banded spherulite

Investigation of the chain tilt in Poly-(ℓ lactic acid), which has similar molecular structure to PCL, may be interesting. Transition from no-banded spherulite to banded spherulite has been reported in PLLA [85], which is also reported in PCL. Moreover, clear banding appears when PLLA is blended with PHB [86] or PEG [87]. It is speculated that the chain tilt may not exist in the banded spherulite of PLLA and PLLA blends, because the chain tilt was not detected in banded spherulite of PCL/PVB in this work.

In this work, PCL/SAN blend frequently appears as an comparative sample. Both rhythmic growth and fixed edge-on lamellae has been confirmed in PCL/SAN spherulite. We speculate that the stepwise lamellar twisting exist in PCL/SAN blend. The observation by microbeam x-ray scattering and POM is expected to examine the existence of stepwise lamellar twisting.

Bibliography

[1] Tatsuya Kikuzuki, Bachelor thesis, (2008).

[2] G.R.Strobl,"高分子の物理" Springer (1997).

[3] L.H.Sperling, Introduction to Polymer Physics, (1985), Wiely-Interscience.

[4] D.I.Bower, An Introduction to Polymer Physics, (2002), Cambridge University Press.

[5] Y.Nozue, Y.Shinohara, Y.Amemiya, Polymer Jounal, (2007), 39, 1221.

[6] A.Keller, Journal of Polymer Science, 1955, 17, 291.

[7] J.D.Hoffmann, R.L.Miller, Polymer, (1997), 38, 3151.

[8] A.Toda, Colloid and Polymer Science, (1992), 270, 667.

[9] A.Toda, A.Keller, Colloid and Polymer Science, (1993), 271, 328.

[10] H.D.Keith, F.J.Padden, Journal of Applied Physics, (1963), 34, 2409.

[11] H.D.Keith, F.J.Padden, Journal of Polymer science, (1964), 35, 1270.

[12] A.Toda, M.Okamura, K.Taguchi, M.Hikosaka, H.Kajioka, Macromolecules, (2008), 41, 2484.

[13] A.Toda, K.Taguchi, H.Kajioka, Macromolecules, (2008), 41, 7505.

[14] Z.Wang, L.An, B.Jiang, X.Wangh, Macromolecules Rapid Communication, (1998), 19, 131.

[15] Z.Wang, L.An, W.Jiang, B.Jiang, X.Wang, Journal of Polymer Science: Part B: Polymer Physics, (1999), 37, 2682.

[16] Z.Wang et al, Macromolecules, in press.

[17] Y.Duan, Y.Jiang, S.Jiang, L.Li, S.Yan, J.M.Schultz, Macromolecules, (2004), 37, 9283.

[18] Y.Wang, C.Chan, L.Li, K.M.Ng, Langmuir, (2006), 22, 7384.

[19] T.Kyu, H.W.Chiu, A.J.Guenthner, Y.Okabe, H.Saito, T.Inoue, Physical Review Letters, (1999), 83, 2749.

[20] B.Lotz, S.Z.D.Cheng, Polymer, (2005), 46, 577.

[21] B.Lotz, S.Z.D.Cheng, Polymer, (2006), 47, 3247.

[22] A.Toda, T.Arita, M.Hikosaka, Polymer, (2001), 42, 2223.

[23] Y.Nozue, S.Hirano, R.Kurita, N.Kawasaki, S.Ueno, A.Iida, T.Nishi, Y.Amemiya, Polymer, (2004), 45, 8299.

[24] Y.Fujiwara, Journal of Applied Polymer Science, (1960), 4, 10.

[25] I. Saracovan, H. D. Keith, R. St. J. Manley, G. R. Brown, Macromolecules, (1999), 32, 8918.

[26] H.D.Keith, F.J.Padden Jr, Polymer, (1984), 25, 28.

[27] H.D.Keith, Polymer, (2001), 42, 9987.

[28] H.D.Keith, F.J.Padden Jr, B.Lotz, J.C.Wittmann, Macromolecules, (1989), 22, 2230.

[29] J.Xu, B-H.Guo, Z-M.Zhang, J-J.Zhou, Y.Jiang, S.Yan, L.Li, Q.Wu, G-Q.Chen, J.M.Schultz, Macromolecules, (2004), 37, 4118.

[30] H.D.Keith, F.J.Padden Jr, Macromolecules, (1996), 29, 7776.

[31] J.M.Schultz, Polymer, (2003), 44, 433.

[32] K.L.Singfield, J.K.Hobbs, A.Keller, Journal of Crystal Growth, (1998), 183, 683.

[33] A.Toda, M.Okamura, M.Hikosaka, Y.Nakagawa, Polymer, (2003), 44, 6135.

[34] A.Toda, T.Arita, M.Hikosaka, J.K.Hobbs, M.J.Miles, Journal of Macromolecular Science, (2003), B42, 753

[35] A.Toda, M.Okamura, M.Hikosaka, Y. Nakagawa, Polymer, (2005), 46, 8708.

[36] M.I.Abo el Maaty, D.C.Bassett, Polymer, (2001), 42, 4957.

[37] D.C.Bassett, Polymer, (2006), 47, 3263.

[38] D.Patel, D.C.Bassett, Polymer, (2002), 43, 3795.

[39] D.C.Bassett, Journal of Macromolecular Science, (2003), B42, 227.

[40] D.C.Bassett, A.M.Hodge, Proceeding of the Royal Society of London, (1981), A377, 61.

[41] D.C.Bassett, A.M.Hodge, Polymer, (1978), 19, 469.

[42] A.J.Lovinger, H.D.Keith, Macromolecules, (1996), 29, 8541.

[43] D.C.Bassett, A.M.Hodge, Proceeding of the Royal Society of London, (1981), A377, 25.

[44] M.Robert, F.Khoury, Polymer, (1987), 28, 38.

[45] A.J.Lovinger, Journal of Polymer Science: Polymer Physics Edition, (1980), 18, 793.

[46] R.Hasegawa, Y.Takahashi, Y.Chatani, H.Tadokoro, Polymer Journal, (1972), 3, 600.

[47] Y.Li, A.Kaito, S.Horiuchi, Macromolecules, (2004), 37, 2119.

[48] A.Kaito, M.Shimomura, M.Akaba, S.Nojima, Journal of Polymer Science, (2007), B45, 1959.

[49] H.D.Keith, H.J.Padden, T.P.Russell, Macromolecules, (1989), 22, 666.

[50] G.C.Eastmond, Advances in Polymer Science, (2000), 149, 59.

[51] Y.Chatani, Y.Okita, H.Tadokoro, Y.Yamashita, Polymer, (1970), 1, 555.

[52] Y.Fan, E.M.Woo, Colloid and Polymer Science, (2008), 286, 917.

[53] P.J.Phillips, G.J.Rensch, K.D.Taylor, Journal of Polymer Science, (1987), B25, 1725.

[54] Y.Takahashi, Y.Matsubara, H.Tadokoro, Macromolecules, (1982), 15, 334.

[55] J-C.Lee, K.Nakajima, T.Ikehara, T.Nishi, Journal of Applied Polymer Science, (1997), 64, 797.

[56] ファインマン物理学 II 巻

[57] 大津元一, 現代光科学, (1994), 朝倉書店.

[58] H.Kajioka, A.Hoshino, H.Miyaki, Y.Miyamoto, A.Toda, M.Hikosaka, Polymer, (2005), 46, 8717

[59] J.K.Hobbs, D.R.Binger, A.Keller, P.J.Barham, Journal of Polymer Science (2000), 38, 1575

[60] Y.Nozue, R.Kurita, S.Hirano, N.Kawasaki, S.Ueno, A.Iida, T.Nishi, Y.Amemiya, Polymer, (2003), 44, 6397.

[61] T.Ikehara, H.Jinnai, T.Kaneko, H.Nishioka, T.Nishi, Journal of Polymer Science, (2007), B45, 1122.

[62] O.Dupont, D.A.Ivanov, A. M. Jonas, R. Legras, Journal of Applied Crystallography, (1999), 32, 497.

[63] A.Guinier, X-ray diffraction in Crystals, Imperfect Crystals, and Amorphous Bodies, Dover, (1963).

[64] G.Glatter, O.Kratky, Small angle x-ray scattering, Academic Press, New York, (1982).

[65] L.A.Feigin, D.I.Svergun, Structure Analysis by Small Angle X-ray Scattering and Neutron Scattering, Plenum Press, New York, (1987).

[66] N.Stribeck, ”X-ray Scattering of Soft Matter”, (2007), Springer.

[67] D.I.Svergun, M.H.J.Koch, Reports on Progress in Physics, (2003), 66, 1735.

[68] L.V.Azaroff, ”エックス線結晶学の基礎”, 丸善, (1973).

[69] F.Cser, Journal of Applied Polymer Science (2001), 80, 2300.

[70] A.J.Ryan, W.Bras, G.R. Mant, G.E.Derbyshire, (1994), 35, 4537.

[71] 菊田惺志,「X線回折・散乱技術（上）」, 東京大学出版会, (1992).

[72] 雨宮慶幸, 伊藤和輝, 日本結晶学会誌, (2003), 45, 163.

[73] 後藤俊治, 石川哲也, 日本結晶学会誌, (2005), 47, 171.

[74] 猪子洋二, 日本結晶学会誌, (1999), 41, 227.

[75] S.M.Gruner, M.W.Tate, E.F.Eikenberry, Review of Scientific Instruments, (2002), 73, 2815.

[76] K.Ito, H.Kamikubo, N.Yagi, Y.Amemiya, Japanese Journal of Applied Physics, (2005), 44, 8684.

[77] 高野秀和、香村芳樹、放射光学会誌, (2006), 19, 314.

[78] A.Iida, T.Noma, Nuclear Instruments and Methods in Physics Research, (1993), B82, 129.

[79] 大柳宏之、「シンクロトロン放射光の基礎」, 丸善, (1996).

[80] J-C.Lee, K.Nakajima, T.Ikehara, T.Nishi, Journal of Applied Polymer Science, (1998), 69, 193.

[81] F.J.Padden, H.D.Keith, Journal of Applied Physics, (1959), 30, 1479.

[82] W-T.Chuang, P-D,Hong, H H.Chuah, Polymer (2004), 45, 2413.

[83] K.Kawashima, R.Kawano, T.Miyagi, S.Umemoto, N.Okui, Journal of Macromolecular Science, (2003), B42, 889.

[84] H.Wang, Z.Gan, J.M. Schultz, S.Yan, Polymer, (2008), 49, 2342.

[85] Y.Wang, J.F.Mano, Journal of Applied Polymer Science, (2007), 105, 3500.

[86] M.Gazzano, M.L.Focarete, C.Riekel, M.Scandola, Biomacromolecules, (2004), 5, 553.

[87] M.Sheth, R.A.Kumar, V.Dave, R.A.Gross, S.P.Mccarthy, Journal of Applied Polymer Science, (1997), 66, 1495.

[88] A.Toda, private communications (unpublished).

[89] H-M.Ye, J.Xu, G-H.Gui, T.Iwata, Macromolecules, (2009), 42, 694.